

Université de Strasbourg
École Doctorale 182 – Physique et
Chimie-Physique
Institut Pluridisciplinaire Hubert Curien



DOCTORAL THESIS IN PHYSICS

Precision measurements in the multi-strange baryon sector at the LHC with the ALICE experiment

October 2020 – September 2023

Candidate:
Romain Schotter

Thesis advisors:
Antonin Maire, Boris Hippolyte

January 2022

Résumé

Abstract

Acknowledgements

For Romain Schotter, this work of the Interdisciplinary Thematic Institute QMat, as part of the ITI 2021 2028 program of the University of Strasbourg, CNRS and Inserm, has been supported by IdEx Unistra (ANR 10 IDEX 0002), and by SFRI STRAT'US project (ANR 20 SFRI 0012) and EUR QMAT ANR-17-EURE-0024 under the framework of the French Investments for the Future Program.

Contents

1	Preface	11
2	Particle physics	15
I	The Standard Model of particle physics	16
I-A	Quantum field theories and fundamental symmetries	16
I-B	Particles and fundamental interactions	17
I-C	The strong force, a colourful interaction	23
I-C.i	Running of α_s , colour confinement and asymptotic freedom	28
I-C.ii	Chiral symmetry breaking	31
I-C.iii	The QCD-phase diagram	33
II	The Quark-Gluon Plasma	35
II-A	The time evolution of a heavy-ion collision	36
II-B	Strangeness enhancement	41
II-C	Comparison with elementary systems	44
3	ALICE: A Large Ion Collider Experiment	47
I	The CERN	47
I-A	The organisation	47
I-B	The accelerator complex	49
I-C	The accelerator programme	52
II	The ALICE collaboration	54
II-A	The collaboration	54
II-B	The detector	55
II-B.i	Inner Tracking System	59
II-B.ii	Time Projection Chamber	61
II-B.iii	VZERO	64
II-B.iv	Time-Of-Flight detector	66

II-C	Trigger system and data acquisition	70
II-D	The event reconstruction	73
II-D.i	Preliminary determination of the primary vertex	73
II-D.ii	Track reconstruction	73
II-D.iii	Final determination of the primary vertex	79
II-E	The ALICE offline framework	79
II-E.i	The computing model	79
II-E.ii	The analysis framework, AliRoot	82
II-E.iii	Data formats	82
II-E.iv	Monte Carlo data	83
4	Identification of V0 particles and cascades	85
I	The appealing features of strangeness	85
I-A	The strange quark with respect to the other flavours	85
I-B	The specificity of strange hadrons	86
II	The multi-strange baryon identification	86
II-A	The V0 and cascade decays	87
II-B	The principles of the topological reconstruction	89
II-B.i	Formation of the V0 candidates	90
II-B.ii	The reconstruction of cascade candidates	90
II-B.iii	Invariant mass of the cascade candidates	93
II-C	The context of hyperon reconstruction in ALICE	94
5	Mass measurements of multi-strange baryons in pp collisions at $\sqrt{s} = 13$ TeV	97
6	Analysis of the correlated production of strange hadrons	99
7	Discussion and conclusion	101
	References	103

Chapter

1 | Preface

All known phenomena observed in Nature can presently be described by four fundamental interactions: the gravitational, electromagnetic, strong and weak interactions. The comprehension of these forces was at the heart of research in Physics throughout the XIXth and XXth centuries. This endeavor led to the two pillars of modern physics: Einstein’s theory of general relativity, in which gravity is a geometric effect of the topology – in particular, the curvature – of spacetime, and the Standard Model of particle physics. In the latter case, the three other forces are understood as an exchange of elementary particles (vector gauge bosons or quanta) of their underlying quantum field.

Within the framework of the Standard Model, the strong interaction is described by quantum chromodynamics (QCD). In this theory, the *quarks* — the elementary particles sensitive to this force — carry a *colour* charge¹, that allows the exchange of *gluons*, the vector gauge bosons of QCD. The peculiarity of this theory resides in its non-Abelian structure, meaning that gluons themselves are colour-charged and thereby can self-interact. The direct consequence of such feature is the running of the QCD coupling constant with the energy scale. In processes involving large momentum transfers (or at short length scale), the coupling constant weakens and the partons – quarks and gluons – can be viewed as free particles, leading to asymptotic freedom. Conversely, for lower momentum exchange (or at larger distance, typically of the order of the proton size), the coupling increases forcing partons to be confined inside composite objects, named hadrons, made of two or three valence quarks: the *mesons* and *baryons* respectively. In this regime, QCD calculations can only be achieved via non-perturbative approaches. One of these reveals another compelling feature: Lattice QCD (lQCD) predicts a phase transition from hadronic to partonic matter at extremely high temperature and/or densities; since the partons are deconfined and – similarly to plasmas – interact weakly, this state of matter is called the *quark-gluon plasma* (QGP). It is believed to have been the state of the primordial Universe, during the first microseconds of its existence, and could be present nowadays on a large scale in the core of neutron stars.

¹This is the analog of the electric charge in QCD.

This QGP is not only a concept, it is an experimental fact. Although the first studies date from the 1970's [1][2][3], research on the QGP took off in 2000 with the hint of its existence by the experiments of the CERN (European Organisation for Nuclear Research) heavy ion programme [4]. This was validated later, in 2005, by the experiments at the Relativistic Heavy Ion Collider (Brookhaven National Laboratory) [5][6][7][8][9].

Experimentally, the QGP is recreated in laboratory by colliding heavy nuclei (Xe, Au, Pb,...) at extremely high energies. Due to its fleeting existence of about $10^{-23}s$, the study of this exotic state of matter relies primarily on the observation of the footprints/signatures left after the collision. The exploration of the QGP also hinges on more elemental collisions, namely proton-nucleus and proton-proton (pp) collisions, where no QGP is foreseen and which are therefore used as a reference.

Among the various available probes of the QGP, the multi-strange baryons, Ξ and Ω containing two or three *strange* quarks, play a special role. Being between light and heavy particles from the flavour point of view, they constitute exotic hadrons abundantly produced in high energy collision, that provide effective constraints on statistical models. Furthermore, thanks to a characteristic decay topology (cascade), their identification is possible on a vast domain of transverse momentum, associated with different production mechanisms (eventually intertwined). Finally, one key signature of the QGP is the *strangeness enhancement*, which consists in the increased yields of strange quarks and thus, in the final state, of strange hadrons. In particular, this enhancement intensifies for hadrons with the largest strangeness content, namely the Ξ and Ω .

Nowadays, the experiment at CERN devoted to studying QCD- and QGP-physics is *A Large Ion Collider Experiment* (ALICE), installed on the ring of the *Large Hadron Collider* (LHC). After two campaigns of data taking in 2009-2013 (Run-1) and 2015-2018 (Run-2), the LHC accelerator has restarted on the 5th of July 2022 for a four-year programme (Run-3) [10]. During the second long shutdown period of the collider (2018-2022), ALICE has been fully revamped and comes out now as a brand-new experiment: more precision Inner Tracking System with reduced material budget; improved readout for its Time Projection Chamber; installation of a Muon Forward Tracker; upgraded detectors joined with a new Online-Offline software to enable continuous readout of Pb-Pb collisions to interaction rate up to 50 kHz [11]. Thanks to these upgrades, the study of QCD- and QGP-physics at LHC enters into a new age, an era of "precision".

About precision, it is enlightening to wonder what it truly means; after all, no one performs unprecise measurements. In the present context, this encompasses two aspects: on one hand, a thorough exploration/characterisation of the object of study with new observables or previously impossible measurements now at reach; on the other hand, accurate measurements going well beyond the current statistical or systematic limitations. In this respect, looking back at the achievements from the previous rounds of data taking, namely LHC Run-1 and Run-2, they are – to a certain extent – plenty of measurements, especially in the light flavour sector. For instance, we can mention [12][13][14].

This thesis proposes pursuing this precision endeavor on multi-strange baryons

thanks to the excellent tracking and identification capabilities (at mid-rapidity) of ALICE during the LHC Run-2. The focus is on pp collisions at a centre-of-mass energy of $\sqrt{s} = 13$ TeV. During this three-year PhD spanning from 2020 to 2023, two analyses have been performed; each one being appropriately introduced and detailed in a dedicated chapter.

The manuscript opens with an introduction of particle physics in Chap. 2. The basic concepts of the Standard Model are presented, with a detailed description of the strong interaction. The notion of QGP is also explained, from its formation to its experimental signatures. Among these, the phenomenon of strangeness enhancement receives a more particular attention.

It is followed by the Chap. 3, that provides an overview of the ALICE collaboration. First, the direct surroundings of ALICE is depicted, that is the CERN, its accelerator complex and the main experiments installed on the ring of the LHC. Then, the internal structure of the collaboration is presented, shortly accompanied by the showcase of the main sub-detectors of ALICE and particularly the ones used in the analyses reported in this manuscript. The event, vertex and tracks reconstruction procedures are outlined.

The Chap. 4 lays emphasis on the technique employed for identifying and selecting the characteristic cascade decay of the multi-strange baryons Ξ and Ω . What makes ALICE unique, among the LHC experiments, for studying those particles in the context of this thesis is also presented.

The Chap. 5 provides a detailed description of the first analysis of multi-strange baryons. It consists in measuring the Ξ^- , $\bar{\Xi}^+$, Ω^- , $\bar{\Omega}^+$ masses and mass differences between particle and anti-particle in pp collisions at $\sqrt{s} = 13$ TeV. The values of the latter offer the opportunity to test the validity of the CPT symmetry to an unprecedented level of precision in the multi-strange baryon sector. This chapter underlines the challenge and the difficulties that one faces with such a measurement.

A second analysis has been carried out based on the experience gained from the first one. It is detailed in Chap. 6. It aims at studying the correlated production of strange hadrons in order to shed more light on the origin of the strangeness enhancement in pp collisions. The physical interpretation of the results is based on the comparison of our measurement to various QCD-inspired Monte Carlo models. The primary focus is to correlate a multi-strange baryon (Ξ or Ω) with a $\phi(1020)$ resonance ($s\bar{s}$), but other kind of correlations are also considered.

The final chapter, Chap. 7, consists in a discussion on the results of both analysis. Different extensions of the present work are also proposed.

Chapter

2 | Particle physics

Particle physics can fairly be defined as the field of Physics dedicated to the study of fundamental particles and their interactions. The idea that matter is composed of elementary bricks is not contemporary, though; the philosophical foundations of this idea date back to the Hellenic epoch in the Ancient Greece (Vth century BC)¹ [15]. With the advent of the scientific method, this concept resurfaces throughout the XIXth and XXth centuries with, among the most notables, John Dalton's atomic theory² and the discovery of the electron by Joseph J. Thomson [16]. Although the first known particle, the electron, was discovered in 1897, research on particle physics gained momentum in the 1950s, thanks to the development of the particle accelerators. These devices made possible to observe high-energy collisions of known particles under controlled laboratory conditions and revealed the existence of dozens of particles: discovery of the pion [17] and kaon in cosmic rays in 1947 [18], followed by the ones of the Λ in 1950 [19], the anti-proton in 1955 [20], the electron and muon neutrinos in 1956 [21] and 1962 [22] respectively, the Ξ in 1964 [23], etc. In total, more than 30 new particles were found by the early 1960s [24] and it was still increasing. This particle "zoo" confused physicists for a decade. It is not until the 1970s that, thanks to the interplay between theory and experiment, a model successfully provided a unified description of these hundreds of particles: they are, in fact, composite objects, made of smaller and fewer constituents. This model still represents the best description of the sub-atomic universe to this day, hence its well-deserved name: the Standard Model of particle physics.

Throughout this chapter, an effort will be made to provide a historical introduction of the modern particle physics, with a particular attention on the many architects that contributed to its construction. The first section, Sec. I, presents the Standard Model starting with some mandatory theoretical aspects. This is followed by the description of the different fundamental particles and interactions, that will ultimately lead to the classification of the elementary particles of the Stan-

¹The fathers of the Atomism from the Ancient Greece, Leucippus and Democritus, thought that matter was made of both void and elementary, indivisible corpuscles: atoms.

²Apart from the name, it does not share much with the philosophical reasoning from the Ancient Greece.

dard Model. The theory of the strong interaction — the quantum chromodynamics (QCD) — will profit of a dedicated sub-section, considering its central role in the present manuscript. The different aspects of this force will be discussed, particularly the QCD phase diagram. One of the fascinating phases of QCD matter consists in state of matter in which quarks and gluons are no longer confined within hadrons: the quark-gluon plasma. Such a state — supposedly corresponding to the primordial state of the Universe a few micro-seconds after the Big Bang — is the heart of the Sec. II. The formation of the QGP in laboratory will be presented, as well as its experimental signatures. One of them, called the strangeness enhancement, stands out of the others, since it has a central role in the studies described in this manuscript. Finally, this chapter will close on a discussion on the different probes of the QGP in view of the “recent” results in elementary systems, namely pp and p-Pb collisions.

I The Standard Model of particle physics

I-A Quantum field theories and fundamental symmetries

Mathematically speaking, the Standard Model is a (relativistic) quantum field theory (QFT), whose dynamics and kinematics are typically described by a Lagrangian³. In this formalism, particles are expressed in terms of dynamical fields defined at all points of spacetime [26]. The construction of the Standard Model relies strongly on group theory and symmetries (or invariances). In essence, the procedure for building a QFT consists in i) specifying a set of symmetries and their associated symmetry group, and ii) writing down the most general Lagrangian that is renormalizable and satisfies the postulated symmetries [27].

There are different classes of symmetries. A transformation that keeps the Lagrangian invariant and applies simultaneously at all points is called a *global* symmetry. Conversely, a similar transformation that would be applied differently at each point is a *local* symmetry. Both global and local symmetries can also be *continuous* if the transformation consists in a sum of infinitesimal transformations – typically described by Lie groups – or *discrete* and represented by finite groups [26]⁴. Continuous symmetries are particularly interesting because of the Noether’s theorem [28] that fundamentally states: to every continuous symmetry, there corresponds a conserved physical quantity (and vice versa).

All QFTs assume global Poincaré invariance, that involves spacetime translations and global Lorentz transformations including rotations in space and boosts. All these symmetries are continuous, and result in the conservation of momentum, energy, angular momentum and the speed of light respectively. The key elements that defines the Standard Model stem, in fact, from a subset of continuous and local symmetries: the *gauge* invariances. Each of these internal symmetries is associated

³The choice of a Lagrangian formulation is motivated, at least partially, by the fact that symmetries in the Lagrangian lead directly to conserved quantities/currents [25].

⁴There is also an additional difference concerning the quantum numbers: for a continuous symmetry, quantum numbers are additives; for a discrete one, they are multiplicatives [27].

to a certain number of group generators, from which emerge (vector) fields – called the *gauge* fields – describing a fundamental interaction. Intuitively, a gauge symmetry corresponds to an invariance under a change of scale or, in other words, of *gauge* [29]. For example, the electrostatic field depends on the potential difference and not the potential itself. This means that the electrostatic field is invariant under a shift of the potential. Additionally, the potential is defined within an additive constant, which corresponds to a *global gauge* [27].

Finally, the Standard Model also relies on discrete symmetries: parity (P), time reversal (T) and charge conjugation (C). Although, most of the interactions preserve these three transformations, this must not be taken for granted. In the current state of the Universe, they are all broken and only the combination of C, P and T still holds as an exact symmetry of Nature [30]. That is closely connected with the Lorentz invariance via the so-called CPT theorem [31], which states that any unitary, local, Lorentz-invariant quantum field theory in a flat Minkowski spacetime must also be CPT invariant and vice-versa [31][32]. This being said, one can easily imagine that CPT invariance stands as one of the most sacred symmetry in the Standard Model. One of the implication of the CPT theorem involves the properties of matter and antimatter: since the combination C, P and T consists in a mirror-image transformation of particles into antiparticles, the CPT symmetry imposes that they share the same invariant mass, energy spectra, lifetime, coupling constants, etc [31][13].

I-B Particles and fundamental interactions

The Standard Model provides a description of the fundamental constituents of the observable Universe, the *elementary particles*, and their interactions, the *forces*. This description encompasses three of the four known fundamental forces: electromagnetic, strong and weak interactions. Gravity is not included for two reasons: on the theoretical side, this force is governed by the laws of general relativity. Its description within an unified framework with the three other interactions turns out to be a difficult – if not impossible – task. Furthermore, the coupling strength of gravity is by far the weakest of all the known forces, making it impossible to study experimentally at microscopic scales. Tab. 2.1 compiles some properties of the different forces.

The strong interaction, as the name suggests, is the strongest of the four fundamental forces; it is responsible for the cohesion of protons, and neutrons inside the nuclei (also called the nuclear force), for more than 99% of the observable mass in the Universe and for the confinement of the quarks (explained later in this section and in I-C.i). It has a limited range, though, of only a few fm. On the opposite side, the weakest of the non gravitational forces is the weak interaction, which also has the shortest effective range (about less than a fm). The radioactive decay – as well as the decay of the particles studied in this thesis – and the fusion of atoms in the Sun originate from this force. Finally, the electromagnetic interaction is certainly the one we are the most familiar with; its coupling strength is in between the strong and weak forces, its range is infinite.

Interaction (Force)	Particles Acted on by Force	Relative Strength	Typical Lifetimes for Decays via a Given Interaction	Range of Force
Strong	Quarks, hadrons	1	$\leq 10^{-20}$ s	1 fm
Electromagnetic	Charged particles	$\approx 10^{-2}$	$\approx 10^{-16}$ s	∞
Weak	Quarks, leptons	$\approx 10^{-6}$	$\geq 10^{-10}$ s	10^{-3} fm
Gravitational	All particles	$\approx 10^{-43}$?	∞

Table 2.1: The four fundamental interactions, with their corresponding relative strengths, typical lifetime for a decay and range. The relative strengths are indicative values; obviously, they depend on the distance and energy scale considered. Here, they have been calculated for two particles at a distance of 0.03 fm. Table taken from [24].

These forces act on the fundamental constituents of matter, the quarks⁵ and leptons⁶, which are point-like fermions of spin 1/2. They are twelve organised in three families or generations, each containing two quarks with fractional electric charges (one with $+2e/3$ and the other with $-1e/3$, where e corresponds to the electric charge of the positron), one charged lepton and a neutrino⁷. The first family (or generation I) consists of the up and down quarks, the electron and the electron neutrino. These are the elements that characterize our low-energy Universe: the quarks make up the nucleons, forming the atomic nuclei, and with the electrons, they constitute the basic building blocks of all earthly matter. The electron-neutrino also plays a role in our everyday Universe, although an indirect one. Without its existence, the primordial hydrogen could not have been transformed into a variety of light and vital elements [34] for the development of life. The particles belonging to the first family can be duplicated to form the second and third families. Higher-generation particles have the exact same physical properties as their first-generation cousins, except for the mass that increases with the generation. Because of this difference, fermions from second and third generations tend to go through a chain of decay processes in order to reach particles from the first family. This is why ordinary matter is generally constituted of first-generation particles. I say *generally* because there are two subtleties when it comes to neutrinos: i) since they only interact via weak interaction and gravity, they cannot aggregate to form ordinary matter⁸ and ii) they can oscillate from one flavour to another, giving rise to the

⁵The term is apparently inspired from Joyce's book *Finnegans Wake*: "Three quarks for muster Mark..." [33].

⁶From the Greek *leptos* meaning "small" to designate particles of small mass. Nowadays, any fermion that is insensitive to the strong interaction is tagged as a lepton [33].

⁷From the Italian "neutro" for "neutral" and the suffix "ino" for "tiny one", so "neutrino" means the "tiny neutral one" [33].

⁸Because the weak interaction only acts at a short distance, and the intensity of the gravitational

phenomenon of neutrino oscillation.

A final aspect concerns the *chirality* of the fermions, that is traditionnally introduced by concept of the helicity or handedness. Both are equivalent in the ultra-relativistic limit. On one hand, a particle exists in two versions: *right-handed* if the direction of spin coincides with the direction of motion; *left-handed* if the directions of spin and motion are opposite [35]. On the other hand, the chirality also has its own *left-* and *right-handed* states but the concept is more abstract. The chirality determines under which representation of the Poincaré group the particle transforms [36].

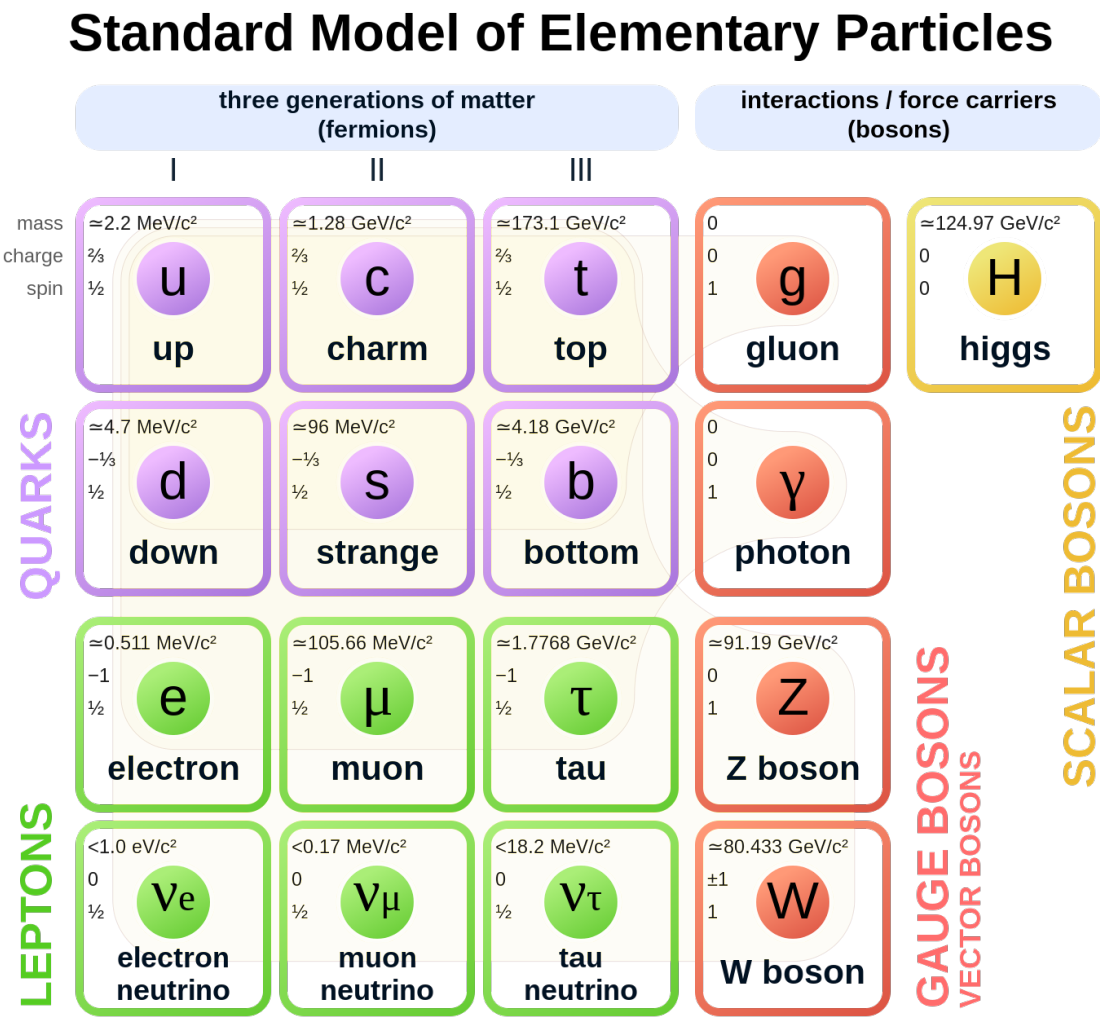


Fig. 2.1: Classification of the elementary particles of the Standard Model, with the fermions on the left and the gauge/scalar bosons on the right. Figure taken from [37].

Classically, a particle interacts with another via a field (for example, in electromagnetism, a positively charged particle generates an electric field that exerts an

force is minuscule considering the extremely small mass of neutrinos.

attractive/repulsive force on neighboring negative/positive charge). In QFT, fields are quantized, and the energy and momentum previously carried by the field are now conveyed by chunks, by quanta⁹ [24]. So in particle physics, interactions are described as an exchange of quanta or force-carrying particles of spin 1, known as *(vector) gauge bosons*¹⁰[27][35]. Following the remarks in Sec. I-A, the term "*(vector) gauge*" emphasizes here the fact that the boson arises from a gauge vector field and therefore a gauge symmetry.

The most precise quantum field theory is the quantum electrodynamics (QED) that describes the interaction between charged particles and electromagnetic fields. It has been developed between 1947 and 1949 by Shin'-ichirō Tomonaga, Julian Schwinger, Richard P. Feynman and Freeman Dyson; only the first three received the 1965 Nobel Prize in Physics for their contributions¹¹. It is based on a U(1) local gauge symmetry¹², that results into an interaction with charged particles mediated by massless photons. This continuous symmetry is associated to a conserved quantity, namely the electric charge. The dynamics of this interaction is given by the Lagrangian density of QED in Eq. 2.1.

$$\mathcal{L}_{QED} = \underbrace{i\bar{\psi}\gamma^\mu\partial_\mu\psi}_{\text{electron kinetic term}} + \underbrace{e\bar{\psi}\gamma^\mu A_\mu\psi}_{\text{electron-photon interaction term}} - \underbrace{m\bar{\psi}\psi}_{\text{electron mass term}} - \underbrace{\frac{1}{4}F_{\mu\nu}F^{\mu\nu}}_{\text{photon kinetic term}} \quad (2.1)$$

where

- γ^μ Dirac matrices that express the vectorial nature of the interaction and μ is the Lorentz vector index,
- A_μ the photon field,
- $F_{\mu\nu} = \partial_\mu A_\nu - \partial_\nu A_\mu$ the field-strength tensor,
- e the coupling constant of QED which coincides with the electric charge of the electron-positron field,
- m the electron/positron mass,
- ψ the electron-positron spinor field,

with the Einstein's notation $x^\mu x_\mu = \sum_{\mu=0}^N x^\mu x_\mu$ and the notations from [35].

Different terms appear in the expression of the Lagrangian density: the density of kinetic energy of the spinor field, the density of potential energy due to the

⁹Here, we present elementary particles as quanta of their underlying field as if the particles could be separated/reduced from their field, which corresponds to the usual experimentalist's picture of QFT. In fact, the relation between particles and fields is slightly more subtle [38].

¹⁰They are called *bosons* because, contrarily to the fermions, their intrinsic angular momentum (or spin) has an integer value.

¹¹Unfortunately F. Dyson did not receive the Nobel Prize because i) his work was not considered as groundbreaking as the one of the three other laureates and ii) the Nobel Prize in a given field can only be awarded to organisation of maximum of three individuals [39].

¹²U(N) corresponds to the group of all unitary matrices to size $N \times N$. Thus, U(1) is a group containing all the continuous transformations of the phase of a complex number.

interaction between the spinor and gauge fields, the mass energy of the spinor field¹³, the density of kinetic energy of the gauge boson (photon). The most interesting term is the second one, which describes the interaction between the charged particles and the photons. This interaction gives rise to different processes, usually pictured by Feynman diagrams. Fig. 2.2 shows the basic interaction vertex in QED.

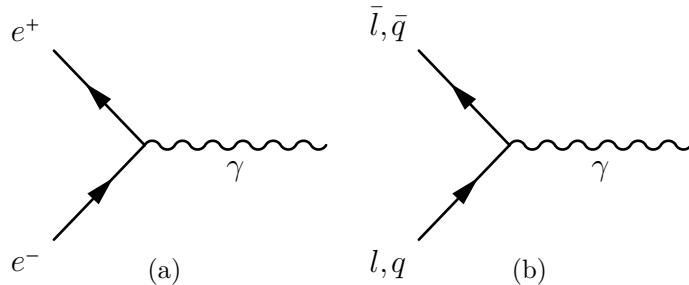


Fig. 2.2: Interaction vertex in QED: (a) involving an electron and a positron, (b) generalized to any charged particles.

Being the first quantum field theory developed, QED paved the way – and even served as a template – for all the subsequent quantum field theories. Therefore, it is not surprising that the form of Lagrangian density is the same for all the forces.

Following the success of QED, attempts to develop a quantum field theory for the weak interaction started in the 1950s; none of them could provide a satisfactory description. In the same decade, important discoveries have been made: the Wu's¹⁴ (1956) and Goldhaber's (1957) experiments [40][41] showed that the P- and CP-symmetries are violated by the weak interaction. These led to conclude that this force has a vector-axial vector structure, meaning that only interacts with left-handed chiral particles and right-handed chiral anti-particles. Meanwhile, a few physicists – including Abdus Salam, Steven Weinberg, Schwinger and his PhD student Sheldon L. Glashow – foresaw that the weak and electromagnetic forces might be two aspects of the same phenomenon. Thanks to the work of Chen Ning Yang and Robert Mills on the development of a generalized gauge theory in 1954, Glashow delivered the electroweak interaction in 1961, which was consolidated later in 1967 and 1968 by Weinberg and Salam¹⁵ respectively. In this quantum field theory, the electromagnetic and weak forces are described within an unified framework; the weak interaction is based on the $SU(2)$ gauge group¹⁶, three generators hence three gauge bosons: W^+ , W^- and Z^0 . These bosons exhibit two unique properties. First, contrarily to all other gauge bosons, these ones have an enormous mass ($m_{W^\pm} = 80.377 \text{ GeV}/c^2$ and $m_{Z^0} = 91.1876 \text{ GeV}/c^2$ [42]), which explains why the weak force is such a short-range interaction. Second, the W^\pm bosons can change the flavour of quarks and leptons. The trend (or the probability) of the flavour-changing is given

¹³If the gauge boson is massive, there would be an extra mass term. Since the photon is massless, this term is null.

¹⁴Awarded of the 1957 Nobel Prize.

¹⁵For their contribution, Glashow, Salam and Weinberg receive the 1979 Nobel Prize.

¹⁶The S (for "special") refers to the group of all matrices whose determinant is equal to 1.

by the Cabibbo-Kobayashi-Maskawa¹⁷ (CKM) matrix [42]¹⁸ in Eq. 2.2.

$$V_{\text{CKM}} = \begin{pmatrix} V_{ud} & V_{us} & V_{ub} \\ V_{cd} & V_{cs} & V_{cb} \\ V_{td} & V_{ts} & V_{tb} \end{pmatrix} = \begin{pmatrix} 0.97425 \pm 0.00022 & 0.2253 \pm 0.0008 & 0.00413 \pm 0.00049 \\ 0.225 \pm 0.008 & 0.986 \pm 0.016 & 0.0411 \pm 0.0013 \\ 0.0084 \pm 0.0006 & 0.040 \pm 0.0027 & 1.021 \pm 0.032 \end{pmatrix} \quad (2.2)$$

Each matrix element provides the probability of transition from one flavour i to another j for quarks, but the same exists for the leptons and is called the Pontecorvo-Maki-Nakagawa-Sakata (PMNS) matrix. The elements of the PMNS matrix are slightly different from the CKM ones, though the structure and ordering are the same.

Finally, concerning the strong interaction, we will see later in its dedicated subsection, Sec. I-C. Patience!

The overall picture of the Standard Model's elementary particles is presented in Fig. 2.1. To this figure should be added the antiparticles. Indeed, to each particle – fermion or boson – corresponds an antiparticle that has the same properties, because of the CPT invariance, but with oppositely sign quantum numbers. Consequently, this also means that both CKM and PMNS matrices are the same for particles and antiparticles.

There is, however, one element of the table in the Fig. 2.1 that has not been discussed yet, that is the Higgs boson. It originates from the electroweak unification, so let us retrace our footsteps. The principles of gauge invariance inevitably give rise to massless gauge bosons, like the photons but not the massive W^\pm , Z^0 bosons. At the time of Glashow's electroweak model in 1961, no one could imagine a mechanism to generate the enormous masses of the weak interaction force-carriers. In the same year, Jeffrey Goldstone showed that the process of spontaneous symmetry breaking¹⁹ leads to the existence of massless gauge bosons, called Goldstone bosons. Three years later, in 1964, three independent groups (Robert Brout and François Englert; Peter Higgs; Gerald Guralnik, Carl Richard Hagen, and Tom Kibble) demonstrated the Goldstone bosons could be absorbed by the massless gauge bosons to acquire a mass: this is the Higgs mechanism. It is only in 1967-68, that Weinberg and Salam put to use this mechanism within Glashow's model to generate the masses of W^\pm and Z^0 bosons. But this goes beyond the scope of the electroweak unification; with this

¹⁷The Universe is unfair: similarly to Dyson for the QED, Nicolas Cabibbo (the pioneer of the CKM matrix) was not awarded with the 2008 Nobel Prize, while Makoto Kobayashi and Toshihide Maskawa were.

¹⁸Mathematically speaking, this matrix relates the mass eigenstates to the weak eigenstates [35].

¹⁹This is the phenomenon in which a physical system perfectly symmetric breaks the symmetry without any external intervention. The most famous example of such process concerns the magnets. A material can be seen as an ensemble of microscopic magnets. If this material is ferromagnetic, all these magnets will tend to align with their neighbors. When the temperature increases, the thermal motions start to disrupt this alignment until the material is not magnetized anymore. Conversely, as the material cools down, neighboring magnets starts to align until a critical temperature, when all the magnets lines up in one macroscopic direction. All directions are equivalent but the magnet has to choose one. This choice breaks the symmetric situation when all the directions are equivalent; this is a *symmetry breaking*. Moreover, this choice is not influenced by any external agent, hence it is labelled as *spontaneous*.

mechanism, the mass of all elementary particles can be generated [33]. Incidentally, a new massive spinless particle, associated to a scalar field, emerges out of the Higgs mechanism: the Higgs boson. Its observation in laboratory was at the heart of Standard Model researches for decades until the 14th of March 2013 when the ATLAS and CMS experiments at the LHC at CERN announced the discovery of the Higgs boson [43][44]. The same year, Peter Higgs and François Englert receive the Nobel Prize for their contribution to the Standard Model.

I-C The strong force, a colourful interaction

Back in the 1960s, in the “glorious years” of particle physics, when physicists were submerged by the number of newly discovered “elementary” particles. Some of them were subject to the strong interaction, some were not; the former were referred as *hadrons*²⁰ and the latter as *leptons*, as discussed in Sec. I-B. The hadrons were further sorted into two groups known as *mesons* and *baryons*²¹. But no one could draw out the underlying scheme between these particles and organise them into some kind of periodic table. There were some attempts though [45][46]; however the Mendeleev of particle physics is arguably Murray Gell-Mann.

In 1961, he (and independently Yuval Ne’eman) proposed a classification scheme called the *eightfold way* [47][48]. At that time, eight spinless mesons, eight vector mesons of spin 1 and eight spin 1/2 baryons were known. In each of these octets, a pattern emerges when the hadrons are organized into groups/multiplets of roughly the same mass, a hint of the underlying structure of strong interaction. A year later, the eightfold way is updated and completed with a decuplet formed of spin- $\frac{3}{2}$ baryons. However, one of the ten members of the decuplet was not yet discovered but this periodic table of elementary particles can predict its properties: a mass near the 1675 MeV/ c^2 , strangeness²² of -3 and negatively charged, these are the characteristics of the Ω^- . Its existence is confirmed experimentally in 1964 by the Alternating Gradient Synchrotron at the Brookhaven National Laboratory (BNL)[23], validating the eightfold way once and for all.

Within the year of this discovery, Murray Gell-Mann (and independently Georges Zweig) unveiled the symmetry behind the eightfold way: there are no elementary hadrons; they are, in fact, all built out of more fundamental particles named *quarks*. A composite object made of bosons can only lead to a boson whereas, formed by fermions, the object is either a fermion or a boson depending on the number of constituents involved. Hence, the quarks must be fermions of spin one-half, mesons are

²⁰The expression originates from the Greek *adros* meaning "thick and bulky".

²¹These terms originally refer to the mass of the particle: *meson* comes from the Greek root *meso* for "middle", that is in between the electron and proton masses; *baryon* stem from Greek *barys* for "heavy", suggesting any particle with a mass greater or similar to the one of the nucleons. Before the development of the quark model, the difference between the meson and the baryon was driven by their spin. The meson is a boson (integer spin values) whereas the baryon is a fermion (half-integer spin values)[33].

²²A quantum number introduced by Murray Gell-Mann in 1953 order to explain the *strange* behaviour of some particles, such as kaons [49]. Any particle with a non-zero strangeness value is dubbed *strange particle*.

composed of an even number of quarks, baryons of an odd number. The smallest odd number is one, but i) it does not make sense to say that a composite structure is made of one constituent and ii) we will see later in Sec. I-C.i that a system of one quark is physically impossible. Thus, mesons must be made out of two quarks and baryons out of three; these are the simplest imaginable arrangements.

Originally, quarks exist in two flavours, *up* (u) and *down* (d), with fractional electric charges of $+2e/3$ and $-1e/3$ respectively. But an extra flavour was needed to explain the existence of strange hadrons: the strange quark, s , is born. It has the same properties as the d quark, except that it is much heavier and it has an assigned strangeness number of -1. Any strange hadrons actually contains one to three s quark, depending on their strangeness. Therefore, the predicted particle by the eightfold way, the Ω^- , corresponds actually to the strangest hadron possible, a baryon with three strange quarks.

With this particle comes the first difficulty of the quark model. Whatever the particle, it must obey the spin-statistics theorem. Quarks being fermions, the theorem states that two *identical* fermions can not occupy the same quantum states simultaneously. However, Ω^- is constituted of three exactly identical s -quark [50]. This problem was overcome by Oscar W. Greenberg [51], Moo-Young Han and Yoichiro Nambu [52] in 1964-65 that introduced a new quantum number, the colour. Each quark comes in three colours or variants labelled as red (r), green (g) and blue (b). In this way, the spin-statistics problem is solved but new questions arises. If quarks carry a colour, hadrons are a mixture of colours. This is assumed to be an equal mixture of all the colours, such that the hadrons are colourless. How come? Why are there no coloured hadrons?

Along the same line: in 1966, the main accelerator at the Stanford Linear Accelerator Center (SLAC) becomes operational and starts a program of deep inelastic scattering experiments in order to study the inner structure of nucleons. Based on James Bjorken's [53] and Richard Feynman's [54] calculations, the results of SLAC's experiments, in 1969, showed that the nucleons were made of point-like constituents of spin- $\frac{1}{2}$, dubbed *partons*, behaving as free particles [26]. The partons were nothing else than the quarks, and these observations established the validity the quark picture to the whole particle physics community. However, it is curious that the partons seem to behave as free particles but they can not escape the hadron.

These questions remain unanswered until 1973. This year had seen the development of Quantum Chromodynamics (QCD) – the quantum field theory of the strong force – and the discovery of two of its most salient properties, namely the colour confinement and the asymptotic freedom (discussed in Sec. I-C.i). Fruit of the work of Harald Fritzsch, Heinrich Leutwyler and Murray Gell-Mann [55], the QCD describes the interaction between colour-charged objects, namely the partons. It is based on the gauge symmetry group $SU(3)$, which has eight generators, giving rise to eight massless gauge bosons called *gluons*, and imposes the conservation of colour.

QCD is very similar to QED: the electric charge is replaced by a colour charge, antiparticles carry opposite colour charges, and the eight gluons take the role of the photon. The dynamics of QCD is given by the Lagrangian density in Eq. 2.3.

$$\mathcal{L}_{QCD} = \underbrace{i\bar{\psi}_q^i \gamma^\mu \delta_{ij} \partial_\mu \psi_q^j}_{\text{quark kinetic term}} + \underbrace{g_s \bar{\psi}_q^i \gamma^\mu t_{ij}^a A_\mu^a \psi_q^j}_{\text{quark-gluon interaction term}} - \underbrace{m_q \bar{\psi}_q^i \psi_q^i}_{\text{quark mass term}} - \underbrace{\frac{1}{4} F_{\mu\nu}^a F^{a\mu\nu}}_{\text{gluon kinetic term}} \quad (2.3)$$

where, using the notations from [50],

- $g_s^2 = 4\pi\alpha_s$ with α_s the coupling constant of QCD,
- $F_{\mu\nu}^a = \underbrace{\partial_\mu A_\nu^a - \partial_\nu A_\mu^a}_{\text{Abelian part}} + \underbrace{g_s f^{abc} A_\mu^b A_\nu^c}_{\text{non-Abelian part}}$ the field-strength tensor,
- ψ_q^i the quark field spinor with colour index i such that $\psi_q = (\psi_{qR}, \psi_{qG}, \psi_{qB})^T$,
- m_q the quark *bare* mass induced by the Higgs mechanism,
- A_μ^a the gluon field with colour index a ,
- $t_{ij}^a = \frac{1}{2}\lambda_{ij}^a$ and λ^a the fundamental²³ representation of the generator of SU(3) associated to the colour index a ,
- f^{abc} the structure constants of SU(3).

As in QED, the Lagrangian density can be expressed with four terms; the quark-gluon interaction is described by the second one. However, the field-strength tensor $F_{\mu\nu}^a$ here admits an extra term because the generators of SU(3) do not commute. The non-Abelian property of the gauge group of QCD gives rise to gluon-self interactions, as shown in the Feynman's diagrams of Fig. 2.3.

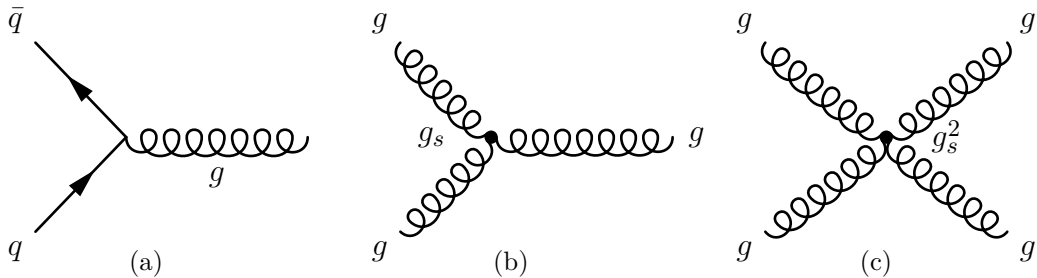


Fig. 2.3: The three possible interaction vertices within the framework of QCD: (a) quark-gluon, (b) triple-gluon and (c) four-gluon interactions.

Consequently to the self-interaction of QCD's force-carriers, gluons can not be colour neutral. To ensure colour conservation at the interaction vertex in Fig. 2.3(a), the gluon must carry a colour and an anti-colour charges. This calls for a revision of the term *partons*: it corresponds to any colour-charged elementary particle, that is the quarks *and* gluons.

²³The representation of a group is *fundamental* when its generators are hermitian and traceless matrices.

Furthermore, quarks are bound together inside hadrons through the exchange of gluons, but because of their self-interaction feature, gluons can radiate other gluons (Fig. 2.3(b)); the latters can, in turn, split into a quark-antiquark pair (Fig. 2.3(a)) or emit gluons again, and so on. The static picture of hadrons with two or three quarks exchanging gluons turns out to be more complex, permeated in a *sea* of quarks (and antiquarks) and gluons²⁴. However, the elements inside the sea do not determine the quantum numbers or properties of the hadron, as opposed to the "original" quarks; for this reason, the latter are often referred as *valence quarks*.

Finally, an incidental consequence of gluon's self-interaction is the running of the coupling constant. This can be understood by making a (anti)parallel with QED. Let us say we want to measure the coupling strength with a charged particle (an electron, for example). In QFT, the vacuum is not entirely empty, it contains pairs of particles and antiparticles that are constantly created and annihilated. Such a pair can also be formed by the cloud of *virtual*²⁵ photons surrounding the charged particle to be tested; in this case, it is said to *polarise the vacuum*. An example of this process can be found in Fig. 2.4(a). The positively charged particle from the vacuum is attracted to the initial electron, leading in a screening effect similar to the one found in a dielectric material (Fig. 2.4(b)). At large distance (or small energy), it is more difficult to penetrate inside the cloud of virtual particle-antiparticle pairs and to probe the initial charge, reducing the coupling strength. Conversely, at small distance (or large energy), the initial charge can be distinguished from the surrounding positively charged particles and the coupling strengthens. In QCD, the opposite happens. Because gluons carry a colour charge, the initial colour of the particle to be tested (a quark) gets spread out, as depicted in Fig. 2.4(c). Thus, an anti-screening effect occurs: the initial red-coloured quark spends most of its time coloured as blue or green, and the red colour charge is diluted in the surrounding cloud of partons. At large distance (or small energy), the initial quark r is overly apparent for an incoming gluon $\bar{r}g$ or $\bar{r}b$; conversely, at small distance (large energy), the initial red quark – likely converted into a green or blue quark – is invisible to such a gluon, resulting in a weakening of the coupling strength.

Before continuing, allow me to digress and finish with the different quarks within the QCD framework. The alert reader may have guessed that the story did not end with the strange quark. In 1964, James Bjorken and Sheldon Glashow introduced a new quark flavour: the charm quark. It is motivated by the idea of a quark-lepton symmetry²⁶ at that time, there were four known leptons (electron, muon and their associated neutrinos) and three quarks. But the charm quark definitely comes into play in 1970 by Sheldon Glashow (again), John Iliopoulos and Luciano Maiani to

²⁴An effect of the sea of quarks and gluons is the Bjorken scaling violation observed by the HERA experiment [27][35].

²⁵Certainly the most vague concept in particle physics. It appears in perturbation theory (see later) and an attempt for a definition could be: it corresponds to a theoretical particle which exhibits the same properties as ordinary particles but not necessarily (for example, they do not satisfy the energy-momentum relation), and with a lifetime so short that it could never be observed experimentally.

²⁶The term *charm* is chosen for designating this fourth flavour because the definition found by Bjorken and Glashow in *American Heritage Dictionary*: "an action or formula thought to have magical power", implying magical power to restore the quark-lepton symmetry [33].

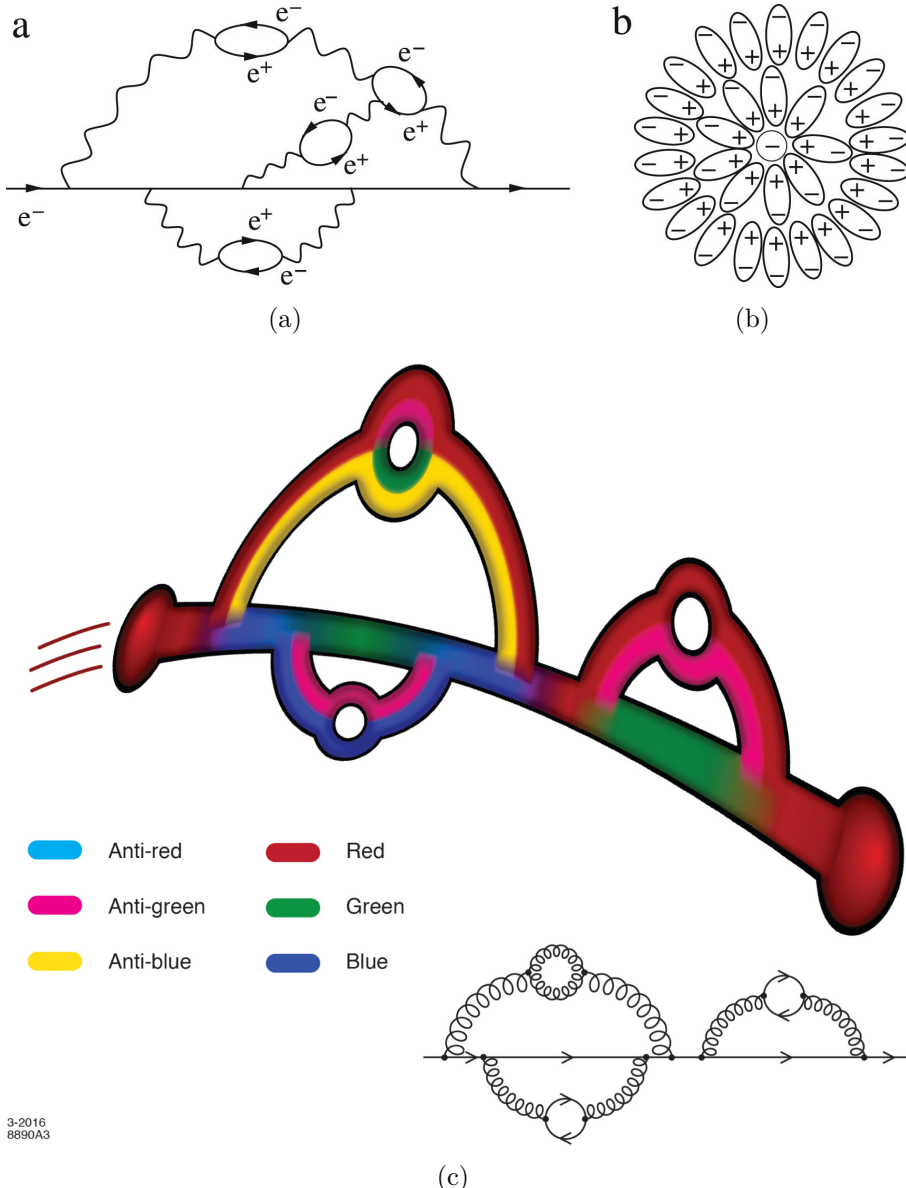


Fig. 2.4: (a) screening effect of an electron in QED, induced ;(b) analogy with the screening effect in a dielectric material; (c) pictorial representation of the colour spread of an initially red coloured quark.

explain the strangeness-changing neutral currents²⁷. Its existence is validated by the observation of the first charmed hadron in 1974 by Burton Richter (SLAC)[56] and Samuel Chao Chung Ting (BNL)[57]; both receive the 1976 Nobel Prize for that discovery. In parallel, a third generation of quark is introduced, in 1972 by

²⁷This is typically the case of the decay of a negative kaon to a negative pion with a neutrino and an anti-neutrino ($K^- \rightarrow \pi^- \nu \bar{\nu}$). It is called a strangeness-changing neutral current because i) the strange particle (kaon) changed into an ordinary one (pion), and ii) there is no electric (or neutral) charge transfer between the hadrons to the leptons. This process was never observed in laboratory, as opposed to the strangeness-changing charged current: ($K^- \rightarrow \pi^0 e^- \bar{\nu}_e$). To eliminate the strangeness-changing neutral currents, a new quark flavour needed to be introduced [33].

Makoto Kobayashi and Toshihide Maskawa²⁸ to explain the observed CP violation. The particles composing this new family make their appearance in 1975, thanks to Haim Harari [58], under the name of *bottom* and *top* quarks²⁹. Evidence of the bottom quark is found in 1977 by Leon M. Lederman at Fermilab [59]. Due to its large mass, the discovery of the top quark takes more time but ultimately occurs in 1995 by two groups at Fermilab [60][61].

I-C.i Running of α_s , colour confinement and asymptotic freedom

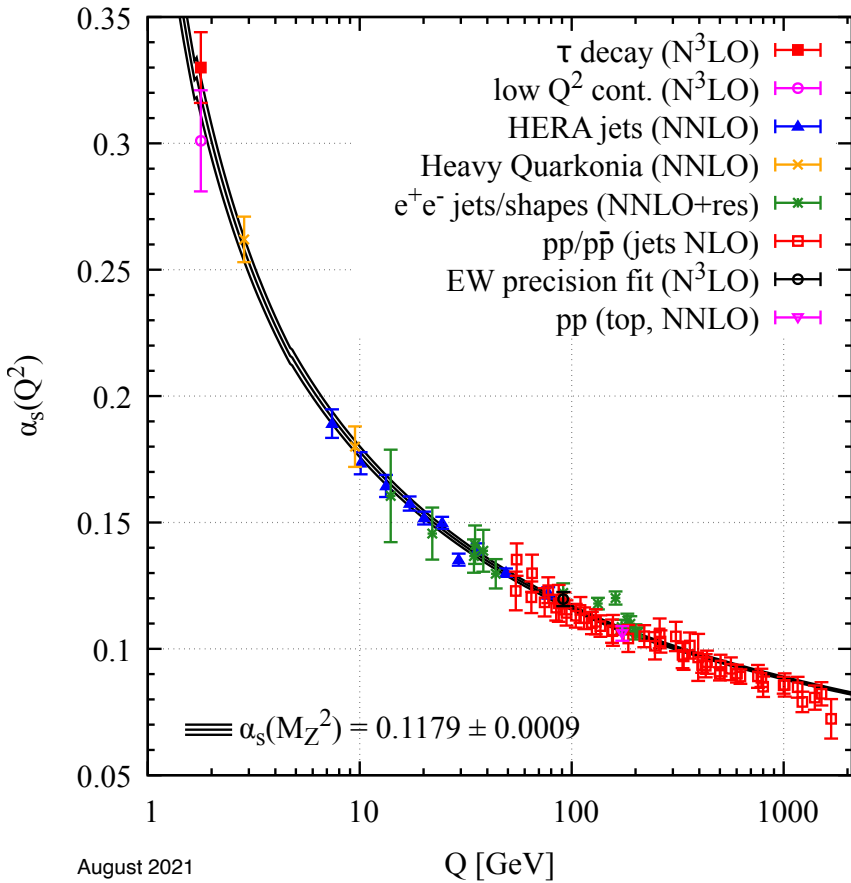


Fig. 2.5: Running of the coupling constant of the strong interaction, α_s , as a function of the energy transfer Q . The markers represent measurements based on perturbative calculation (the order of the perturbation development is indicated in parenthesis), the solid line corresponds to analytical prediction. Figure taken from [42].

Fig. 2.5 shows the running of the coupling constant α_s of QCD as a function of the energy transfer Q . The strength of the interaction varies considerably, such

²⁸For the discovery of, at least, a third family of quarks, they both receive the 2008 Nobel Prize.

²⁹Both belong to the same weak isospin doublet, as are the down and up quarks. To match the labelling of the first generation of quarks, the names *bottom* and *top* were chosen.

that two regimes can be discerned: one at large Q (or small distance) when the strong interaction is "weak" (α_s small), the other at small Q (or large distance) when the coupling constant gets "strong" (α_s large). Usually, these two regimes are delimited by defining an energy scale, denoted as Λ_{QCD} , at which $\alpha_s \sim 1$. This corresponds to $\Lambda_{\text{QCD}} \sim 200 \text{ MeV}^{30}$. Far above this value, the contribution of high-order diagrams decreases with their order such that most of them can be neglected, and QCD predictions can be calculated easily – or in some cases, it simply renders the calculations possible – using perturbation theory. In this case, we talk about perturbative QCD (pQCD).

As the energy transfer decreases, the coupling constant increases and perturbative calculations start to diverge until the point where it becomes infinite, at Λ_{QCD} . At this value or below, QCD is dominated by the contributions from high-order diagrams and can no longer be treated perturbatively anymore. The only way out is to perform analytical calculations, which is not possible due to the complexity of QCD. A more viable option is to resort to numerical calculations. A well-established technique is called *lattice QCD*, where to each (space-time) point of the lattice/-grid corresponds a spinor field representing the quarks possibly connected (or not) by links describing the gluon vector field. Although it provides some insights on non-perturbative physics aspects of QCD, it is extremely demanding in terms of computational power and time – these two factors being strongly dependent on the lattice size.

A phenomenological approach of QCD, supported by lattice calculations, can also be followed by considering that the interaction potential between two quarks separated by a distance r is approximated by³¹

$$V(r) \approx -\frac{\alpha_s(r)}{r} + \kappa r, \quad (2.4)$$

where the constant κ is typically about 1 GeV/fm [62]. The alert reader recognises the first term as the Coulombian-potential, similar to the one in QED; the second term corresponds to an elastic spring-type force. As illustrated in Fig. 2.6, they describe two specific behaviours of the QCD interaction potential.

At small distance ($r \leq 0.1 \text{ fm}$), the Coulomb-type term dominates, the interaction potential diminishes asymptotically as the distance decreases; it is not divergent though, as α_s also varies. The quarks interact less and less, and becomes quasi-free. This phenomenon, known as *asymptotic freedom*, has been discovered by David Gross, Frank Wilczek in 1973 [64] and Hugh David Politzer in 1974 [65], and sets the groundwork for the development of a quantum field theory of strong interaction, that is the QCD³². Neither the electrostatic force between two charges nor the

³⁰The definition of Λ_{QCD} is convenient because it allows to classify quarks as a function of their mass hierarchy with respect to Λ_{QCD} : u , d and s quarks belong to the light-flavour sector ($\Lambda_{\text{QCD}} \ll m_s, m_u, m_d$), the others are heavy-flavour quarks ($m_t, m_b, m_c \gg \Lambda_{\text{QCD}}$).

³¹The expression of the potential is experimentally motivated by the ordering in the spectra of the charmonium ($c\bar{c}$) and bottomonium ($b\bar{b}$) bound states [35] [62].

³²In the early seventies, the common belief among the theoreticians was that quantum field theory fails to describe the strong interaction, and therefore it would be impossible to have a common mathematical framework for all the known forces (except gravity) [33].

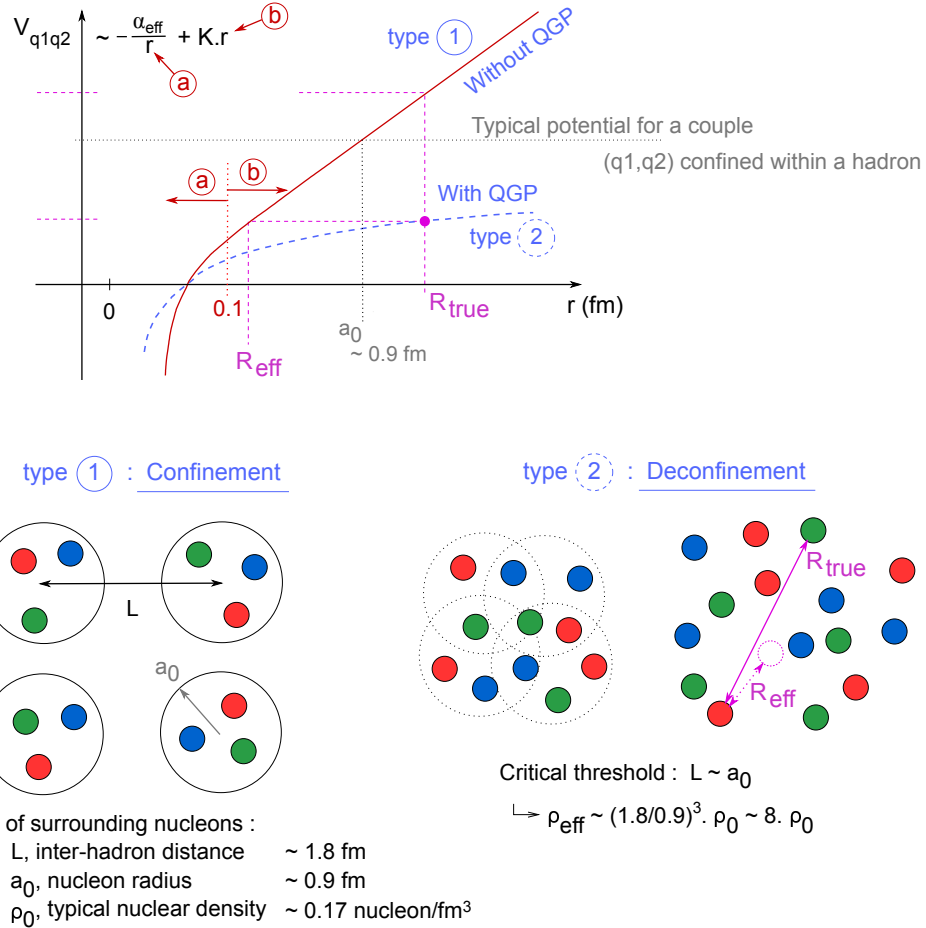


Fig. 2.6: QCD interaction potential between two coloured-objects (quark-quark or quark-antiquark) as a function of their separation r . Figure taken from [63].

gravitational force between two masses exhibit this property; in these cases, the interaction gets weaker as the distance increases between the two objects.

Conversely, the second term takes the upper hand at $r \geq 1\text{fm}$, the force increases linearly with the distance between the two quarks, as if they were connected by an elastic or spring made of gluons. As the quarks are pulled away, the energy stored in the spring of gluons accumulates until it reaches the threshold to create a quark-antiquark pair³³. This description is shown on Fig. 2.7. The spring tying together the initial $q_i \bar{q}_i$ pair ruptures and the accumulated energy is expended on producing a $q_1 \bar{q}_1$ pair: the freshly created quark, q_1 , binds with \bar{q}_i , \bar{q}_1 with q_i . This process continues until all the $q\bar{q}$ pairs have a sufficiently low energy to combine into a hadron. Note that the initial quark-antiquark pair could be replaced by a pair of gluons and the process would still be the same. As a result, any colour-charged particle – quark or gluon – can not be found isolated; they must be confined in a colour-neutral object, such as meson and baryon³⁴. This phenomenon is referred as

³³There is an alternative scenario: the energy stored in the spring of gluons continues to increase until it reaches the threshold to create not one but two quark-antiquark pairs. Obviously, this path – which explains the production of one or several baryons from the vacuum – demands more energy and thus is less probable to occur.

³⁴If there is (ordinarily...) no such thing as free parton, the same would be true for a colour-charged hadron. For this reason, baryons and mesons are colour-neutral structures.

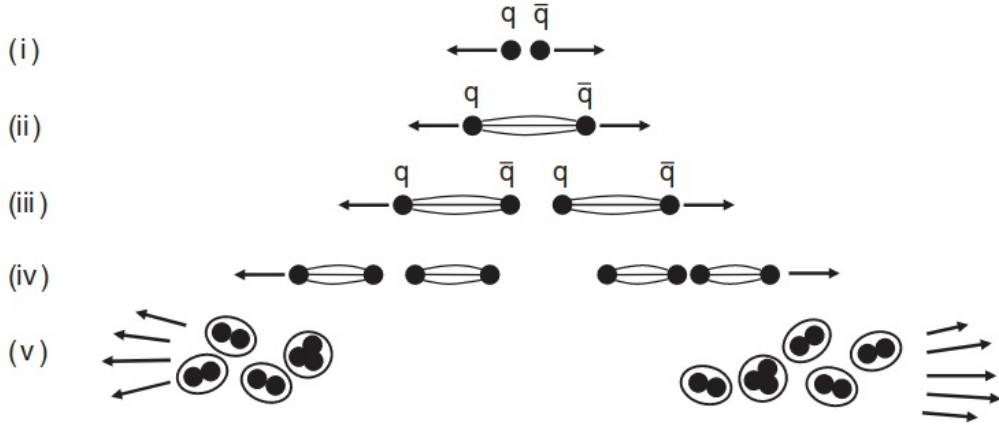


Fig. 2.7: Schematic of the quark confinement: (i) the quark and antiquark are pulled away from each other;(ii) as they separated, the string of force tying together the pair stretches; (iii) the energy stored in the string now exceeds the necessary energy for creating a new quark-antiquark pair, the string will break and the two initial quarks will form smaller strings with the newly created pair;(iv) this process continues;(v) until all the quarks and antiquarks have a sufficiently low energy to form hadrons. Figure taken from [35].

colour confinement.

Interestingly enough, the quark confinement is analogous to the behaviour of a magnet. The latter consists of a north and south poles. If one tries to isolate one of the poles, for example, by cutting the magnet in half, this would only yield into two small magnets. Like the quarks, no one has ever seen an isolated magnetic pole (magnetic monopole).

I-C.ii Chiral symmetry breaking

In Eq. 2.3, the Lagrangian density of QCD was presented and split into four different terms. The quark and gluon kinetic energy and the quark-gluon interaction terms preserve the chiral symmetry, meaning that they leave the chirality of the quarks unchanged. The mass term, though, mixes the left- and right-handed particles:

$$m_q \bar{\psi}_q^i \psi_{qi} = m_q (\bar{\psi}_q^{i,L} \psi_{qi}^R + \bar{\psi}_q^{i,R} \psi_{qi}^L). \quad (2.5)$$

The quark mass, m_q , controls whether the chiral symmetry is broken or preserved. For massless quarks, this term is null hence left- and right-handed particles do not interact together; they would live, somehow, in two separate worlds. Consequently, every hadron would have a twin, identical in every point apart from the handedness: one is left-handed, the other right-handed. In practice, the quarks have a finite mass but, for the light-flavour ones, it is sufficiently small to consider the chiral symmetry as an approximate symmetry. Therefore, chiral partners are expected to have slightly different masses. However, this is clearly not the case of the ρ ($m_\rho = 770\text{MeV}/c^2$) and a_1 ($m_{a_1} = 1260\text{MeV}/c^2$) mesons, meaning that the chiral symmetry is much more broken than expected [25].

To be exact, it is *spontaneously* broken³⁵. This concept is visualised in Fig. 2.9. Returning to the example in the note 19, the continuous transition of the ferromagnet is characterised by an order parameter: the magnetisation. When the temperature is so high that the thermal motions disrupt the alignment of all the magnetic dipoles, the potential is symmetric and the minimum is centred at zero magnetisation (left Fig. 2.9). As the temperature decreases and the magnet cools down, the symmetry of the potential is preserved but there are now two minima. The system (the ball) has to choose one, acquiring a non-zero magnetisation in the process, and hence breaking the symmetry (right Figs. 2.9).

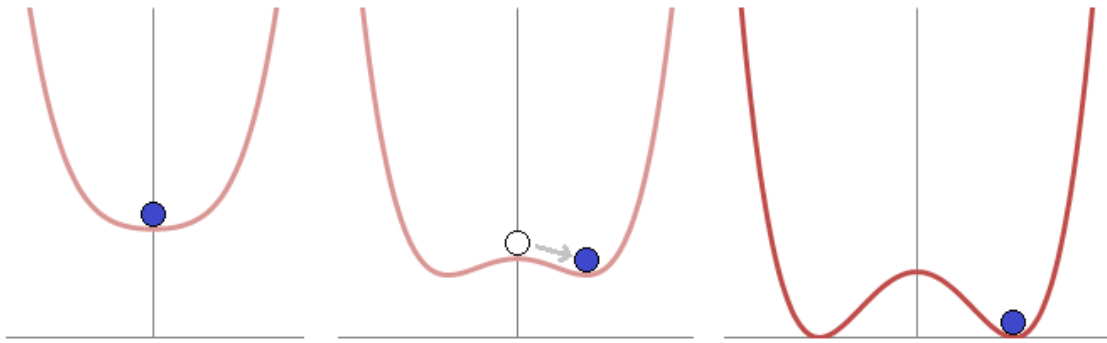


Fig. 2.8: The left figure represents the shape of the potential at high energy, there is one minimum and it is centred on zero. Right figures: as the energy decreases and below a certain critical temperature, the ground state is no longer centred on zero but some distance away from it. Both ground states are equivalent, the system chooses one of them; this is a spontaneous symmetry breaking. The x -axis here represents the order parameter. Figure taken from [66].

The same process occurs for the chiral symmetry but, in this case, the order parameter is the *chiral condensate*. This quantity, $\langle \psi_q \bar{\psi}_q \rangle$ or $\langle q\bar{q} \rangle$, measures the coupling between left- and right-handed particles in vacuum. It was mentioned earlier that, in QFT, the vacuum is not empty but is composed of fleeting particle-antiparticle pairs that pop in and out. It could be that the Lagrangian density of QCD have an approximate chiral symmetry, but the vacuum does not. This means that particles with different handedness in the vacuum may (or not) interact together, depending the vacuum expectation value of the chiral condensate. If the $\langle q\bar{q} \rangle$ is null, the chiral symmetry is restored (left figure 2.9). Conversely, it is spontaneously violated when the chiral condensate is non-zero (right figures 2.9).

This symmetry was extensively studied by Yoichiro Nambu and Giovanni Jona-Lasinio in 1961 [67]. In their model, the chiral condensate emerges from the passage of particles in the vacuum³⁶; for that reason, the chiral symmetry breaking is qualified as *dynamical*. Moreover, as the partons (inside a hadron) travel through the vacuum, they interact with the condensate and acquire an additional mass, the *dynamical mass*³⁷. Predominant fraction of the hadron mass originates from this

³⁵Well, it is also *explicitly* broken but we will pass on that detail.

³⁶In fact, the chiral condensate, and hence the spontaneous chiral symmetry breaking, is a consequence of the colour confinement [26].

³⁷As opposed to the *bare mass* stemming from the Higgs mechanism. It should be mentioned

extra mass: for example, the proton mass sits $\sim 938 \text{ MeV}/c^2$ and the bare mass of its quark constituents represents almost $10 \text{ MeV}/c^2$, that is $\sim 1\%$ of proton mass.

On a side note, lattice QCD calculations predict that the chiral symmetry can be restored by heating or compressing matter. This is clear on Fig. 2.9 where the chiral condensate vanishes as the temperature and/or density increases. In such conditions, the ordinary hadronic matter undergoes a phase transition, in which hadrons are only clothed by the bare mass of its constituents.

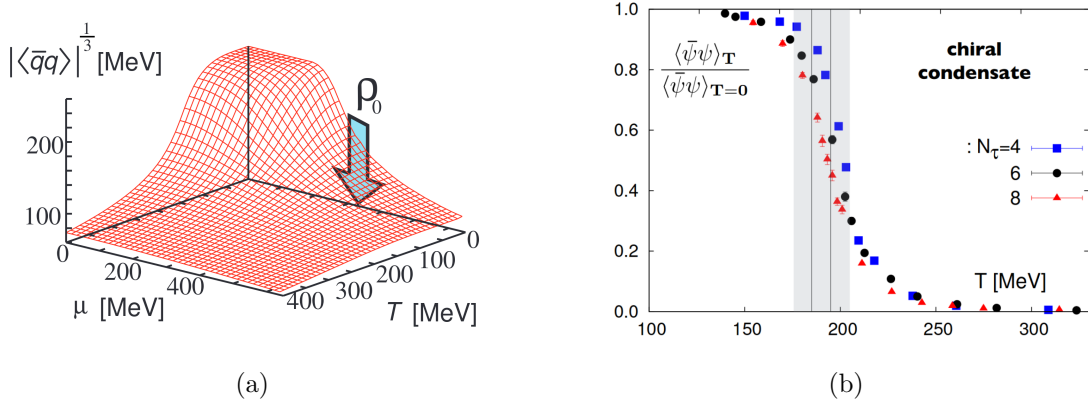


Fig. 2.9: Lattice QCD results on the evolution of the chiral condensate as a function of (a): the matter density (or the baryochemical potential μ) and the temperature (T) [68], (b): the temperature for different lattice points N_τ [69]. The arrow on the left figure indicates the value of μ corresponding the ordinary nuclear density, ρ_0 . The grey bands on the right figure indicate a range for the transition temperature.

I-C.iii The QCD-phase diagram

In addition to the chiral phase transition, another one comes onto stage as the temperature increases. The Fig. 2.10 shows the predicted evolution of the pressure, energy density and entropy density for a hadron gas as a function of the temperature of the medium. The properties of the gas change rapidly when the temperature reaches $T_c = 154 \text{ MeV}$, indicating the liberation of many degrees of freedom. In this case, these are the partons – ordinarily confined within hadrons – that now undergoes a *deconfinement* transition and becomes quasi-free.

I write *quasi-free* because even at $T \sim 400 \text{ MeV}$, the energy density does not reach the ideal gas limit. As a consequence, the quarks and gluons are still interacting but weakly. Due to this shared similarity with the plasmas, this new state of hadronic matter is dubbed *quark-gluon plasma* (QGP). Note that, because the coupling between the partons decreases with the increasing momentum transfer and temperature (asymptotic freedom), the energy density will ultimately overlap with

that nothing prevents the gluons to acquire also a dynamical mass. In this case, there would not be massless anymore.

the ideal gas limit but at much larger temperature though.

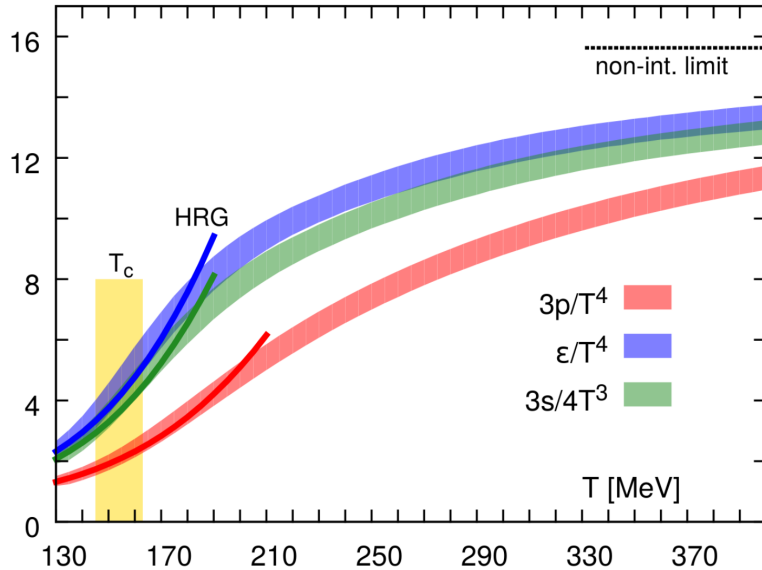


Fig. 2.10: Lattice QCD calculations of the pressure (p), energy density (ϵ) and entropy density (s) normalised to the fourth (third, for the last quantity) power of temperature. The solid lines represent the prediction of the hadron resonance gas (HRG) model, the black dashed line indicates the energy density in the limit of an ideal gas. The transition temperature T_c is equal to 154 ± 9 MeV. It should be emphasised that these predictions have been obtained assuming a zero net baryon density. Figure taken from [70].

The Fig. 2.11 provides the full QCD phase diagram. As it can be seen, there are two general ways to form a quark-gluon plasma: either one increases the temperature, or one increases the net baryonic density by compressing hadronic matter. The above phase transition corresponds to the former: by heating up the system at (almost) zero net baryon density, ordinary nuclear matter transforms first into a hadron gas and then undergoes a phase transition towards a QGP. This is what someone would see if he/she could rewind the videotape of the time-evolution of the Universe, from nowadays to a few μ s after the Big Bang. In the latter, the ordinary nuclear matter at relatively low temperature acquires, by compression, a larger and larger baryon density until the system transforms into a QGP. This state of matter is supposed to be present in the core of neutron stars[71], with potentially a colour superconductor behaviour [72].

There is a profound difference in the nature of the phase transition between the one in the high-temperature region and the other with a high baryon density. Similarly to chiral transition on Fig. 2.9, the Fig. 2.10 shows a smooth evolution from one phase to another, indicating a second order — or at least, a crossover — phase transition [74]. In contrast, the high baryon density driven evolution is expected to be more abrupt, more sharp as when ice melts to turn into water. This corresponds to a first order transition. It follows that there must be a critical point somewhere in the middle of the phase diagram, joining the first and second (or crossover) phase transitions [75]. Its precise location is currently unknown, as no singularities have

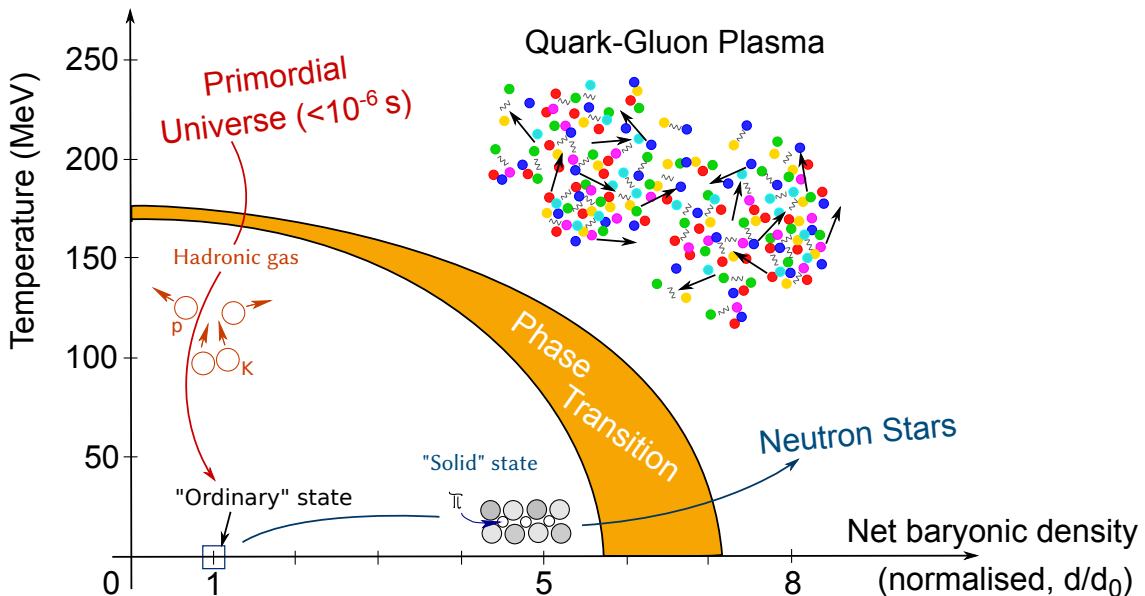


Fig. 2.11: Schematic representation of the QCD phase diagram as a function of the temperature and the net baryonic density. The latter is normalised to the net baryon density of ordinary nuclear matter. Figure taken from [73].

been observed yet.

II The Quark-Gluon Plasma

Each field of research has its pioneers and the study of the quark-gluon plasma is no exception. The first one was arguably Rolf Hagedorn, who approached the particle production making use of statistical physics. This endeavor led ultimately to the invention of the statistical bootstrap model (SBM) in 1964. At that time, a large number of massive resonances were observed, and this model provided a successful production mechanism for these particles³⁸. However, this description was conceived before the development of the quark model. When the quarks were finally considered as the elementary building blocks of hadrons, an extension of SBM was called for [76].

The mutation of the statistical hadronisation model was achieved by the father of SBM and Johann Rafelski, between 1977 and 1980. This process led to a new paradigm. It was realised that, at a certain temperature, hadrons are melting to form a new phase composed of boiling quarks: the quark-gluon plasma. Although this concept was already intuited before by numerous physicists – including Peter Carruthers in 1974 [77] or George F. Chapline and Arthur K. Kerman in 1978 [78] –, it was only approached qualitatively.

³⁸The statistical bootstrap model considers a gas of interacting hadrons, composed of all possible particles and their resonances, in a heat bath. If several light hadrons and/or resonances get compressed into a smaller volume, they could themselves be considered as a highly excited and massive resonance (also called fireball). Thus, the hadron gas rather corresponds to a gas of fireballs, that can also become a fireball in itself if compressed. This description provided an explanation for the mass spectrum of hadronic states.

Nevertheless, Chapline and Kerman were the first ones to make the connection between the QGP and (relativistic) heavy-ion collisions. The same year, this point is addressed quantitatively by Siu A. Chin[79] and later refined in a paper by James D. Bjorken in 1983 [80]. In this renowned publication, Bjorken presents an analytical solution for one-dimensional relativistic hydrodynamics in heavy-ion collisions, as well as the space-time evolution of the QGP at mid-rapidity (*Bjorken scenario*), laying down the foundations for the research programme at CERN.

Starting in 1986, a vast number of heavy ion experiments emerges at the CERN's Super Proton Synchrotron (SPS): WA85, NA36, NA35, Helios-2, NA38, WA80, and their future descendants [81]. At first, ^{16}O and ^{32}S nuclei were accelerated at 200 GeV (per nucleon) until 1995, when the SPS switched to ^{208}Pb beams with an energy per nucleon of 158 GeV. In a press conference held in February 2000, CERN reports to have “compelling evidence that a new state of matter has been created. The new state of matter found in heavy-ion collisions at the SPS features many of the characteristics of the theoretically predicted quark-gluon plasma” [4]. This announcement marks a turning point for QGP research: partonic matter is not a mere theoretical concept anymore; it becomes real, tangible and measurable.

The Relativistic heavy-ion Collider (RHIC) at BNL enters in operation in the next few months, with its four experiments – BRAHMS [6], PHOBOS [7], PHENIX [8], STAR [9] – dedicated to observe and characterise the QGP under different observables. In April 2005, BNL holds a press conference in order to present the results of the RHIC experiments, and by doing so, confirms the existence of "a new type of nuclear matter" [5].

Nowadays, the study of the QGP is mainly centred around two accelerators: the RHIC at BNL and, since 2009, the Large Hadron Collider (LHC) at CERN. Alike RHIC, the latter also has four experiments: ATLAS, CMS, LHCb and ALICE. Although, they all have a heavy-ion research programme, ALICE is specifically designed to analyse the QGP. Concretely, it pursues the exploration of the QCD phase diagram and the characterisation of this new state of matter initiated at the RHIC, but at much higher energies. For comparison, the LHC delivers Pb-Pb collisions at a centre-of-mass energy per nucleon $\sqrt{s_{\text{NN}}} = 2.76$ and 5.02 TeV, and Xe-Xe collisions at $\sqrt{s_{\text{NN}}} = 5.44$ TeV. This is, at least, twenty times more energetic than at the RHIC. The LHC accelerator, as well as the ALICE collaboration, are presented in the next chapter, chap. 3.

II-A The time evolution of a heavy-ion collision

We timidly started above to raise the question of how a heavy-ion collision leads to the formation of the QGP? This point was addressed by Bjorken in his scenario of the same name. Although the current description turns out to be more complex than anticipated, the Bjorken scenario still provides the key steps of the QGP formation process. The following discussion is structured around the Figs. 2.12 and 2.13

A facility, such as the LHC or RHIC, accelerates heavy nuclei to ultra-relativistic speed. At the LHC energies, the Pb nuclei in each beam are accelerated to, at least,

1.38 TeV³⁹, which corresponds to a Lorentz factor γ of about 1500. Consequently, as Bjorken argued [80], even though the partons involved in the collision carry a tiny fraction of the incident beam energy, the nuclei are so extremely boosted that the space-time evolution of the system should be the same in all centre-of-mass frames near central rapidity, and thereby the particle yield should be flat as a function of rapidity, defining a central plateau structure for particle production. Moreover, at such energies, the nuclei are not stopped but rather continue to recede in opposite direction with respect to the collision point; this is the *Bjorken regime* or *transparency regime* and corresponds to net baryonic density close to zero⁴⁰. Another implication is that, because of the length contraction, the nucleus looks like a highly-contracted pancake at mid-rapidity, as can be seen on Fig. 2.12.

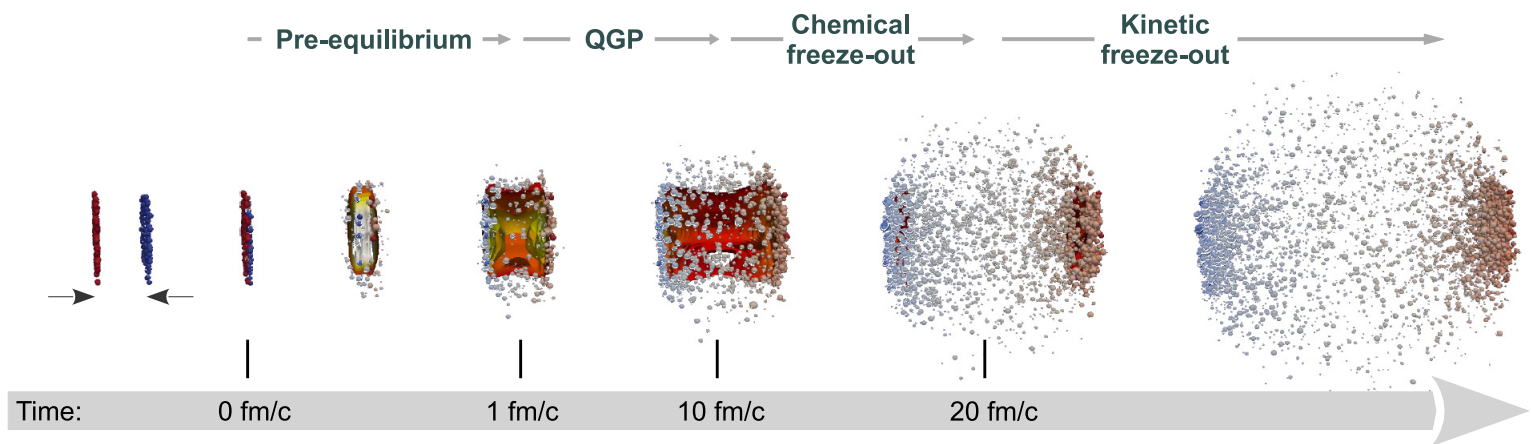


Fig. 2.12: Simulation of the time evolution of a heavy-ion collision, rendered in seven pictures. Figure originally created by Hannah Petersen, taken from [82] and modified by the present author.

The two extremely boosted nuclei approach each other and collide head-on⁴¹. At the same time, the clock associated to the centre-of-mass frame starts to run and indicates 0 fm/c.

The partons of each nuclei start interacting via either hard-processes – that involve large momentum transfers and lead to the creation of high momentum partons or massive quarks such as the charm, bottom or even top quarks – or soft-processes,

³⁹The least energetic Pb-Pb collision available at the LHC being $\sqrt{s_{\text{NN}}} = 2.76$ TeV, each beam carries 1.38 TeV per nucleon.

⁴⁰As opposed to the *Landau regime* or *stopping regime*, where the nuclei are completely stopped in frontal collisions. It occurs only for collisions at centre-of-mass energies up to a dozen of GeV per nucleon pair. These two regimes actually relates to the two different QGP phase transition: either by heating the system (Bjorken scenario) or compressing it (Landau scenario).

⁴¹Note that this is not necessarily the case, the two nuclei can be slightly shifted. The *impact parameter* quantifies the offset usually in fm, or alternatively in percentage. In the latter case, we talk about *centrality*. Both parameters are accessible by making use of a *Glauber model*, that provides a semi-classical picture of a nucleus-nucleus collision as a function of the average number of nucleons and nucleon participants in the collision.

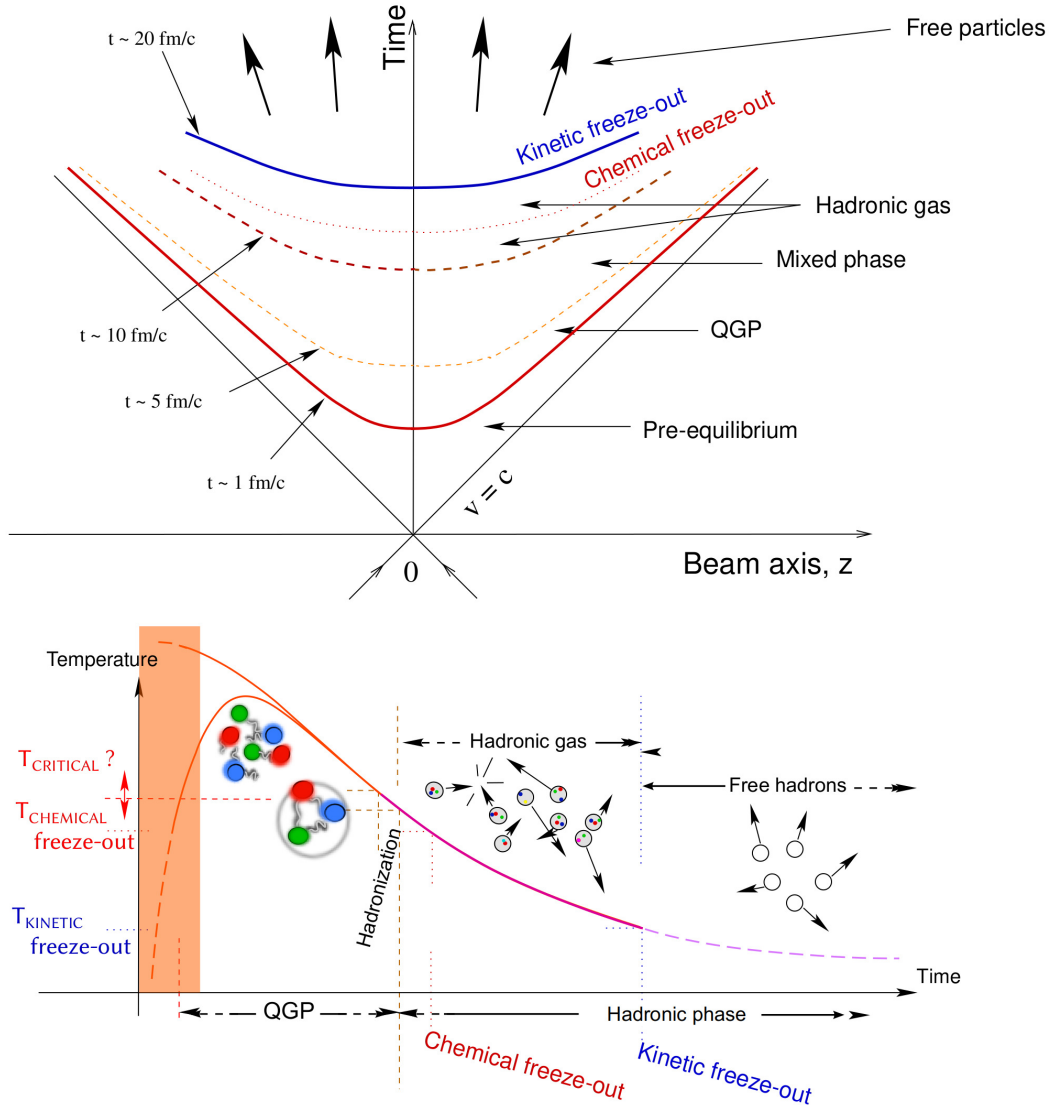


Fig. 2.13: The two views of the Bjorken scenario for ultra-relativistic heavy-ion collisions. Top panel: space-time evolution. Bottom panel: temperature-time evolution. Figure taken from [83].

characterised by small momentum transfer and representing most of the interactions in the initial stage of the collision. As the number of parton-parton interaction increases, the energy density of the system builds up enabling the creation of quarks and gluons out of the vacuum. Rapidly, a dense region of matter (dubbed "fireball") is formed, where partons are strongly coupled but not yet thermalised. This is the pre-equilibrium phase.

Here, the emphasis is on coloured particles, but other kind particles can be produced in the fireball, namely the leptons and photons. Because i) they carry no colour charge and ii) the typical interaction time of the weak ($\approx 10^{-10} \text{ sec}$) and electromagnetic forces ($\approx 10^{-16} \text{ sec}$) is too short compared to the timescale of a heavy-ion collision ($\approx 10^{-23} \text{ sec}$), they will simply escape the medium unaffected.

If the energy density is high enough (typically around 1 GeV/fm^3), the initially produced matter undergoes, first, a phase transition towards the restoration of the

chiral symmetry and, if possible, then towards the QGP. Due to multiple interaction between the medium constituents, the energy gets distributed evenly among them leading the system to a thermal equilibrium around $1 \text{ fm}/c$ ($\approx 10^{-23} \text{ sec}$) after the collision⁴².

Once the QGP is formed, it experiences two expansions. Driven by the non-uniform geometrical energy distribution in the initial stage of the collision, a pressure gradient appears in the QGP, which results in a radial expansion of the system. Furthermore, the boost of the two incident nuclei causes the plasma of quarks and gluons to inflate in the longitudinal directions. Since the energy deposited initially in the system is fixed and its spatial size keeps extending, the energy density decreases and inevitably, the fireball cools down.

At some point, most of the parts of the system goes below the critical temperature, the deconfined partons start to recombine into hadrons. The QGP evaporates into a gas of hadrons. Note, that because the chiral transition – in this case, from a restored symmetry to a broken one – occurs below T_c , the mesons and baryons formed during this hadronisation process only carry the bare mass of their constituents. At least, until the system further cools down and undergoes a phase transition towards a breaking of the chiral symmetry, as explained in the Sec. I-C.ii.

The energy density within the hadron gas remains significant, sufficiently to allow for inelastic collisions. Consequently, the chemical composition in terms of particle species is in constant evolution. Around $10 \text{ fm}/c$, as the energy density decreases, inelastic interactions become less and less frequent. They become impossible when the gas reaches the *chemical freeze-out* temperature. The particle composition is now fixed but hadrons can still interact elastically.

Although, the hadron content should be fixed, some resonances can still regenerate via pseudo-elastic scattering. This is, for example, the case of the K^{*0} that can be recreated through π^\pm - K^\mp interaction. On the other hand, elastic scatterings modify the momentum of one of its decay products. In such a case, the measured yield would decrease.

At $20 \text{ fm}/c$, the hadron gas fades into free hadrons. The momenta of the hadrons are now fixed. This is the *kinetic freeze-out*. These particles will fly towards the detectors and, for some of them, decay via weak or electromagnetic interactions. Either the particles originate directly from the collision or are decay products, once they have reached the detector, they will be detected and reconstructed, giving rise to an event such as the one displayed in the Fig. 2.14.

In total, the QGP only exists for about 10^{-22} sec , which is currently impossible to reach for the most advanced readout electronics. The study of this state of matter relies on the signatures that are printed in the detectors after the collision. Theoretical models provide predictions of what the QGP footprints look like. Nowadays, it is widely admitted that the following signatures are marks of the QGP.

- **Collective flow:** The QGP being an almost perfect liquid of constituents with small mean free path, the pressure gradient created by the collision leads

⁴²Note that this is not a mandatory step for the QGP formation.

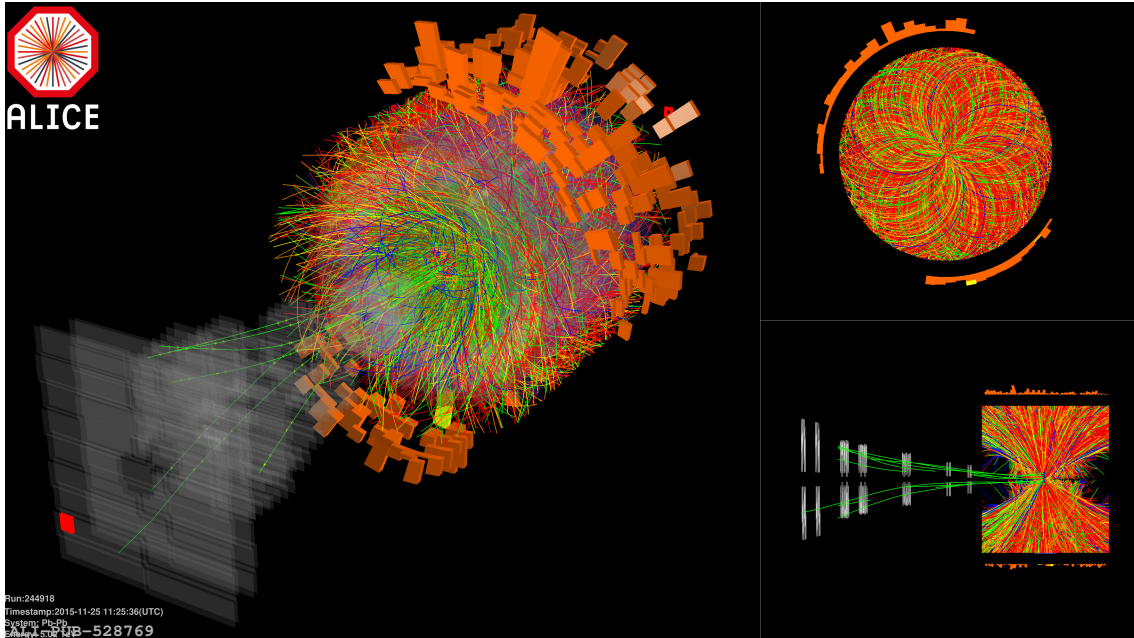


Fig. 2.14: Event display of the particles reconstructed with the ALICE detector and created in a Pb-Pb collision at $\sqrt{s_{\text{NN}}} = 5.02$ TeV in 2015. Figure taken from [84].

to a collective flow, *i.e.* flow of partons, that can be described in the final state by ultra-relativistic hydrodynamic models. This aspect is addressed, in particular, by performing measurements sensitive to the radial/isotropic and anisotropic flow. The former is characterised by a boost of the low- p_{T} produced hadrons to higher p_{T} —the higher the mass, the higher the boost—; the latter is studied through a Fourier series decomposition of the azimuthal distribution of the emitted particle density. Moreover, the collective motion of partons can also be observed looking at long-range particle correlation.

- **Direct photons:** Photo-production occurs over the entire duration of the collisions, but it is strongly increased when the system is hot. Therefore, a significant excess of *direct*⁴³ photons is observed in heavy-ion collisions, suggesting that a QGP has been formed there. Moreover, since they leave the medium unaffected, they carry informations on its properties. In particular, the low- p_{T} photons are essentially produced out of the plasma heat, hence they are designated as *thermal photons*. Accounting for the blue-shift induced by radial expansion of the system (Doppler effect), the measurement of their yield provides an effective temperature of 304 ± 41 MeV in the most central Pb-Pb collisions [84].
- **Jet quenching:** The high- p_{T} or massive partons are produced in the early stage of the collision. As they interact with other soft partons of the QGP, a part of their energy is transferred to the medium, resulting in energy loss

⁴³The term *direct* aims at designating only the photons originating from the different stage of the collisions (prompt), and not the ones from hadronic decays (non-prompt).

effects. They are of two kinds: collisional, which consists in elastic scattering *with* the medium constituents, and radiative that corresponds to an inelastic interaction and results in the emissions of gluons *within* the QGP. In the case of two jets, back-to-back, created close to the phase boundary, one will escape the fireball whereas the other will lose most of its energy in the medium. Thus, if one of the back-to-back jets is missing in the event, this would suggest the existence of a hot and dense medium, as observed in [85]

- **Heavy quarkonia suppression:** The heavy quarks, such as charm or beauty, can fragment and hadronise to form a quarkonia ($c\bar{c}$ or $b\bar{b}$ mesons). Because of the low binding energy of these states, they will start to melt and dissolve within the medium. On the other hand, this suppression can be counterbalanced by a regeneration of the quarkonia state: at the chemical freeze-out, it is possible for a heavy quark to recombine with a heavy anti-quark. Therefore, the quarkonia production is compared to theoretical models, and so far, the results are consistent with the formation of a QGP.
- **Hadron abundancy:** At chemical freeze-out, the hadron gas is supposed to be in thermal and chemical equilibrium. The hadron composition in the hadron can therefore be addressed in a statistical approach using the grand canonical formalism. The *statistical hadronisation model* (SHM) provides a prediction of the mesons and baryons abundancies, as a function of the gas volume and temperature, and the different chemical potentials (μ_B for the baryonic one, μ_S for the strangeness one,...). By fitting the measured yields of various hadron species with the SHM prediction, the chemical freeze-out temperature T_{ch} and volume V_{ch} can be estimated. The values $T_{ch} = 155 \pm 2$ MeV and $V_{ch} = 5924 \pm 543$ fm³ are consistent with lattice QCD calculations.

About abundance, the one of strange particles stands out of the other species. It is, in fact, one of the historical key signatures of the QGP and is called the *strangeness enhancement*.

II-B Strangeness enhancement

The concept of strangeness enhancement, that consists in the abundant production of strange hadrons in heavy-ion collisions, starts to take shape in the mind of Johann Rafelski in 1980. The original argument is based on the assumption that, in a melted vacuum such as the one that settles in the QGP pre-equilibrium stage, the chiral symmetry restoration results in strange quarks carrying only their bare mass (m_s), that is at least two times lower than QGP temperature ($2m_s < T_{QGP}$). Thus, this opens the way to a chemical equilibration/saturation of strangeness. When the fireball cools down, the numerous s and \bar{s} tend to hadronise into strange baryons (qqs or $\bar{q}\bar{q}s$,...) rather than mesons ($\bar{q}s$ or $q\bar{s}$).

Back then, gluons were still hypothetical objects. Strangeness production was mainly considered in the annihilation process of light quark pairs $q\bar{q} \rightarrow s\bar{s}$ (Fig. 2.16d).

In 1981, József Zimányi and Tamás Bíró estimated that, with this process, the chemical equilibrium of strangeness takes too much time to settle and is reached around eight times the natural lifespan of a QGP fireball. However, Zimányi and Bíró assumed that there were no gluons and were focused on the physical case of a hadron gas [86].

In parallel, it was realised that gluon fusion processes dominates the production rates. Together with Berndt Müller, Rafelski shows in 1982 that the chemical equilibration of strangeness is possible within the QGP lifespan thanks to the fusion of gluons created out of the vacuum heat [87]. The different $gg \rightarrow s\bar{s}$ processes are depicted in Fig. 2.16a,b,c.

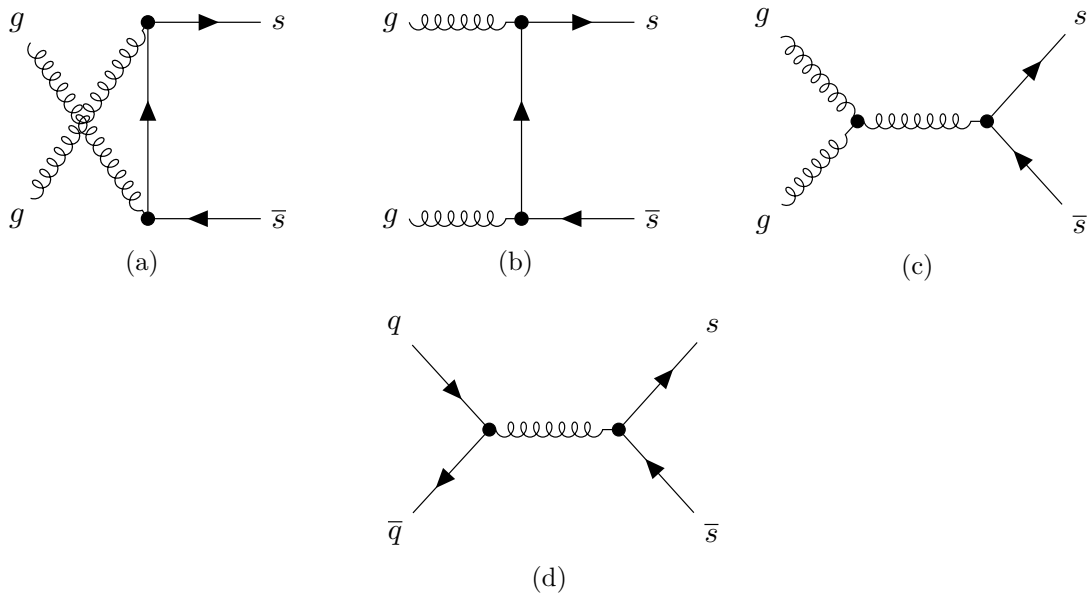


Fig. 2.15: The lowest-order QCD diagrams for $s\bar{s}$ production. (a)(b)(c) the different gluon fusion processes $gg \rightarrow s\bar{s}$; (d) quark-antiquark annihilation process $q\bar{q} \rightarrow s\bar{s}$. Figure taken from [63].

In summary, the strangeness enhancement was proposed by Rafelski and Müller in 1982 as a signature of a deconfined quark-gluon matter. They demonstrated that:

- the QGP begins to be saturated by strange quarks and anti-quarks when the temperature of the plasma reaches the 200 MeV after about 2×10^{-23} sec,
- this saturation is possible because strange quarks can pop in out of the QGP heat ($2m_s < T$) via gluon fusion processes (Fig. 2.15). These processes are favoured because i) they are more energy/time efficient and ii) the high density of gluons created out of the vacuum,
- at the hadronisation, the strangeness tends to be distributed on baryons rather than mesons. Consequently, this leads to an increased production of strange particles in the final state of the collision. In fact, the larger the strangeness content, the larger the enhancement of the hadron production.

Experimentally, the strangeness enhancement manifests itself through an increase of the *relative* yields of strange hadrons in heavy-ion collisions. Now comes two difficulties: so far, only the strangeness enhancement from the formation of a QGP was considered, however a similar phenomenon could occur in a hadron gas⁴⁴. The difference between these two increases in strange particle abundancies resides in the hierarchy between hadrons with different strangeness content [63]:

$$\Omega(sss) / \Xi(dss)_{\text{QGP}} \approx \Xi(dss) / \Lambda(uds)_{\text{QGP}} \quad (2.6)$$

$$\Omega(sss) / \Xi(dss)_{\text{Hadron Gas}} \ll \Xi(dss) / \Lambda(uds)_{\text{Hadron Gas}} \quad (2.7)$$

$$\Omega(sss) / \Xi(dss)_{\text{QGP}} > \Omega(sss) / \Xi(dss)_{\text{Hadron Gas}} \quad (2.8)$$

$$\Xi(dss) / \Lambda(uds)_{\text{QGP}} > \Xi(dss) / \Lambda(uds)_{\text{Hadron Gas}} \quad (2.9)$$

Another issue arises from the definition of *relative* yields. In other words, this comes down to asking what normalisation to use? There are different possibilities, depending on the physics target. Most of the time, the yields of strange hadrons in heavy-ion collisions are compared to the ones in pp collisions. This is relevant in order to discriminate the strangeness enhancement originating from the QGP (heavy-ion collisions) from the one occurring in a hadron gas (as in pp collisions, assuming that there are enough interactions between the different produced hadrons). Alternatively, one could also look at the "continuous" evolution of the yields as a function of the collision system. In such a case, the relative yields correspond to the ratio of production rate between the particle of interest and the lightest known hadron, namely the π . Finally, the focus can also be on the difference of yields between hadrons with the same strangeness content but different mass, typically the yields ratio between a resonant and a non-resonant hadronic state. This could provide some information on the influence of the hadronic phase.

The Fig. 2.16 presents, on the left, the measurement of relative yields of strange hadrons with respect to the pions as a function of the average charged multiplicity of the collision, and on the right, the yield ratios between resonant and non-resonant states are displayed. The lowest multiplicities correspond to pp collisions, and as it increases, we move on towards more and more central heavy-ion collisions.

The left panel of Fig. 2.16 shows that the yield of strange hadrons increases in Pb-Pb and Xe-Xe collisions with respect to pp and p-Pb collisions, and the enhancement factor gets bigger with the strangeness content. This is compatible with the strangeness enhancement picture and confirms the existence of a deconfined quark-gluon matter. Notice that the ratios do not change with the centre-of-mass energy, suggesting that the initial stage of the collision does not play an important role in the strangeness enhancement (at least, at the LHC energies).

On the right panel, the yield ratios between resonant and non-resonant hadronic states seem to decrease when going from elementary collision systems (pp and p-Pb) to the heavy-ion ones. This trend indicates that the temperature of the hadron

⁴⁴Strange hadrons could be formed via inelastic collisions between light mesons and baryons. Because of the large dynamical mass of hadrons, the production of strange particles should be suppressed. This reduction gets more pronounced as the hadron mass is high.

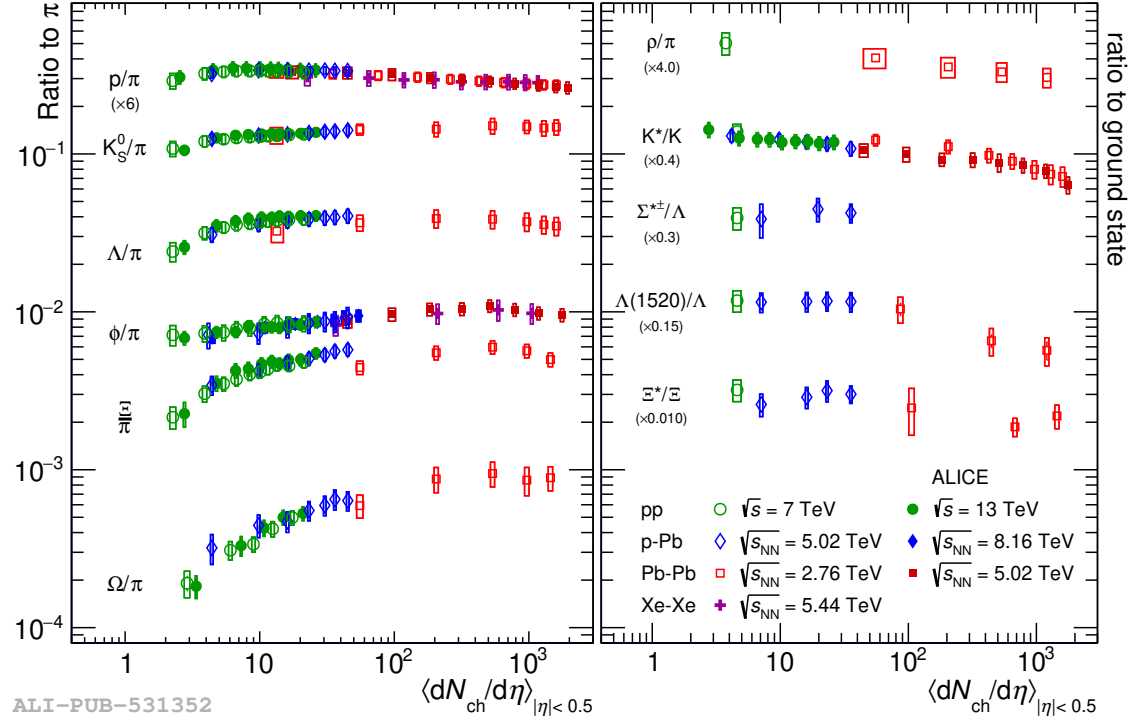


Fig. 2.16: (Left panel) Relative yields of strange hadrons with respect to the pions and (right panel) yield ratios between resonant and ground state hadrons as a function of the average charged particle multiplicities at midrapidity. Results from different collision systems are presented: pp at $\sqrt{s} = 7$ and 13 TeV; p-Pb at $\sqrt{s_{NN}} = 5.02$ and 8.16 TeV; Pb-Pb at $\sqrt{s_{NN}} = 2.76$ and 5.02 TeV; Xe-Xe at $\sqrt{s_{NN}} = 5.44$ TeV. The left panel considers the following strange hadrons: K_S^0 ($\bar{d}s$), Λ (uds), ϕ ($s\bar{s}$), Ξ (dss) and Ω (sss). The error bars corresponds to the statistical uncertainty, whereas the boxes show the total systematic uncertainty. Figure taken from [84].

gas after the QGP is sufficiently high to suppress the resonance yields by elastic rescattering of the decay products.

II-C Comparison with elementary systems

Throughout this section, it was suggested that the formation of the QGP is exclusive to heavy-ion collisions, and it is not expected in more elementary systems – such as pp and p-Pb collisions – because the size of the colliding system is *a priori* too small. Looking more attentively at the Fig. 2.16, one notices that relative yields of strange hadrons increases smoothly from low to high multiplicity pp and p-Pb collisions. In other words, this means that strangeness enhancement seems to be present as well in small systems.

In fact, the aforementioned QGP manifestations, the heavy quarkonia suppression [88], the strangeness enhancement [84], the collective flow [14] have been observed in both heavy-ion collisions and small systems, suggesting the presence of a common collective behaviour. Some signatures are missing though; for example, there are so far no indication of jet quenching nor thermal photons in small systems.

As a consequence, the classical picture of a heavy-ion collision, forming a hot

and dense matter where quarks and gluons are deconfined, needs to be revised. At least, the elementary colliding systems can no longer be considered as a valid reference point, for sufficiently high energies such as the LHC ones. This point will be further addressed in more details in Chap. 6.

Chapter

3 | ALICE: A Large Ion Collider Experiment

As it was already mentionned before, ALICE (*A Large Ion Collider Experiment*) aims at studying QCD bulk matter and, in particular, the quark-gluon plasma (QGP). It is situated in the CERN area, in the vicinity of Geneva, on the ring of the LHC (*Large Hadron Collider*). Being the spearhead of the QGP studies at CERN, it has been designed in order to access to a large variety of observables over a wide range of transverse momentum, thus offering the ability to study the evolution the heavy-ion collision from its initial stages to the hadronic phase.

The first section, Sec. I provides a brief introduction of the immediate surroundings of the ALICE collaboration, the CERN. Different aspects are mentioned, from the organisation to the main experiments on the LHC rings, through the CERN accelerator complex. This brings to the description of the ALICE in Sec. II, from the viewpoint of the collaboration and the experiment via the detector. The latter point allows to exhibit the strength of the ALICE detector, as well as presenting the event reconstruction procedure and the offline framework.

I The CERN

I-A The organisation

Located the border between France and Switzerland, the CERN is like a tiny country with its own culture, its own language (essentially composed of acronyms). It is mostly known for its expertise on particle accelerators and detectors for high energy physics, but it is also the birthplace of some of our everyday devices – such as the World Wide Web (1990), the touchscreen (1972) – or less daily tools, like the Worldwide LHC computing grid (2005) and the multi-wire proportionnal chamber



Fig. 3.1: Aerial view of the CERN accelerator complex (highlighted by the white curves), with an insert on the main site in Meyrin (Switzerland, canton of Geneva). Figure taken from [89] and modified by the present author.

(1968). The Fig. 3.1 provides an aerial view of the CERN sites, with an insert on its headquarters in Meyrin (Switzerland, canton of Geneva). A location that has been decided from the very beginning of the organisation, back in the 1950s.

At the end of the Second World War, Europe lays in ruins, most of the research facilities are destroyed and many physicists have left the continent to work on the other side of the Atlantic. Europe is no longer at the forefront of scientific progress. A situation from which the old continent might never recover, as the European nations do not have the resources to rebuild the basic infrastructure. Nevertheless, things begin to change in 1949 when, at the European Cultural Conference, Louis de Broglie – supported by Raoul Dautry, Pierre Auger, Lew Kowarsky, Edoardo Amaldi and Niels Bohr – proposes to create an European laboratory in order to promote collaboration between Europe’s nations, and share the costs.

The project gains momentum such that, in late 1951, the United Nations Educational, Scientific and Cultural Organization (UNESCO) – pushed by the United States – organises a dedicated meeting on that matter. Some countries show their skepticism: even though the infrastructure costs are mutualised, this kind of endeavor still demands an initial investment; a few years after the end of the war, many countries are still in a difficult financial position and are thus reluctant to participate. After two months of debate, the first resolution of the convention establishing the European Council for Nuclear Research (“Conseil Européen pour la

Recherche Nucléaire” in French or CERN) is ratified in 1952 by the twelve founding member states: Belgium, Denmark, France, Germany, Greece, Italy, Netherlands, Norway, Sweden, Switzerland, United-Kingdom and Yugoslavia [90].

Later that year, Geneva was chosen to host the laboratory. In 1953 the CERN convention is completed and signed by all the members. It defines, amongst others, the membership, the financial contributions, the decision protocols, its denomination¹ and its missions. In particular, the CERN aims not only for technological developments and scientific researches on high-energy physics but also for the “promotion of contacts between, and the interchange of, scientists, the dissemination of information [...]”, and “collaborating with and advising other research institutions” [91].

Nowadays, the organisation includes 23 Member States and ten Associate Member States. There are also non-members States or institution with an Observer status, such as the United-States, Japan, European Union, UNESCO and previously the Russian Federation. In 2017, the CERN counted more than 17 500 people, all over the world, working together towards a common goal, including more than 12 200 scientists [92]. This makes it the largest scientific organisation in the World.

I-B The accelerator complex

As stated in the Article II of the Convention, the construction and operation of particle accelerators stand as one of the CERN’s purposes. In particular, the organisation must immediately develop a 600 MeV synchro-cyclotron and a 28 GeV proton synchrotron (PS). The former, built in 1957, corresponds to the first accelerator of CERN; the latter starts accelerating protons in 1959.

The next step up in beam energies arrives in 1976 with the first underground accelerator, the Super Proton Synchrotron (SPS). It consists in two rings, of seven kilometers circumference each, delivering beams of 300 GeV of protons and antiprotons. At least, on the paper because it is one of the rare cases in particle physics, when the final product performs better than expected in the technical design reports. Thanks to technological advances during its construction, the SPS could reach beam energies up to 400 GeV, and gradually of 450 GeV after some upgrades.

In 1989, a 27-kilometre circular accelerator enters in operation, namely the Large Electron-Positron (LEP) collider. It was tuned such that the colliding energy sits on the resonance mass peak of the Z^0 and W^\pm bosons, but in the search of the Higgs boson, it was also operated with a centre-of-mass energy of 209 GeV on its last year, in 2000. This was – and still is – the largest electron-positron collider ever built.

As one World record calls for another, the LEP collider is decommissioned in order to be replaced in 2008² by the Large Hadron Collider (LHC), the World’s largest and most energetic particle collider. The accelerator is currently operational

¹The CERN Convention was the opportunity to rename the CERN as the “Organisation Européenne pour la Recherche Nucléaire” (or European Organisation for Nuclear Research in English), that would corresponds to the acronym OERN now. Because the initial abbreviation turns out to be more elegant, the name CERN remained.

²Technically, because of an incident on one of the dipole magnets, the accelerator undergoes

	pp	Pb-Pb	Xe-Xe
Energy per beam	6.5 TeV	2.56 TeV	2.72 TeV
Luminosity ($cm^{-2}s^{-1}$)	2.1×10^{34}	6.1×10^{27}	0.4×10^{27}
Velocity (in units of c)	0.99999998	0.99715693	0.99898973
Circumference	26 659 m		
Beam vacuum		10^{-13} atm	
Number of RF cavities		8 per beam	
Number of magnets		9593	
Number of dipole magnets		1232	
Dipole operating temperature		1.9 K (-271.3 C)	
Current flowing in the dipole		11 850 A	
Magnetic field of the dipole		8.33 T	

Table 3.1: A selection of design parameters for the LHC during the Run-2. Values taken from [95] and [42].

and should still be, at least, until 2038. Beyond this date, the CERN might start the construction of the Future Circular Collider, a particle accelerator with a circumference of 100 km[93][94].

The LHC is the collider of (almost) all superlatives. To put it into perspectives, the Tab. 3.1 lists some of its important characteristics.

As in any accelerator, particles circulate in a vacuum tube in order to avoid collisions with gas molecules. The beam is subject to ultra-high vacuum, corresponding to a pressure of 10^{-13} atm, applied over the approximately $9\,000\,m^3$ covered by the LHC. In comparison, this is like pumping down the nave of a cathedral to a pressure level similar to the one at the Moon's surface.

Various magnets control the particle trajectory: 1232 dipoles to bend the 6.5 TeV beams, 392 quadrupoles to squeeze and focus the beam down to the collision point, etc. If we hope to curve the particle's trajectory at the LHC energies, the dipoles must create an intense magnetic field of 8.33 T, demanding a current of 11 850 A. For comparison: at ambient temperature, the dissipated heat would melt down the magnet. Hence, 90 tonnes of superfluid helium are injected into the magnets bringing their temperature down to 1.9 K (-271.3 C), that is even lower than the temperature of outer space (2.7 K). At this level, the dipoles become superconducting and can now endure the flow of currents to develop the necessary magnetic field.

The particle acceleration is ensured by eight radiofrequency cavities (RF cavities)³ per beam. Most often, they accelerate protons at 6.5 TeV, which corresponds to the typical kinetic energy of flying mosquito but distributed on the minuscule volume of a proton. At such energy, a proton travels at almost light-speed and makes 11 245 LHC turns per second. Furthermore, because of the RF cavities, each

some repairs that delay its operation by fourteen months.

³It consists in a cavity filled with an electromagnetic field oscillating at a specific frequency (in the radio wave's domain, hence the name of the radiofrequency cavities), and shaped in such a way that resonance occurs.

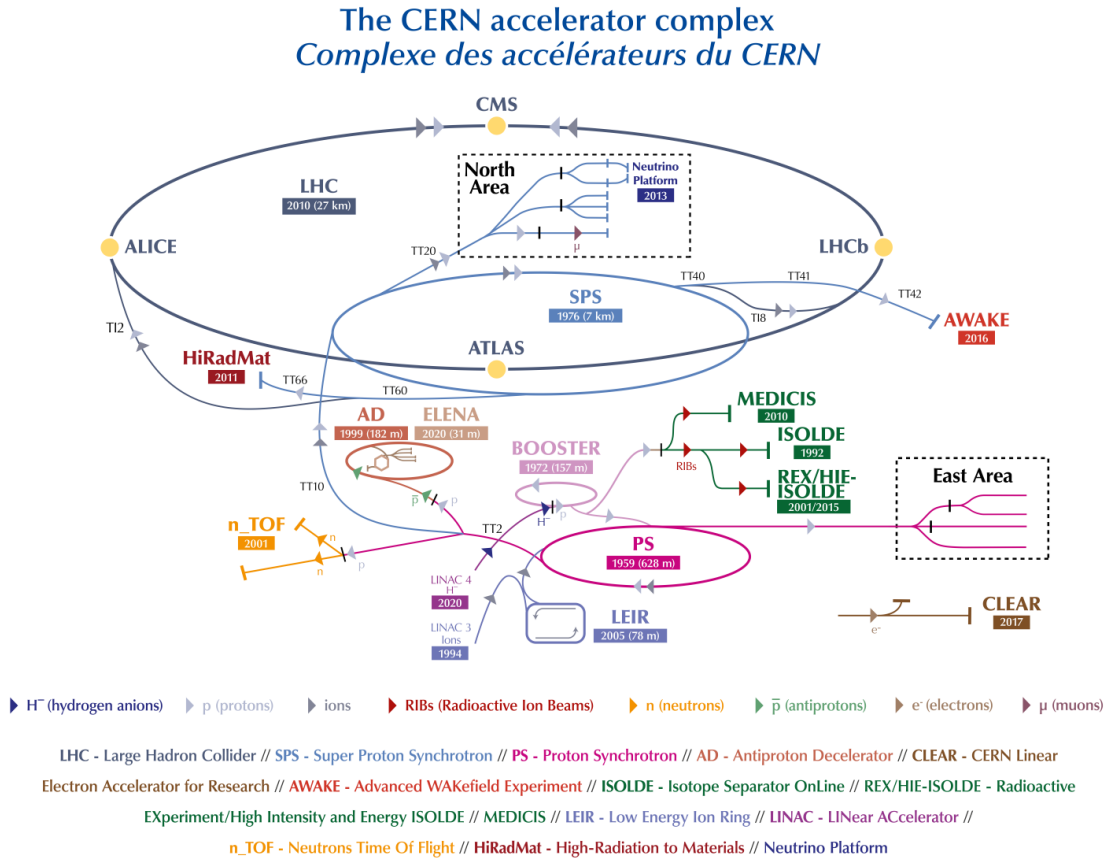


Fig. 3.2: Schematic representation of the CERN accelerator complex as in 2023. Figure taken from [96].

beam is divided into 2808 bunches separated by 7.5 m (or 25 ns⁴) and containing about 10^{11} protons.

It is noteworthy that the LHC is only the last element of the acceleration chain, as represented in the Fig. 3.2. The beam energy increases gradually using the past CERN’s accelerators. Depending on the type of beams (pp or AA), the route to the LHC differs slightly. For a proton beam, negatively charged hydrogen ions are first accelerated by the Linear Accelerator 4 (LINAC 4)⁵ to 160 MeV, and then they are injected in the Proton Synchrotron Booster (BOOSTER) in order to reach an energy of 2 GeV. The electrons of the hydrogen ions are removed when leaving the LINAC 4. For a heavy-ion collision, the Linear Accelerator 3 (LINAC 3) provides a beam of heavy-ions – already stripped of their electrons – to the Low Energy Ion Ring (LEIR), which accelerates them to 72 MeV per nucleon. Whether it is a beam made of protons or heavy-ions, they are successively accelerated by the PS and SPS up to 450 GeV (or 177 GeV per nucleon for heavy-ions). The particles are finally injected

⁴This is the case for the LHC Run-2, but in the Run-1, the distance between two bunches was twice as big, that is 50 ns.

⁵Until 2020, the first acceleration stage was performed by the LINAC 2 that accelerated hydrogen atoms.

in the rings of the LHC in order to reach their top energy of 6.5 TeV (or 2.56 TeV per nucleon for Pb beams) and collide in the four collision points where sits the four main LHC's experiments: ATLAS, CMS, LHCb, and ALICE[97]. Tab. 3.2 presents a few of their characteristics.

Experiment	ATLAS	CMS	ALICE	LHCb
Participants	5 991	5 824	2 085	1 585 
Height (m)	25	15	16	10
Length (m)	46	21	26	21
Width (m)	25	15	16	13
Weight (tonnes)	7 000	14 000	10 000	5 600

Table 3.2: A few characteristics of the four main LHC experiments, namely ATLAS, CMS, ALICE and LHCb. The participants include particle physicists, engineers, technicians and students; their number corresponds to the one as of March 2023[98]. The dimensions of each detector originate from [99][100][101][102].

A Toroidal LHC Apparatus (ATLAS) and a Compact Muon Solenoid (CMS) are the most colossal experiments at the LHC, as much in terms of the number of participants as in the dimension of their detectors. Both cover a wide range of physics and share the same goals, namely characterising the elementary particles of Standard Model – in particular, the Higgs boson – and searching for the new particles beyond the Standard Model, such as dark matter candidates or supersymmetric particles.

ALICE and LHCb (Large Hadron Collider beauty) are more specialised. ALICE aims at studying QCD matter, and particularly under extreme energy densities where a phase of deconfined quark-gluon matter forms, the QGP. On the other hand, LHCb focuses on heavy flavour physics. It is concerned about new physics in CP violation and rare decays, primarily of beauty but also charm hadrons.

In order to carry out their physics programme, the LHC must provide different types of beam. For instance, ATLAS and CMS are essentially interested in pp collisions with the highest interaction rate possible, whereas ALICE needs heavy-ion runs to study *directly*⁶ the QGP. Therefore, the Run Coordination of each experiment gathers regularly with LHC Programme Coordination to discuss and negotiate the accelerator schedule, in order to define a programme which best meets everyone's needs.

I-C The accelerator programme

As shown in the Tab. 3.3, the LHC delivers his first collisions on the 23rd of November 2009; these are pp collisions at $\sqrt{s} = 900$ GeV. The centre-of-mass energy

⁶As discussed in Sec. II-C, the QGP can also be investigated via the study of its signatures in pp collisions.

LHC Run	Year	Collision	Centre-of-mass energy (per nucleon)	Dates
Run 1	2009	pp	900 GeV	23 rd Nov. to 14 th Dec.
		pp	2.36 TeV	14 th and 16 th Dec.
	2010	pp	7 TeV	30 th Mar. to 4 th Nov.
		pp	900 GeV	2 nd , 3 rd and 27 th May
		Pb-Pb	2.76 TeV	9 th Nov. to 6 th Dec.
	2011	pp	7 TeV	21 th Feb. to 4 th Nov.
		pp	2.76 TeV	24 th to 27 th Mar.
		Pb-Pb	2.76 TeV	5 th Nov. to 7 th Dec.
	2012	pp	8 TeV	5 th Apr. to 16 th Dec.
	2013	p-Pb	5.02 TeV	20 th Jan. to 10 th Feb.
		pp	2.76 TeV	11 th to 14 th Feb.
Run 2	2015	pp	13 TeV	3 rd Jun. to 19 th Nov.
		pp	5.02 TeV	19 th to 23 rd Nov.
		Pb-Pb	5.02 TeV	24 th Nov. to 13 th Dec.
	2016	pp	13 TeV	23 rd Apr. to 26 th Oct.
		p-Pb	5.02 TeV	4 th to 17 th Nov. 4 th to 5 th Dec.
		p-Pb	8.16 TeV	18 th to 25 th Nov.
		Pb-p	8.16 TeV	26 th Nov. to 4 th Dec.
	2017	pp	13 TeV	23 rd May to 26 th Nov.
		pp	5.02 TeV	11 th to 21 st Nov.
		Xe-Xe	5.44 TeV	12 th Oct.
	2018	pp	13 TeV	12 th Apr. to 23 th Oct.
		Pb-Pb	5.02 TeV	7 th Nov. to 2 nd Dec.

Table 3.3: Summary of the LHC Run 1 and 2 physics programmes with the data taking periods in the rightmost column [103].

gradually increases over the years, from 0.9 TeV to 2.36 and then 7 TeV in 2011, and 8 TeV in 2012. The proton-proton programme is complemented by Pb-Pb collisions at $\sqrt{s_{\text{NN}}} = 2.76$ TeV in November 2010 and 2011, followed in early 2013 by the first p-Pb run at a centre-of-mass energy per nucleon of 5.02 TeV. A few days later, the collider enters in a long shutdown (LS1), marking the end of the first campaign of data taking now called Run-1 (2009-2013). During this period, the LHC undergoes maintenance operations and preparations in view of an increase by a factor two of

both energy (reaching $\sqrt{s} = 13$ TeV in pp collisions) and luminosity⁷ (bunches of protons are separated by 25 ns instead of 50 ns).

In spring 2015 begins the second campaign of data taking, the LHC Run-2. The latter opens with pp collisions at a record energy of 13 TeV, which will be the default collision energy in pp until the end of the Run-2. The same goes for heavy-ion collisions: the Pb-Pb and p-Pb data are now collected at $\sqrt{s_{\text{NN}}} = 5.02$ TeV, and up to 8.16 TeV in the latter case. Note also the presence of a short Xe-Xe run at $\sqrt{s_{\text{NN}}} = 5.44$ TeV in October 2017. The Run-2 comes to an end on December 2018; the LHC enters in its second long shutdown (LS2). As for the LS1, this is the opportunity for the collider and its experiments to be renovated and upgraded.

On the 5th of July 2022, the LHC restarts and delivers its first pp collisions – almost four years after the start of the LS2 – at the new record energy of 13.6 TeV, signalling the beginning of the Run-3.

II The ALICE collaboration

Amongst the different collaboration based at CERN, ALICE holds a particular place since the work presented in this manuscript has been realised within this experiment. As mentioned above, it aims at studying the properties of strongly interacting matter and particularly under extreme energy densities where the quark-gluon plasma is formed (Sec. II).

II-A The collaboration

As of March 2023, the ALICE collaboration counts 2084 physicists, engineers, technicians and students from 174 institutes in 41 countries. Most of its members originate from Europe (France, Italy, Germany,...), but also from Asia (China, South Korea, Japan,...) and America (United States, Brazil, Mexico,...). In order to co-ordinate the efforts within the collaboration, ALICE is organised in different boards and committees, each covering a specific scope⁸:

- *The Collaboration Board (CB)* is the highest instance of the collaboration, it can examine and render a decision on any issues from the construction of the detector to the publication policy. It consists in a legislative assembly, mainly composed of the representatives of each member institute (one per member).
- *The Management Board (MB)* supervises the experiment in any matters (scientific, technical, organisational, operational and financial). It plays the role of the executive authority of the collaboration, and is represented by the Spokesperson and its deputies.

⁷This quantity corresponds to a measure of the number of collisions either per unit of time (*instantaneous luminosity*) or over a certain period of time (*integrated luminosity*). In the latter case, it is expressed in inverse barns (b^{-1}) or femtobarns (fb^{-1}).

⁸Only a subset of the ALICE management structure is mentioned. The complete picture is specified in the ALICE Constitution [104].

- *The Resource Board (RB)* deals with the financial aspect of ALICE. Each national funding agency has a seat within this committee.
- *The Physics Board (PB)* coordinates the analysis efforts in order to address the physics goals defined by the CB and MB. It consists in eight Physics Working Groups (PWG), each covering a specific theme, as presented in Tab. 3.4.

<u>Physics Working Group</u>	<u>Topic</u>
<i>PWG-CF</i>	Correlations and Flow
<i>PWG-DQ</i>	Dileptons and Quarkonia
<i>PWG-EM</i>	Electromagnetic probes
<i>PWG-HF</i>	Heavy Flavour
<i>PWG-JE</i>	Jets
<i>PWG-LF</i>	Light-Flavours
<i>PWG-MM</i>	Monte Carlo generators and Minimum bias analysis
<i>PWG-UD</i>	Ultra-peripheral collisions and Diffraction

Table 3.4: The eight working groups of the ALICE Physics Board, as of 2023.

Each PWG is also subdivided in Physics Analysis Group (PAG). For instance, the PWG-Light Flavours includes four PAGs: *Resonances*, *Spectra*, *Nuclei and Exotica*, and *Strangeness*. The present analyses on multi-strange baryons (Chap. 5 and 6) are part of the latter group.

- *The Run Coordination (RC)* is responsible for the operation of the ALICE detector. Amongst its duties, it must ensure efficient data taking, optimal data quality and must define the LHC schedule with the LHC Programme Coordination in order to meet the physics goals of the collaboration.
- *The Editorial Board (EB)* manages the publication process (publication, conference proceedings, internal and technical notes). It is complemented by the *Conference Committee (CC)* that oversees the oral presentations (talk or poster) outside of the collaboration.

This structure is quite common in high-energy experiments, most of the collaboration are being organised in this way. With different denominations perhaps, but the essence stays the same.

II-B The detector

The ALICE detector sits in a cavern 56 m below the ground, in the vicinity of Saint-Genis-Pouilly in France. It is located at the interaction point 2 of the LHC, where the L3 experiment at the former LEP collider was installed. From the latter only remains the gigantic red octagonal solenoid magnet, now symbol of the ALICE collaboration.

Being the only experiment dedicated to studying the QGP, ALICE has been designed as general-purpose detector capable of accessing a large number of observables. The physics targets impose several design constraints.

The apparatus must be able to operate in a high-multiplicity environment, considering that the charged particle density per unit of rapidity in the most violent Pb-Pb collisions may reach $dN_{\text{ch}}/d\eta = 2035 \pm 52$ [105]. For that reason, high granularity detectors – such as the Inner Tracking System – are employed to ensure an excellent reconstruction of the primary and secondary vertices, especially close to the interaction point. In fact, the design of ALICE was optimized to endure values up to $dN_{\text{ch}}/d\eta = 4000$, and twice as much in simulations.

To gain as much insights as possible on the QGP evolution, most of the measurements shall be achievable over a wide momentum range, spanning from very low transverse momentum (~ 100 MeV/c) – where most of the particle production is – up to large transverse momentum (≥ 100 GeV/c). This requires reducing the multiple scattering at low p_{T} , and thus using extremely thin detectors. At central rapidity, the material budget amounts to 13% radiation length, X_0 ⁹, up to Time Projection Chamber outer wall¹⁰. For comparison, it is about 47% and 40% X_0 in ATLAS and CMS at the end of their inner tracker [99][100], and 17.5% X_0 down to the VELO (VERtex LOcator) for LHCb [102]. At high p_{T} , the constraint lies in the need for a good resolution at large transverse momentum. This is achieved by means of a large tracking lever arm thanks to the Time Projection Chamber, that extends up to 2.5 m.

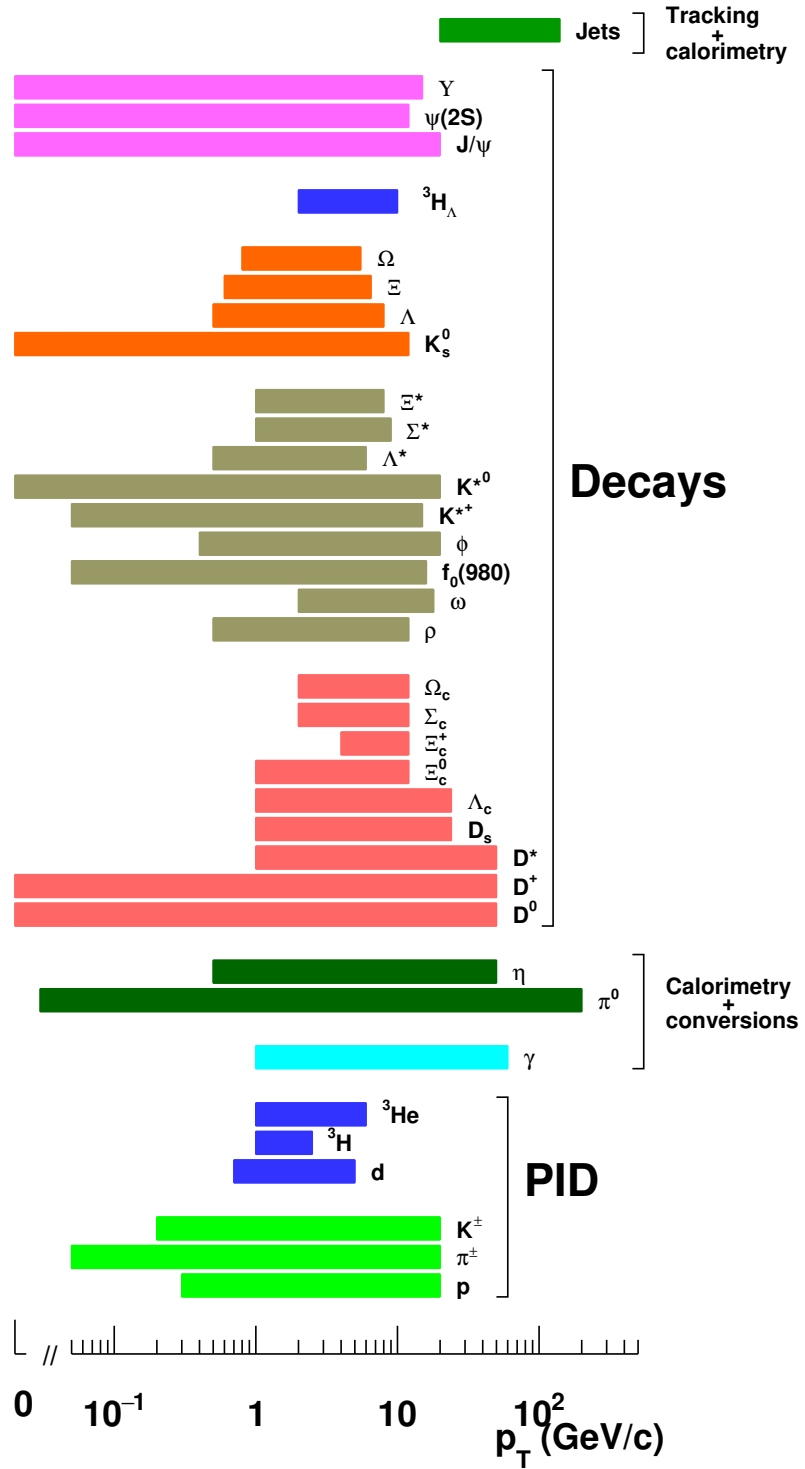
This brings an extra consideration. In order to avoid excessively bending the low p_{T} charged particles and making them impossible to detect, the momentum measurement down to 100 MeV/c necessitates a moderate magnetic field of 0.5 T¹¹. In return, the high p_{T} charged particles are less curved resulting in a reduction of the momentum resolution, when they are still measurable.

Along the same line, many observables depend on the nature of the particle, and so it is essential to have a robust particle identification (PID) over a wide momentum range. To that end, ALICE exploits all the PID techniques on the market: ionization energy loss in the Time Projection Chamber, time-of-flight measurement with the Time-Of-Flight detector, Cerenkov and transition radiations in the High-Momentum Particle Identification Detector (HMPID) and Transition Radiation Detector (TRD) respectively, energy measurement with the Electromagnetic Calorimeters (EMCal) and the Photon Spectrometer (PHOS). The Fig. 3.3 provides

⁹This is the characteristic amount of matter over which a high-energy electron loses all its energy by bremsstrahlung (*i.e.* deceleration via the emission of photons) but $1/e$. It is expressed in g.cm⁻² [42].

¹⁰Here, there are two antagonistic constraints: the detectors must be thin and radiation tolerant in order to function in a high-multiplicity environment, the latter requiring relatively thick materials. However, in ALICE, the interaction rate in heavy-ion collisions is low (about 10 kHz or 10 000 Pb-Pb collisions per second) such that the radiation doses are rather mild, compared with the levels in ATLAS and CMS (790 and 840 kGy respectively): the total dose over the period of a LHC-Run varies between tens of Gy for the furthest parts of the Inner Tracking System to 2.7 kGy close to the interaction point.

¹¹Among the four main LHC experiments, this is the most moderate magnetic field. For comparison, CMS uses a magnetic field of 4 T, the same as the LHCb dipole magnet, and ATLAS solenoid magnet delivers a 2 T field.



ALI-PUB-528808

Fig. 3.3: ALICE particle identification and reconstruction as a function of p_T . Figure taken from [84].

an overview of the PID and reconstruction capabilities with the transverse momentum coverage.

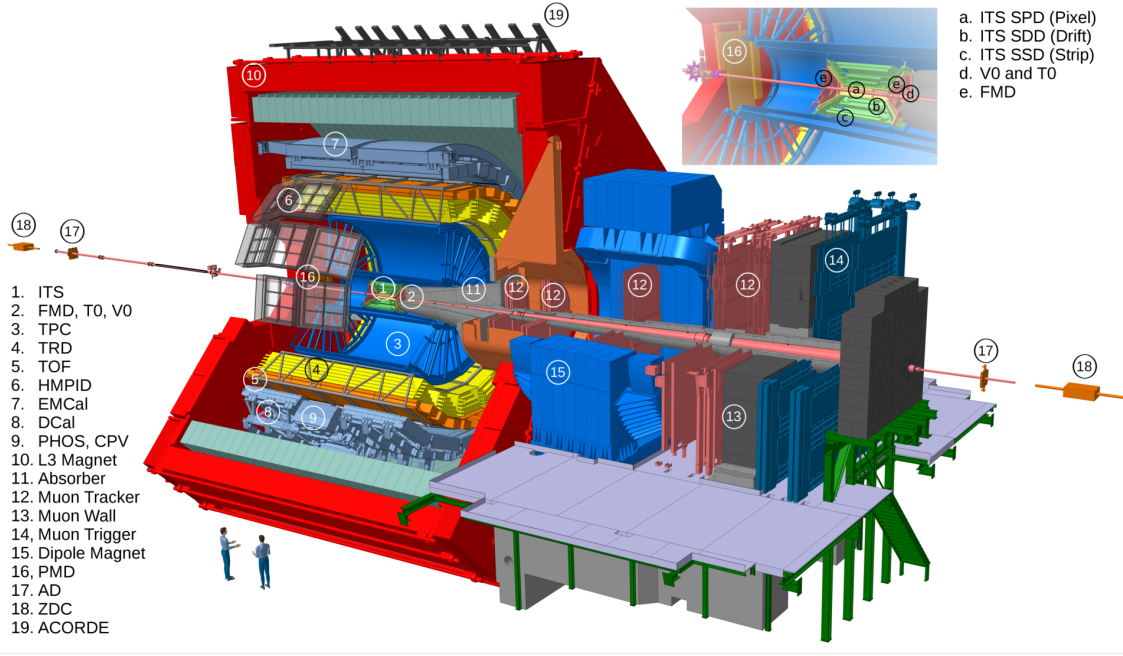


Fig. 3.4: Schematic representation of the ALICE apparatus, as it was operated in the LHC Run-2. Figure taken from [84].

Fig. 3.4 provides a overview of the different elements of the detector. It comprises 19 detection systems organised in two groups: the ones in the central barrel at mid-rapidity ($|\eta| < 0.9$), embedded in the L3 solenoid magnet that delivers a homogenous magnetic field up to 0.5 T; the others at forward rapidity ($-4 < \eta < -2.5$), dedicated to muon detection. An exhaustive description of the ALICE apparatus can be found in [101], as well as its physics performances in [106][107][108]. In the next paragraphs, we will concentrate on the main detectors employed in this thesis, namely the Inner Tracking System (Sec. II-B.i), the Time Projection Chamber (Sec. II-B.ii), the VZERO (Sec. II-B.iii) and the Time-Of-Flight detector (Sec. II-B.iv).

Before proceeding, a note on the location of the different parts of the apparatus: in the cartesian coordinate system of ALICE, the origin lies at the centre of the central barrel and the z -axis coincides with the beams. The elements located on positive z belongs to the A-side (beam circulating in Anti-clockwise direction, from ALICE to the ATLAS interaction point), the others with negative z are on the C-side (beam going in Clockwise direction, from ALICE to the CMS interaction point). The y -axis points towards the top of the detector and the x -axis is in the horizontal plane, going towards the centre of the LHC ring. Moreover, there exists a cylindrical coordinates system based on the distance from the origin r and the azimuthal angle φ in the transverse plane xy , as well as a spherical one with an additional angle, the zenithal angle denoted θ .

Layer	r (cm)	$\pm z$ (cm)	Area (m ²)	Active area per module (mm ²)	Resolution $r\varphi \times z$ (μm ²)	Material budget (% X_0)
1 - SPD	3.9	14.1	0.07	12.8 × 69.6	12 × 100	1.14
2 - SPD	7.6	14.1	0.14	12.8 × 69.6	12 × 100	1.14
3 - SDD	15.0	22.2	0.42	72.5 × 75.3	35 × 25	1.13
4 - SDD	23.9	29.7	0.89	72.5 × 75.3	35 × 25	1.26
5 - SSD	38.0	43.1	2.20	73 × 40	20 × 820	0.83
6 - SSD	43.0	48.9	2.80	73 × 40	20 × 820	0.86

Table 3.5: Details on the six layers of the ITS during the LHC Run-1 and Run-2. [101][106]. The radial distance r are, in fact, average positions. The rightmost column only includes the material budget of the sensor.

II-B.i Inner Tracking System

The Inner Tracking System (ITS) of ALICE is the closest detection system to the interaction point. It surrounds the beam pipe, a 800 μm-thick beryllium cylinder with an average radius of 2.9 cm. The ITS is designed in order to i) estimate the primary vertex position to a precision better than 100 μm, ii) reconstruct secondary decay vertices of relatively short lifetime particles such as hyperons, D or B mesons, iii) track and identify particles whose $p_T \leq 200$ MeV/c, iv) bring constraints on the particles reconstructed by the Time Projection Chamber and, by so doing, improve the momentum and angle resolution, v) enhance PID capabilities of the ALICE apparatus, and finally vi) provide additional trigger information. As shown on the Fig. 3.5, the ITS is made of six coaxial cylindrical layers of silicon detectors based on three different technologies. The two innermost layers are the Silicon Pixel Detectors (SPD), followed by the two layers of Silicon Drift Detector (SDD). The two outermost layers utilizes Silicon Strip Detectors (SSD). The number of detector, and their positionning, has been optimized in order to guarantee efficient track reconstruction and highly precise estimation of the impact parameter. The pseudo-rapidity coverage varies from a layer to another, but taken as a whole, the ITS covers a range of $|\eta| < 0.9$ for all interaction point within ± 5.3 cm along the beam direction. Its overall material budget of 7.18% X_0 (including the silicon detectors, thermal shields, electronics, support structure, cooling system) makes it the only device capable of detecting low- p_T particles, with a relative momentum resolution better than 2% for pions with momentum between 100 MeV/c and 3 GeV/c. Some important characteristics of the ITS are reported in Tab. 3.5.

The two innermost layers are positionned at 3.9 and 7.6 cm from the origin, covering a pseudo-rapidity range of $|\eta| < 2$ and $|\eta| < 1.4$ respectively. At this distance, the track density can reach values up to 80 tracks/cm². In order to cope with these high track densities, the layers are equipped with SPD employing hybrid¹² silicon

¹²The term *hybrid* here refers to a type of pixel technology in which the silicon sensor and the readout chip are processed separately and connected together via a bump-bonding process. In this way, the detector (silicon sensor) and the electronics (readout chip) can be optimized individually. In LHC experiments, the optimisation is performed such that the detector has a good radiation tolerance and the readout is fast. In return, the assembly tends to be more complex and expensive,

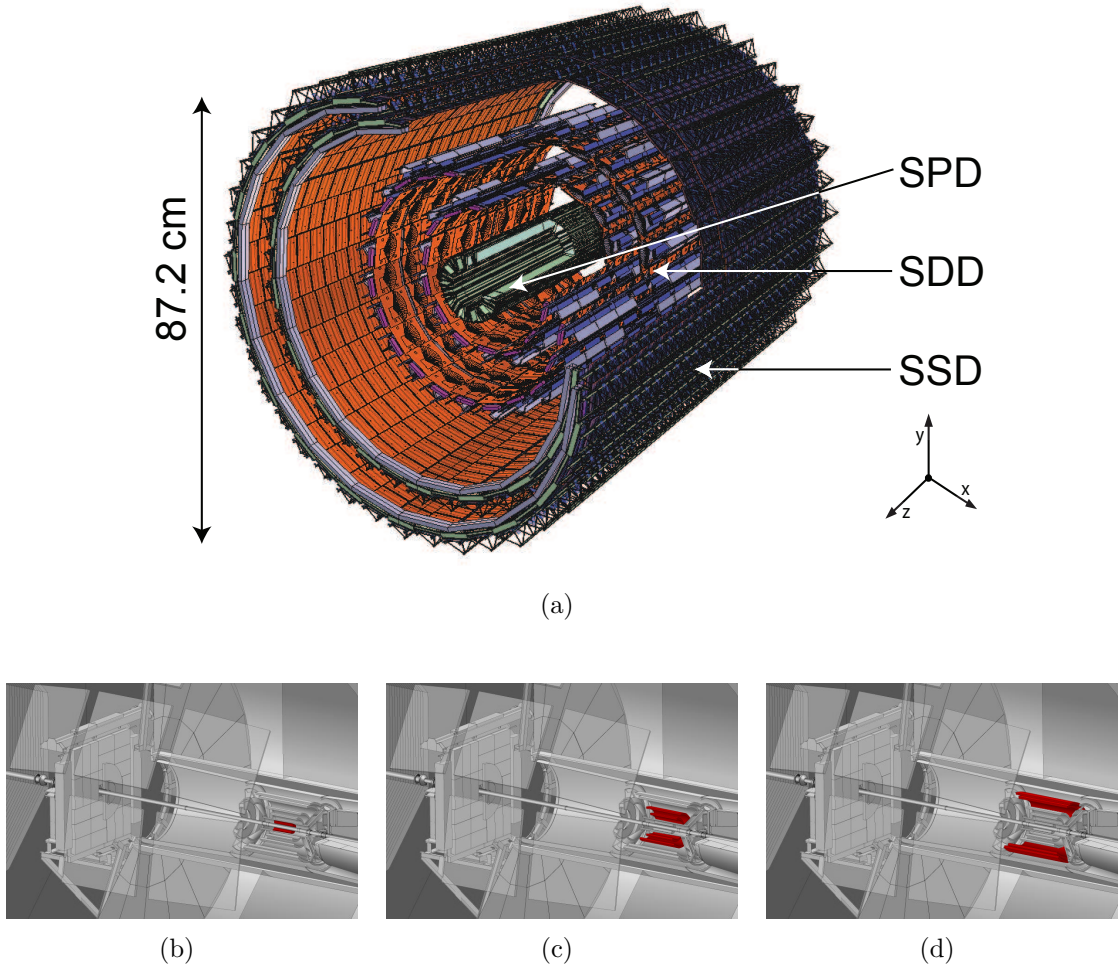


Fig. 3.5: Visualisation of the complete structure of the ITS detector (a), as well as a highlight on the SPD(b), SDD(c) and SSD(d) locations in the ALICE apparatus. Figures taken from [109][110].

pixels. It consists of a bi-dimensional matrix of 256×160 cells of dimension $50 \mu\text{m}$ ($r\varphi$) by $425 \mu\text{m}$ (z). Two matrices are mounted together along the z direction, forming a 141.6 mm long half-stave. Two of them are attached head to head along the beam direction on a carbon-fibre support with cooling tubes in order to forge a stave. The latter are arranged in ten sectors surrounding the beam pipe, each sector supporting two staves for the inner layer and four for the outer layer. While the high granularity of the SPD provides a spatial resolution of $12 \mu\text{m}$ in $r\varphi$ and $100 \mu\text{m}$ along z , its fast integration time of 100 ns – corresponding to four consecutive bunch-crossings in pp collisions or one in heavy-ions operation – offers additional trigger information.

The SDDs equip the two intermediate layers at an average distance of 15.0 and 23.9 cm, where the track density rises up to 7 tracks/cm 2 . Both layers have a pseudo-rapidity acceptance of $|\eta| < 0.9$. The basic module consists in a sensitive area of $70.17 \times 75.26 \text{ mm}^2$, split into two drift regions by a central cathode strip at high voltage such that the drift velocity is $8.1 \mu\text{m/ns}$. At this speed, charges

the readout chips dissipate a lot of power requiring an efficient cooling system and so more material budget.

drift to one of the 256 collection anodes (with a $294\text{ }\mu\text{m}$ pitch) in a maximum time of $4.3\text{ }\mu\text{s}$, making it the slowest ITS detector. The SSD modules are mounted on triangular support structure made of carbon-fibre called ladders. The third layer counts 14 ladders with six modules each, and 22 ladders with eight detectors each for the fourth layer. They yield to a spatial precision of $35\text{ }\mu\text{m}$ in the transverse plane and $25\text{ }\mu\text{m}$ along the beam axis. Because of the sensitivity of the SDD layers to temperature changes, two thermal shields surround them in order to avoid any radiation of heat.

The two outermost layers are constituted of double sided SSD of $73 \times 40\text{ mm}^2$, where each side has 768 parallel strips (with a pitch of $95\text{ }\mu\text{m}$) and corresponds to a side of a p-n junction. The p-side (n-side) of the fifth layer (sixth layer) faces the inside of the ITS. The strips from one side are rotated by a stereo angle of 35 mrad with respect to the other, to reduce the overlapping between the strips and thus the number of ambiguities. The SSD modules are assembled on the same ladder design as those of the intermediate layers: 34 ladders, supporting 22 modules each, are installed on average at 38 cm from the beam pipe for the inner layer and 38 ladders, holding 25 modules each, at 43 cm for the outer layer. Both covers a pseudo-rapidity region of $|\eta| < 0.9$. The SSDs layers provide a spatial resolution of the track position of $20\text{ }\mu\text{m}$ in the $r\varphi$ direction and $820\text{ }\mu\text{m}$ along z , which is essential for the track matching from the Time Projection Chamber to the ITS. Similarly to the SDD layers, its analogue readout allows for the measurement of the charge deposited by the passage of a charged particle, and hence opens the door for PID of low-momentum particles.

II-B.ii Time Projection Chamber

The Time Projection Chamber (TPC) is the main tracking device of the ALICE detector. It is responsible for measuring the momentum of charged particle above $150\text{ MeV}/c$, as well as providing particle identification and primary vertex determination (addressed in more details in Sec. II-D.iii). The TPC design is shown in Fig. 3.6(a). It consists in a cylindrical gaseous detector, surrounding the ITS, with an inner radius of about 85 cm, an outer radius of 250 cm and an overall length of 500 cm along the beam axis. The acceptance of the TPC covers pseudo-rapidities from $|\eta| < 0.9$ (for tracks traversing radially the entire ALICE detector) up to $|\eta| = 1.5$ and the full azimuth (except for the dead zones between sectors). Although it is the largest sub-detector of ALICE, its material budget remains quite low (about 3.5% X_0).

The detection volume corresponds to a field cage filled with gas and separated in two equal parts, along the beam axis, by a central electrode at -100 kV. At this high voltage, this central membrane generates an axial electrostatic field of 400 V/cm. When a charged particle traverses the 88 m^3 of TPC's active volume, it creates electron-hole pairs along its path by ionisation of the gas. The electrostatic field forces the electrons to drift from the central electrode to the end plates, where they are collected, in a maximum time of $92\text{ }\mu\text{s}$ at a speed of $2.7\text{ cm}/\mu\text{s}$ (depending on the gas composition).

Each end plate is segmented into 18 trapezoidal sectors (as represented in



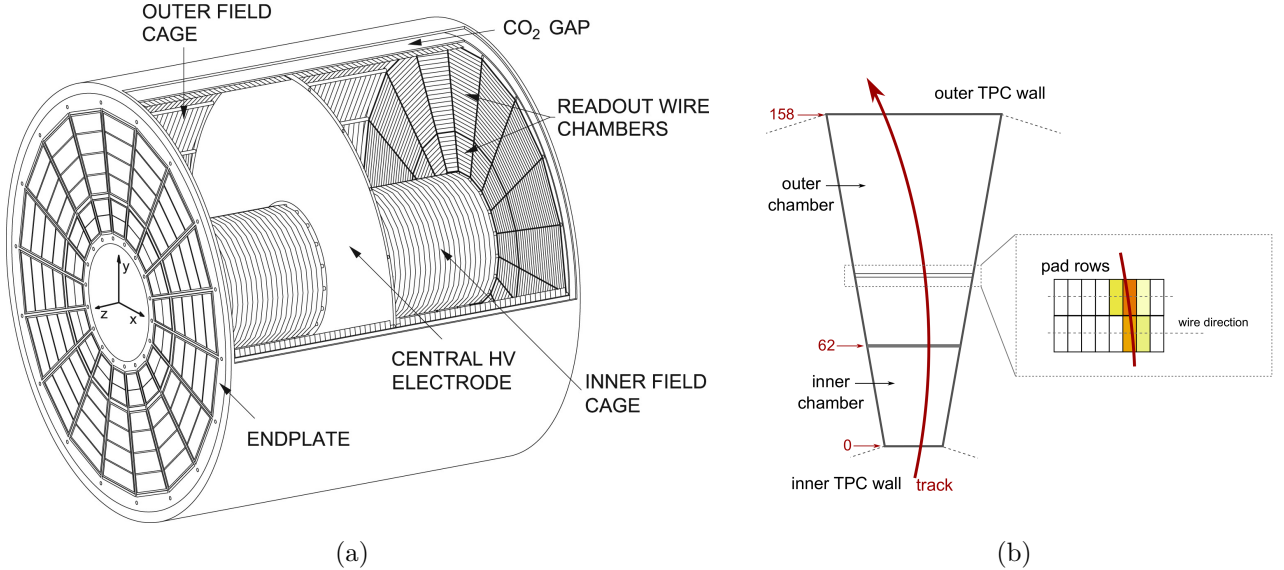


Fig. 3.6: (Left panel) Scheme of the TPC field cage, taken from [111]. (Right panel) Passage of a charged particle through a sector of the TPC. Figure taken from [112].

Fig. 3.6(b)), being themselves instrumented with two multi-wire proportionnal chambers (MWPC) with cathode pad readout: one stretches from $R = 84.8$ cm to 132 cm (inner chamber), the other from 134.6 cm to 246.6 cm (outer chamber). This is motivated by the variation of the track density with the radial distance (from the primary vertex), that requires MWPCs with different wire geometry and pad sizes (granularities). Together, the two chambers count a total of 159 readout pad rows: 63 of 4×7.5 mm² for the inner chamber, 64 of 6×10 mm² and 32 of 6×15 mm² for the outer chamber. They measure the deposited charge, as well as the radial position and the drift time. The longitudinal coordinate is inferred from the latter, provided that the drift speed is uniform over the whole volume¹³. In fact, the gas composition has been optimised for high and stable drift velocity, as well as low diffusion and small radiation length. At the start of the LHC Run-2, a mixture of Ne/CO₂/N₂ (90/10/5%) was employed. For the data taking campaign of 2017, it was replaced for Ar/CO₂ (90/10%) before switching back to the initial gas composition in 2018, as it turns out that the latter yields to a reduced space-charge distortion.

The spatial resolution varies from 1100 to 800 μm in the transverse plane, and 1250 to 1100 μm along the beam axis. Although the TPC can not compete with the degree of precision of the ITS, it stands as the main tracking detector in ALICE thanks to its almost continuous sampling of the particle trajectory over large distances.

Moreover, the pad rows provides an analogue readout of the charge deposition, which is used to measure the energy loss of charged particles per unit of length (dE/dx) with a resolution (σ_{TPC}) ranging from 5.2% in pp events to 6.5% in the most central Pb-Pb collisions. As the energy deposition is stochastic phenomenon by nature, only the moments of its underlying distribution can be predicted. For

¹³The longitudinal position is given by the product of the drift velocity and the drift time, $v_{\text{drift}} \cdot t_{\text{drift}}$.

instance, the Bethe-Bloch formula describes the mean dE/dx :

$$\begin{aligned} \left\langle -\frac{dE}{dx} \right\rangle &= K z^2 \frac{Z}{A} \frac{1}{\beta^2} \left[\frac{1}{2} \ln \frac{2m_e c^2 \beta^2 \gamma^2 T_{\max}}{I} - \beta^2 - \frac{\delta(\beta\gamma)}{2} \right], \\ \beta\gamma &= \frac{p}{Mc} \end{aligned} \quad (3.1)$$

with

- Z , the atomic number of the absorber (the TPC gas in this case),
- A , the atomic mass of the absorber ($\text{g}\cdot\text{mol}^{-1}$),
- m_e , the electron mass,
- z , charge number of the incident ionising particle,
- M , mass of the incident ionising particle,
- p , momentum of the incident ionising particle,
- β , velocity of the incident ionising particle in units of c ,
- γ , Lorentz factor of the incident ionising particle,
- I , mean excitation energy of the absorber,
- $\delta(\beta\gamma)$, density effect correction due to the polarisation of the absorber,
- $T_{\max} = \frac{2m_e c^2 \beta^2 \gamma^2}{1+2\gamma m_e/M+(m_e/M)^2}$, the maximum energy transfer to an electron in a single collision,
- K , an independent constant of the ionising incident particle or the absorber.

As a matter of fact, the energy deposition follows a Landau distribution. Its broad tail on the high-energy-loss side leads the mean energy loss to be significantly greater than the most probable value. However, the most probable energy loss is much easier to evaluate than the mean that requires large samples to converge. Thereby, the Landau distribution is usually truncated to keep only the 50 to 70% smallest values, and by so doing, the truncated mean coincides with the most probable energy loss [42].

Fig. 3.7 shows clearly the characteristic dE/dx bands associated to e, π , p, d, t, ${}^3\text{He}$ and ${}^4\text{He}$. The measurements distribute around dashed lines, that correspond to the expected mean value given by the Bethe-Bloch formula (Eq. 3.1). By comparing the measured value to the expected energy loss for various particle species, the nature of the incident particle can be determined. The PID estimator,

$$n_\sigma = \frac{\langle dE/dx \rangle_{\text{meas}} - \langle dE/dx \rangle_{\text{exp,i}}}{\sigma_{\text{TPC}}}, \quad (3.2)$$

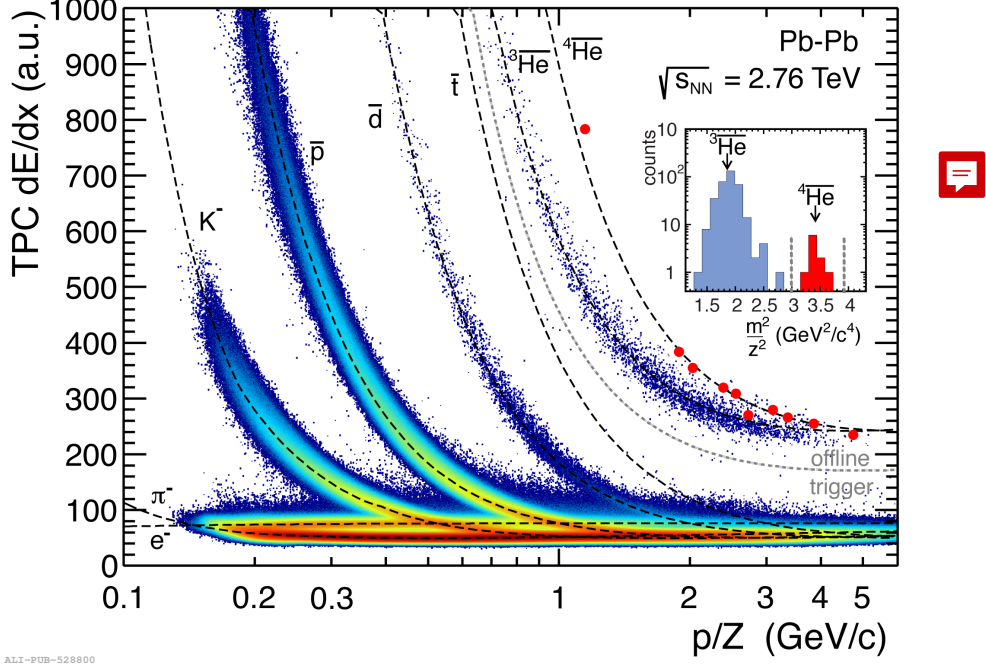


Fig. 3.7: Energy deposition of various charged particles (electron, pion, kaon, anti-proton, anti-deuteron, anti-tritium, and two anti-helium isotopes) in the ALICE TPC in arbitrary units as a function of the magnetic rigidity (momentum over charge number). The dashed lines correspond to the theoretical expectations for each particle species. Figure taken from [84].

gives the distance between measured dE/dx and the expected one under the particle mass hypothesis m_i ($i = e, \pi, p, d, t, {}^3\text{He}, {}^4\text{He}$), in units of relative resolution σ_{TPC} . Therefore, the TPC is able to distinguish a pion/electron from a kaon with a separation power better than 3σ below $\sim 300 \text{ MeV}/c$, and a kaon from a proton up to $1 \text{ GeV}/c$.

II-B.iii VZERO

The VZERO system consists in two scintillator arrays, VZERO-A and VZERO-C, covering the pseudo-rapidity ranges $2.8 < \eta < 5.1$ and $-3.7 < \eta < -1.7$ respectively (Fig. 3.8(a)). It plays a crucial role in the data taking of ALICE as it provides minimum-bias triggers for the experiment, measures the charged particle multiplicity and centrality, and participates in the beam luminosity determination.

Each array is segmented in four rings, themselves being divided in eight sections, for a total of 32 cells made of 45° wide plastic scintillators, as sketched in Fig. 3.8(b). Because of the integration constraints (mainly coming from the muon absorber), the arrays come in two different designs. The 2.5 cm thick VZERO-A sits at $z = 329 \text{ cm}$ from the origin of the detector ($z = 0$). Since the VZERO-C stands in front of the muon absorber, the scintillator thickness has been reduced to 2 cm and its rings are positioned between -86 and -88 cm along the beam axis.

The passage of a charged particle in the scintillator generates light, that is guided to photomultiplier tubes via 1 mm in diameter Wave-Length Shifting and

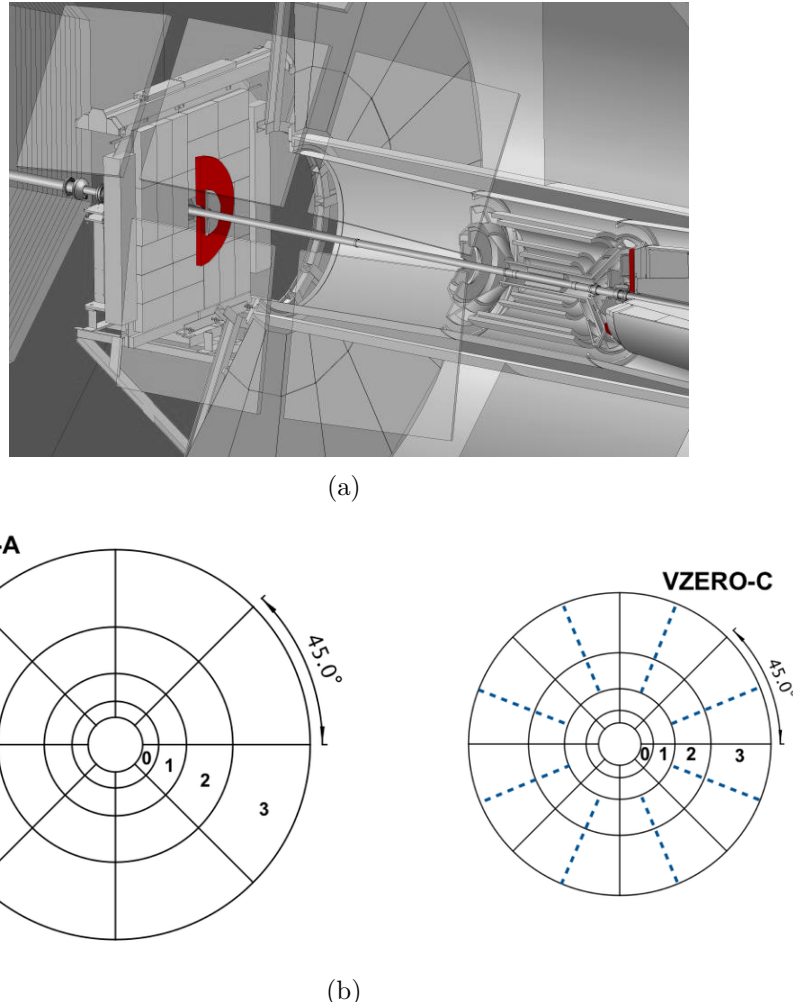


Fig. 3.8: (Top panel) View of the VZERO scintillator arrays inside the ALICE apparatus: VZERO-A on the left, and VZERO-C on the right. (Bottom panel) Sketches of the VZERO-A (left) and VZERO-C (right) with their segmentation. The dashed lines delimit segments connected to the same photomultiplier tube. Figures taken from [84][113].

optical fibers. For each of the 32 elementary cells, the photomultiplier tube outputs two analogue signals. The first measures the integrated charge, the second – amplified by a factor 10 – determines the pulse/arrival time relative to the LHC bunch clock with a resolution better than 1 ns. Each signal gives rise to a specific type of trigger algorithm.

Based on the coincidence between the time signals from the arrays, beam-induced background events¹⁴ can be rejected. Fig. 3.9 shows an example of such rejection. A particle coming from the interaction point takes about 11 ns and 3 ns to reach the VZERO-A and the VZERO-C respectively. If the signals measured in the both scintillator arrays matches these values — as in the top right corner of Fig. 3.9 —, this indicates that a beam-beam collision has occurred. However, the signals arriving in coincidence at -12 ns (VZERO-A) and 3 ns (VZERO-C), and 11 ns (VZERO-A) and -3 ns (VZERO-C) are not the signatures of a beam-beam

¹⁴They typically correspond to beam-gas collisions, that is a collision between a bunch from the beam and a residual gas molecule in the beam pipe

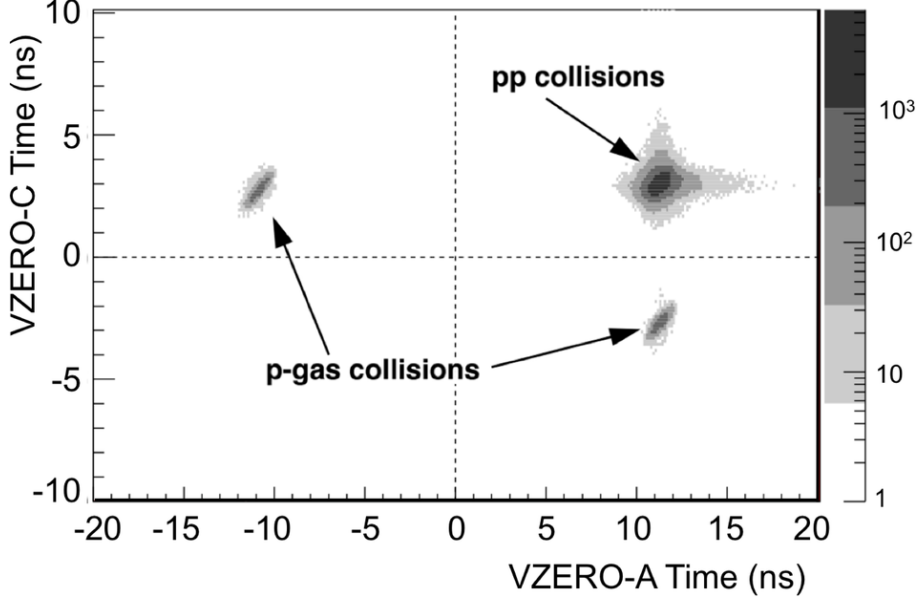


Fig. 3.9: Time of flight of the particles detected in the VZERO-C versus VZERO-A. Figure taken from [113].

event. They correspond to beam-gas collisions coming from the A-side and C-side respectively. This is the first type of trigger algorithm.

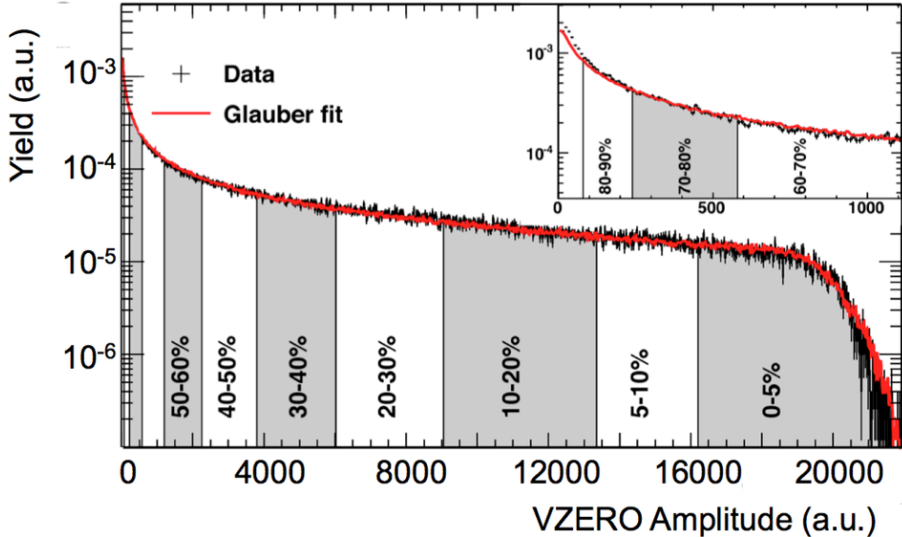


Fig. 3.10: Total yield as a function of the signal amplitudes in the two VZERO arrays in Pb-Pb collisions at $\sqrt{s_{\text{NN}}} = 2.76$ TeV, fitted with a Glauber model in red. The shaded areas correspond to different centrality classes. Figure taken from [113].

The energy deposited in the scintillators provides a measurement of the charged particle multiplicity. Based on a simulation of the VZERO detectors, the total charge collected can be related to the number of primary charged particles, as shown in Fig. 3.10. The second type of trigger algorithm consists in dividing the

distribution of the V0 amplitudes in different multiplicity/centrality¹⁵ classes from the 5%-highest multiplicity to the 10%-lowest multiplicity events, as represented in shaded areas.

II-B.iv Time-Of-Flight detector

The Time-Of-Flight (TOF) detector is a large cylindrical array with an inner radius of 370 cm and an outer one of 399 cm. It covers the central pseudo-rapidity region, that is $|\eta| < 0.9$, and the full azimuth. While the separation power of TPC only goes up to $1 \text{ GeV}/c$, the TOF detector aims at providing particle identification at intermediate momentum from 0.2 to $2.5 \text{ GeV}/c$. To instrument this large volume (17.5 m^3), a gaseous detector is employed, as its manufacture turns out to be relatively simple and thus quite inexpensive. The best solution, with respect to the design considerations of the experiment, is the Multi-gap Resistive-Plate Chamber (MRPC) [114].

The basic constituent of the TOF system is a pair of MRPC strips, 122 cm in length and 12 cm in width, stacked together with an active area of $120 \times 7.4 \text{ cm}^2$. As shown in Fig. 3.11(a), it consists in two cathodes and a central anode in a gas volume, and spaced by five 0.4 mm thin glass plates (with a $250 \mu\text{m}$ gap) for each strip. The full volume is filled with a gas mixture composed of $\text{C}_2\text{H}_2\text{F}_4$ (90%), C_4H_{10} (5%), SF_6 (5%), as it shows no ageing effects and has a rate capability much higher than the expected rate in ALICE [115].

To cover the full cylinder along the beam direction and minimise the cumulative dead areas from the innermost to outermost detectors in ALICE, five modules of different lengths are combined. The central element utilizes 117 cm long module, the intermediate ones 137 cm, the external ones 177 cm made of 15 MRPC strips for the central module and 19 for the others. Altogether, they form a supermodule of total length 930 cm with an overall active region of $741 \times 7.4 \text{ cm}^2$, as shown on Fig. 3.11(b). Each of the 18 azimuthal sectors of the TOF system has a supermodule.

When a charged particle traverses the active volume, it ionises the gas along its path and produces electrons that drift to one of the cathodes. The key aspect of the MRPC resides in the high voltage of the anode (-13 kV), which delivers a high and uniform electrostatic field. The latter is sufficiently strong to start an avalanche process¹⁶, and thereby to give rise to a detectable signal. The avalanche stops when it reaches a glass plate, but the produced electrons continue to drift – and to create avalanches in the gaseous medium along the way – until they are collected by the

¹⁵In heavy-ion collisions, the impact parameter – and, *a fortiori*, its percentage value, the centrality – cannot be measured directly, but the number of charged particle is measurable using – among others – the VZERO detectors. Since the centrality and the charged particle multiplicity in the event are correlated, the latter allows to recover the centrality (as confirmed by the Glauber fit in Fig. 3.10, that also gives access to the centrality). Hence, for heavy-ion collisions, the different intervals in multiplicity in Fig. 3.10 are referred as *centrality classes*.

¹⁶Let us consider a medium containing free electrons and in which a strong electrostatic field exists. If the latter is strong enough, it accelerates the electrons such that they will collide with other atoms in the medium, thus ionising them and releasing additional electrons. These ones also get accelerated and collide with other atoms, releasing more electrons, and so on. This chain reaction is called an avalanche process.

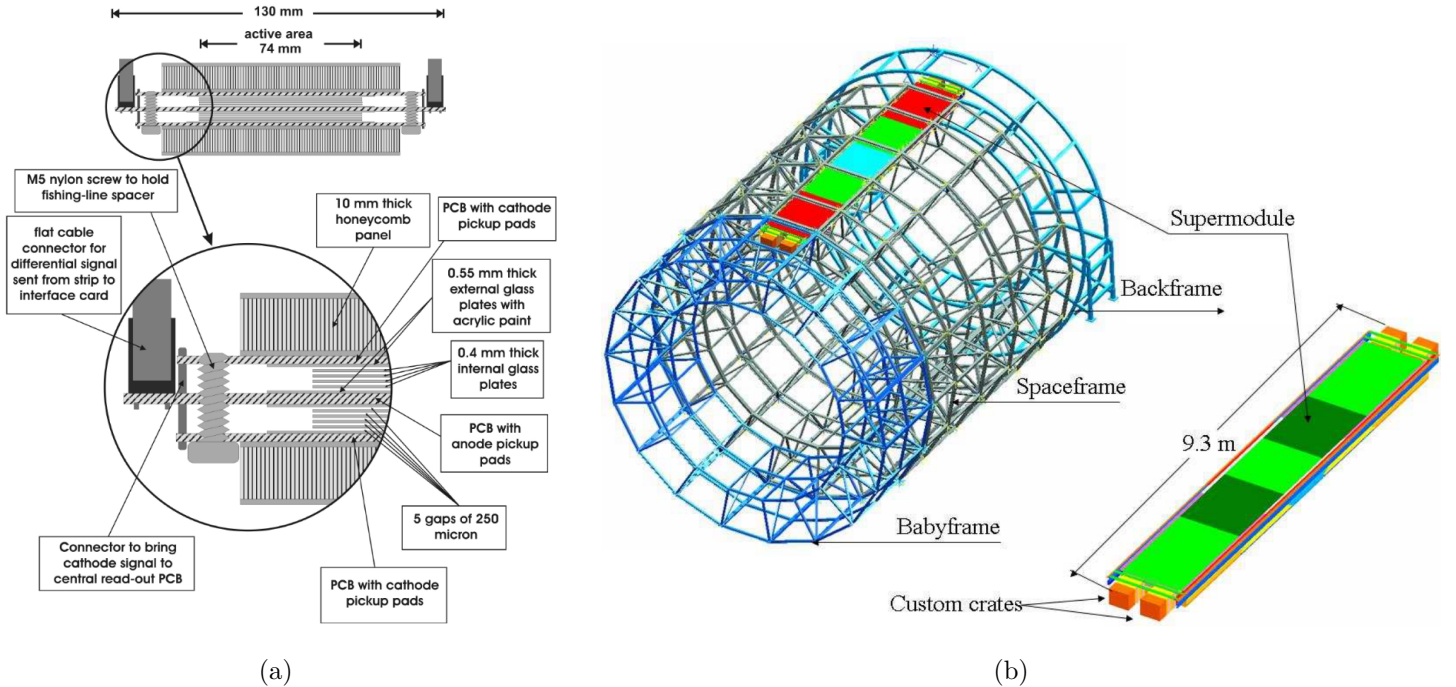


Fig. 3.11: (Left panel) Drawing of the cross section of a 10-gap double-stack MRPC. (Right panel) Schematic view of the TOF barrel with one supermodule, consisting of five modules. Figure taken from [101].

48 cathode pad readouts of $3.5 \times 2.5 \text{ cm}^2$ from each strip.

Their output signals carry informations on the deposited charge via the Time-Over-Threshold and the hit times relative to the collision time, t_{ev} , with an intrinsic resolution of 56 ps during the LHC Run-2. Due to the finite size of the colliding bunches, t_{ev} has to be measured on an event-by-event basis. To that end, different options are available.

The most precise measurement of the collision time is provided by the T0 detector. It consists in two arrays, each made of twelve Cerenkov counters, placed at $z = 375 \text{ cm}$ (T0-A) and -72.7 cm (T0-C). They respectively cover the pseudo-rapidity range $4.61 < \eta < 4.92$ and $-3.28 < \eta < -2.97$. Each counter is a quartz radiator of 20 mm in diameter and 20 mm thick, connected optically to a PMT. The readout electronics is quite similar to the one used for the TOF detector, with a dead time below 25 ns. The T0 system gives two time measurements, one for each array, $t_{\text{T0-A}}$ and $t_{\text{T0-C}}$. When both values are available, the average is taken as the start time of the event, $t_{\text{ev}}^{\text{T0}} = (t_{\text{T0-A}} + t_{\text{T0-C}})/2$, with a resolution of 50 and 25 ps in pp and Pb-Pb collisions. If only one of the two counters produces a signal, the collision time is given by either the $t_{\text{T0-A}}$ or $t_{\text{T0-C}}$ taking into account the longitudinal position of the primary vertex (provided by the ITS). Consequently, the resolution deteriorates to 100 and 60 ps in pp collisions for the T0-A and T0-C respectively, and 50 and 30 ps in heavy-ion collisions. Due to its limited acceptance, the triggering efficiency of the detector in coincidence is about 48%, and reaches 60% and 67% for the T0-A and -C individually in pp collisions¹⁷.

¹⁷The triggering efficiency is close to 100% in heavy-ion collisions, due to their inherently high

The TOF system itself can also determine t_{ev} . Based on a sample of particles matching a hit in the detector, a χ^2 -minimisation procedure is performed in order to extract the set of mass hypotheses that minimises their combined time-of-flights. From this set derives the event collision time, denoted $t_{\text{ev}}^{\text{TOF}}$. By construction, this procedure only applies for a minimum number of two tracks, and the resolution improves with the track multiplicity (scaling as $\sim 1/\sqrt{N_{\text{tracks}}}$). It allows to reach time resolution from 80 ps for the low multiplicity events to 20 ps for the high multiplicity events, with efficiencies ranging from 20% to 100% respectively.

Considering the above efficiencies, the collision start time can be obtained from the T0 or TOF measurement ($t_{\text{ev}}^{\text{T0}}$ or $t_{\text{ev}}^{\text{TOF}}$), or even their combination if both are available. In the latter case, the final t_{ev} corresponds to their weighted average, with the inverse of their resolution squared as weighting factors. If none of the preceding procedures is usable, the start time of the event is set on the LHC clock¹⁸ which has a resolution of 200 ps [116].

In any case, the difference between the arrival time t_{TOF} and the moment of the collision t_{ev} gives the *measured time-of-flight* of the charged particle from the primary vertex to the TOF detector. Based on the latter and the flight path length, the velocity of the particle – or rather the ratio of the velocity to the speed of light, $\beta = v/c$ – can be evaluated. The Fig. 3.12 shows the distribution of β for charged particles measured by the TOF detector as a function of their momentum in Pb-Pb events at $\sqrt{s_{\text{NN}}} = 5.02$ TeV. A clear separation of the electron, pion, kaon, proton and deuteron bands is visible. This stems from the relation between the particle mass m , its momentum p and its velocity β :

$$m = \frac{p}{\beta\gamma} = p \sqrt{\frac{1}{\beta^2} - 1} \quad \text{with} \quad \beta = \frac{v}{c} = \frac{L}{ct_{\text{exp}}}, \quad (3.3)$$

$$\Rightarrow t_{\text{exp}} = L \frac{\sqrt{p^2 + m^2}}{cp}. \quad (3.4)$$

In Eq. 3.4, t_{exp} corresponds to the *expected time-of-flight*, *i.e.* the time it would take for a particle of mass m , with a momentum p , to go from the interaction point to the TOF detector following a path of length L . To this quantity is attached an uncertainty coming from the track reconstruction, as it will be detailed in Sec. II-D. By comparing the measured time-of-flight t_{TOF} and the expected one $t_{\text{exp},i}$ for different mass hypothesis m_i ($i = e, \mu, \pi, K, p, d, {}^3\text{He}, {}^4\text{He}$), particle identification can be performed. The PID estimator n_σ is constructed in the following way:

$$n_\sigma = \frac{t_{\text{TOF}} - t_{\text{ev}} - t_{\text{exp},i}}{\sigma_{\text{PID},i}}, \quad \text{with} \quad \sigma_{\text{PID},i}^2 = \sigma_{t_{\text{TOF}}}^2 + \sigma_{t_{\text{ev}}}^2 + \sigma_{t_{\text{exp},i}}^2. \quad (3.5)$$

Therefore, the TOF detector is capable of identifying charged particles in the intermediate momentum range, with a separation power better than 3σ between pions and kaons below 2.5 GeV/ c , and up to 4 GeV/ c between kaons and protons.

multiplicities.

¹⁸In fact, it is set on zero as, after alignment and calibration of the TOF detector, the LHC clock phase has been shifted to coincide with the nominal starting time.

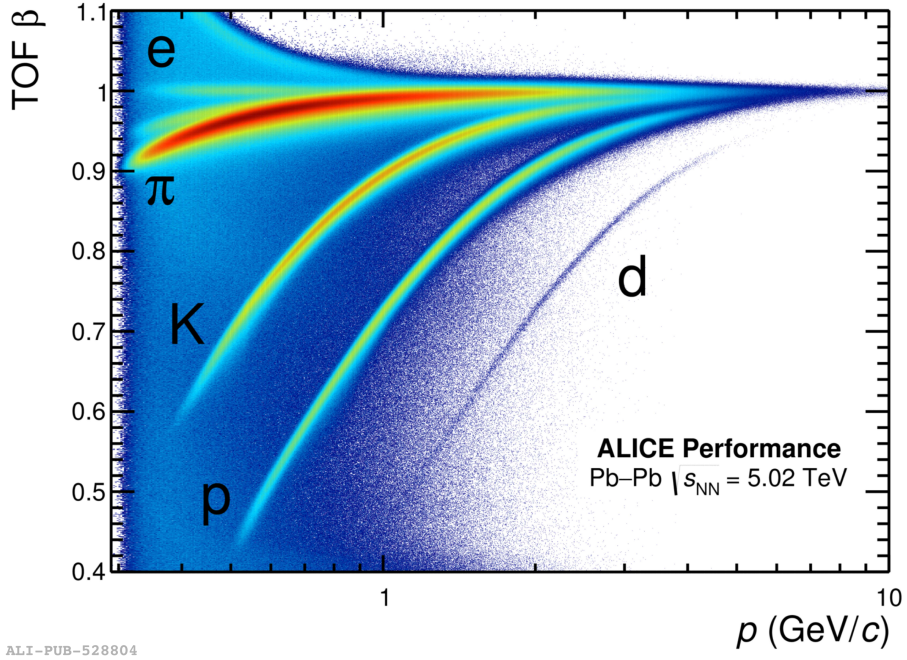


Fig. 3.12: Velocity ($\beta = v/c$) of electrons, pions, kaons, protons and deuterons as a function of their momentum (provided by the TPC), measured by the TOF detector, in Pb-Pb collisions at $\sqrt{s_{\text{NN}}} = 5.02 \text{ TeV}$. Figure taken from [84].

II-C Trigger system and data acquisition

In contrast with its current LHC Run-3 version, ALICE only records triggered data in the Run-1 and Run-2, *i.e.* events are selected and stored based on a variety of different features. The Central Trigger Processor (CTP) is in charge of optimising the trigger system in order to make the best use of i) the various detector components, that are busy for different period of time (~88 μs for the TPC versus the T0 with <25 ns) when a valid trigger signal is received, and ii) the different running modes (pp, pPb, PbPb with specific interaction rates).

The latter is achieved by ensuring that the data collection is not ruined by the pile-up. Here, we refer primarily to event pile-up between different bunch crossings, that is treated differently depending on the expected multiplicity and luminosity. The one occurring between two central or semi-central heavy-ion collisions must be avoided as the density of tracks is so high that they become unreconstructable. However, the pile-up level between a (semi-)central and up to two peripheral Pb-Pb collisions is tolerable in some detectors – such as the TPC – and not in others – the ITS for example. The same applies for pp collisions where pile-up is unavoidable but tracks are reconstructable due to much lower track densities than in Pb-Pb. To that end, a *past-future* protection has been implemented, which basically verifies that the level of pile-up in the sensitive time windows of each detector¹⁹ remains

¹⁹For instance, the past-future protection circuit checks on the TPC that the pile-up occurring between -88 μs (past) and +88 μs (future) relative to the collision time stays manageable. The same logic applies to the rest of the ALICE devices. In fact, three categories of detectors can be drawn out: the ones that can provide a signal at each bunch crossing and thus do not need a

tolerable as defined in the above requirements.

To ensure efficient data taking, the ALICE detector is not entirely readout for every event. Instead, it is divided into groups of sub-systems named detector *clusters*. For instance, the data from the forward muon arm do not need the TPC to be exploitable, only the trigger detectors (in particular the V0 and SPD for determining the centrality/multiplicity class and primary vertex location) are required. By grouping these detectors into the same cluster, they can be read out separately from the other devices. Thereby, the number of detector clusters amounts to three: one for the full detector, another comprising only the central detectors, and a last one including the forward muon detectors and the trigger detectors.

In addition, the hardware trigger system divides into three levels – dubbed L0, L1 and L2 – with different latencies [117][118]. At each LHC clock cycle (that is every 25 ns in pp and 100 ns in heavy-ion mode), the CTP checks for the inputs from detectors with fast trigger capabilities (essentially the T0, V0, SPD and TOF) up to 800 ns after the collision (time needed for the SPD to transmit its trigger signal to the CTP). When the inputs coincide with the requirements of one (or more) *trigger class*²⁰, the trigger system issues a Level 0 (L0) decision in less than 100 ns, that reaches the detectors 1.2 μ s after the interaction. Upon reception of the L0 signal, detectors move into a busy-state in which they stop taking new data until they have been fully read out. Since all the detector inputs can not be transmitted under 800 ns, the CTP collects all the signals that can be delivered under 6.1 μ s, checks the conditions for all trigger classes and – in the absence of a veto from the past-future protection circuit – generates a Level 1 (L1) trigger arriving at the detectors 6.5 μ s after the collision. Together, the L0 and L1 signals represent the fast response of the trigger system. The last signals arrives 87.6 μ s after the collision, due to the drift period of the TPC. A level 2 (L2) trigger decision is sent with a latency of 100 ns and reaches the detectors at 88 μ s, to finally conclude on whether the event is accepted or rejected. At this stage, a rejection most often comes from excessive pile-up.

Among the different trigger classes, two configurations play an important role in ALICE and in the present work: the minimum-bias (MB) and the high-multiplicity (HM) classes. As its name suggests, the former refers to the least biasing conditions for the data acquisition in ALICE over the full multiplicity distribution. Its requirements have evolved over the years, though. Because of the low interaction rate in pp in 2009 and 2010 data takings, the minimum-bias trigger selections were kept loose: it required a hit in either VZERO counters or in one of the two SPD layers (MB_{OR}). In this way, the collected event would have at least one charged particle in eight units of pseudo-rapidity. As the luminosity and the amount of beam-gas background increase, the conditions were tightened up and the high selection efficiency MB trigger is traded off for a high purity one. Hence, to be recorded, an event necessitates a coincidence between the two VZERO detectors (MB_{AND}). This is equivalent of asking for, at least, two charged particles separated by 4.5 units of

protection, the others requiring the application of the past-future condition under 10 μ s, and the TPC demanding a protection under 88 μ s.

²⁰This is the set of detector signals that defines a trigger selection. ALICE counts 50 trigger classes [101].

pseudo-rapidity: one in the A-side, the other in the C-side²¹ [119][120].

The HM trigger corresponds to 0.1% highest multiplicity events from the MB sample; it has been implemented in order to study efficiently rare signals, most particularly in small systems. Throughout the LHC Run-1, it was based on the number of hits in the outer layer of the SPD for the multiplicity estimation. The threshold was typically set between 80 to 100 hits which represent about 60 to 80 pairs of matching clusters between the two SPD layers, also referred as SPD tracklets (HM_{SPD}) [120]. However, in the Run-2, the default HM trigger configuration changes and now relies on the signal amplitude of the VZERO counters, that is correlated with the event multiplicity (HM_{VZERO}) as explained in Sec. II-B.iii.

As a side note, because the SDD is the slowest ITS detector ($4.3 \mu\text{s}$) compared to the others (300 ns for the SPD and 1.4 to $2.2 \mu\text{s}$ for the SSD), it acts as a bottleneck and limits significantly the triggering rate. For that reason, the trigger system operates in two modes: the default option, called “CENT”, corresponds to the one where events are recorded with the informations of the SDD. In the case when this detector is still in busy-state at the reception of the L0 signal, the “FAST” configuration allows nevertheless to record the event without reading out the SSD. In this way, by combining these two trigger configurations (CENT and FAST), one can double the amount of data available but at the price of a lower track reconstruction efficiency (Sec. II-D.ii).

The reception of a successful L2 trigger signal initiates the detectors readout. Each one produces *event fragments* that are transmitted to Data AcQuisition (DAQ) readout receiver cards, being themselves linked to Local Data Concentrators (LDCs). The latter gathers the event fragments from its associated cards and assembles them into sub-events. In parallel, a copy of the readout data is transferred to the High-Level Trigger (HLT) farm computer, that performs an online processing in order to filter out interesting physics events with more sophisticated and precise selections (jet identification, sharp p_{T} cut, etc) than the lower layer triggers (L0, L1, L2). It can also reduce the output size by selecting relevant parts of the event. The triggered event or the regions of interests are compressed, transferred back to the LDCs. The DAQ system treats the output of HLT system as the one of any other sub-detector.

A single machine of the Global Data Collector (GDC) farm²² receives the sub-events from sub-detectors’ LDCs — including the ones from the HLT computers — and proceeds to the event reconstruction. The Transient Data Storage archives the output data over the storage network before their final recording into the Permanent Data Storage.

²¹In fact, there exists still a few variants of the minimum-bias trigger such as at least a one hit in the SPD, or one hit in either VZERO scintillator arrays, or even both simultaneously.

²²The Event-Destination Manager (EDM) supervises the distribution of LDC’s sub-events from the same event to single GDC machines, and balances the data stream in order to avoid event loss by overloading the GDC farm (the so-called back-pressure). The latter point is critical for the reconstruction of rare events, as more frequent events take up most of the GDC load. Hence, the EDM monitors their GDC occupancy and, in case it is too high, they are blocked in favour of the rare events. With the past-future protections, these are the two cases that may lead to a rejection at the L2 trigger stage.

II-D The event reconstruction

The event reconstruction starts at the DAQ-LDC level, where the digitised signals of each detector, that have been likely generated by the same particle, are grouped into a *cluster* based on their space and/or time proximities. Its centre of gravity is often taken as an estimate for the crossing point of a particle in the sensitive volume of the detector.

II-D.i Preliminary determination of the primary vertex

From these clusters in the two innermost layers of the ITS, a preliminary estimation of the primary vertex position is realised [121]. The pairing of SPD clusters between the inner and outer layers (within an azimuthal window of $\Delta\phi = 0.01$ rad) allows to form tiny track segments²³ called *tracklets*. The space point towards which the maximum number of tracklets converges gives a first estimate of the primary vertex location.

Concretely, the reconstruction algorithm attempts to minimise the quantity

$$D^2 = \sum_i^N \left(\frac{x_i - x_0}{\sigma_{xi}} \right)^2 + \left(\frac{y_i - y_0}{\sigma_{yi}} \right)^2 + \left(\frac{z_i - z_0}{\sigma_{zi}} \right)^2, \quad (3.6)$$

with N the number of considered tracklets, and each term of the sum corresponds to weighted distance along x , y or z between the tracklet i (x_i, y_i, z_i)²⁴ and the interaction point (x_0, y_0, z_0). The minimisation procedure is repeated several times; at each iteration, the tracklets contributing to the previously found vertex are discarded from the sample. Hence, by construction, the first reconstructed vertex takes up the majority of tracklets and is designated as the primary vertex. Since the spatial resolution scales as $1/\sqrt{N_{\text{tracklets}}}$, the latter also turns out to be the most accurate.

In cases where no convergence point is found (as it happens in low-multiplicity events), the algorithm searches for a vertex along the beam axis, with the constraint that it coincides with the beam position in the transverse plane. It is calculated as the weighted mean of the intersection points with the beam axis over all the tracklet candidates.

If no pair of clusters can be formed in the SPD, the primary vertex and thus the event are not reconstructed.

II-D.ii Track reconstruction

The determination of the trajectory — or *tracking* in the particle physicist's jargon — of a charged particle breaks down into two major phases: the *track finding*

²³The track curling being supposedly small between the radii of the two SPD layers (3.9 and 7.6 cm), it can be approximated as a straight line, *most* particularly in the case of high-momentum particles [106].

²⁴Here, this is the tracklet's position at the point of minimum distance with respect to the primary vertex. At the start of the minimisation procedure, the initial location of the vertex is taken as the mean position of the intersection point of all selected tracklets [106].

and *track fitting*. The former aims at associating a set of clusters to the same track, and from this, the latter tries to estimate the track parameters such as the charge or momentum. Both can be performed using global or local methods.

Broadly speaking, the global approach treats all the measurements simultaneously, once all the informations have been collected. It has the advantages of being stable with respect to noise and directly applicable on raw data, but it does ~~a~~ require a precise knowledge of the model that may be unknown or do not exist because of random perturbations or non-uniformity of the magnetic field for instance. The online event reconstruction on the HLT computer farm typically uses such techniques (Cluster Finder and Track Follower methods, fast Hough transform), primarily because they are fast but also a high precision is not required at this stage (mostly interested in the reconstruction of high-momentum particles).

In contrast, the local methods proceed to a progressive estimation of the parameters from one measurement to the next, each step improving the knowledge about the trajectory. Thereby, they do not require to know the global model, as any local effect (stochastic processes, etc) can be naturally accounted for at each data point. However, they are sensitive to the noise, wrong measurement or misassociation, and rely on complex reconstruction algorithms. Among all the local approaches, the most advanced one is the Kalman filter technique, which is the one adopted for the offline reconstruction in ALICE.

Within the framework of the Kalman filter, the five track parameters at a given time (or equivalently, at the position of a given hit) are contained inside the *system state vector*. The latter evolves according to an iterative procedure in two steps.

- **Prediction:** The track parameters are extrapolated to the next detection plane as the sum of a deterministic term – depending only on the current knowledge of the state vector – and a noise term accounting for stochastic processes such as multiple scattering or energy loss.
- **Filtering:** If a cluster at the extrapolated position is found in the vicinity of the predicted measurement, it is added to the prediction, thus improving/updating the state vector. In this way, cluster association with a track (track finding) appears naturally and simultaneously with ~~the~~ track fitting.

These steps repeat as many times as there are measurement points. There also exists a third (optional) phase, called **smoothing**, available once the full state vector has been extracted: the prediction and filtering steps are replayed in the opposite direction, starting from the last filtered point. These can be reiterated as much as required; each pass refining the track parameters such that the reconstructed track reproduces more and more the real particle trajectory.

Note that the two aforementioned random perturbations of the particle trajectory are in fact treated differently²⁵. On one hand, the multiple scattering in-

²⁵This originates from the different stochastic nature of these processes. The multiple scattering follows a Gaussian distribution with a zero mean value and a variance given by the Molière theory [42]. In other words, the associated noise term should be unbiased ($\langle \epsilon \rangle = 0$) with a known covariance matrix. In contrast, the energy loss leads to a biased noise term ($\langle \epsilon \rangle \neq 0$), given by the Bethe-Bloch formula. However, it should be dominant for small particle energies where the covariance matrix is driven by the multiple scattering dominates. Hence no error term, associated to energy losses, is added to the covariance matrix [122].

troduces an angular uncertainty on the position of the next measurement, which translates into an increase of the covariance matrix elements of the state vector. On the other hand, the energy loss affects the momentum of track parameters, but can be estimated on average knowing the amount of crossed material and using the Bethe-Bloch formula in Eq. 3.1 under the assumption of a certain particle mass. Hence, a dE/dx correction of the track parameters can be applied at each prediction step.

In ALICE, the Kalman-filtering track reconstruction uses three passes, as illustrated in Fig. 3.13.

The first inward stage (first path on Fig. 3.13) starts by looking for the first clusters of a track candidate, dubbed *track seed*, in order to initiate the Kalman-filter procedure. This search commences in the best tracking device of the experiment, *i.e.* the TPC, and particularly at its outer radius where the low track density limits the number of ambiguous cluster association. At first, the seeds consist of two TPC clusters and the preliminary vertex point. This initial guess relies on the fact that the track originates from the interaction point. This process is reiterated later without such constraint, which would correspond to secondary tracks coming from a decay. In such case, the seeds are formed out of three clusters.

Once the seeds have been built, they are propagated inwards to the TPC inner radius. As described above, at each step, the seeds are updated with the nearest space point whenever one passes a proximity cut, taking into account multiple scatterings and energy losses. At the end, only the tracks with at least 20 (out of 159) attached clusters and with a minimum of 50% of the predicted measurement points matching an associated hit, are selected.

During this propagation, a preliminary particle identification based on the energy deposit in the TPC gas (see Sec. II-B.ii) allows to determine the most probable mass of the track candidate among eight hypothesis: e^\pm , μ^\pm , π^\pm , K^\pm , p^\pm , d^\pm , t^\pm , ${}^3\text{He}^{2\pm}$ or ${}^4\text{He}^{2\pm}$. In cases where there is an ambiguity, the pion mass is assigned by default. From this and the amount of crossed material at each step, energy losses can be corrected on average using the Bethe-Bloch formula (Eq. 3.1). It should be emphasised that all the parameters related to the TPC corresponds, in fact, to those of Ne. This approximation is justified by i) the fact that the TPC gas consists mainly of this element, and ii) the effect is relatively small.

When all the seeds have reached the inner wall of the TPC, the tracking in the ITS takes over. The reconstructed TPC tracks are extrapolated from the TPC inner wall (~ 85 cm) to the outermost layers of the ITS (SSDs at 38 and 43 cm) that serve as seeds for the track finding in the ITS. Similarly as in the TPC, the seeding procedure produces two kinds of seed: first, one with a vertex constraint, then the other without it. Whatever the hypothesis, they are all propagated as close as possible to the primary vertex, and updated along the way by any cluster passing a proximity cut. Only the highest quality candidates in the ITS from each TPC track are selected. A further check on cluster sharing among each other is performed. In such a case, the tracking algorithm tries to find another candidate and if this fails, the worst of the two tracks receives a special flag for containing a shared cluster that is potentially an incorrectly assigned cluster.

Once all the ITS-TPC tracks have been formed, the ITS standalone tracking

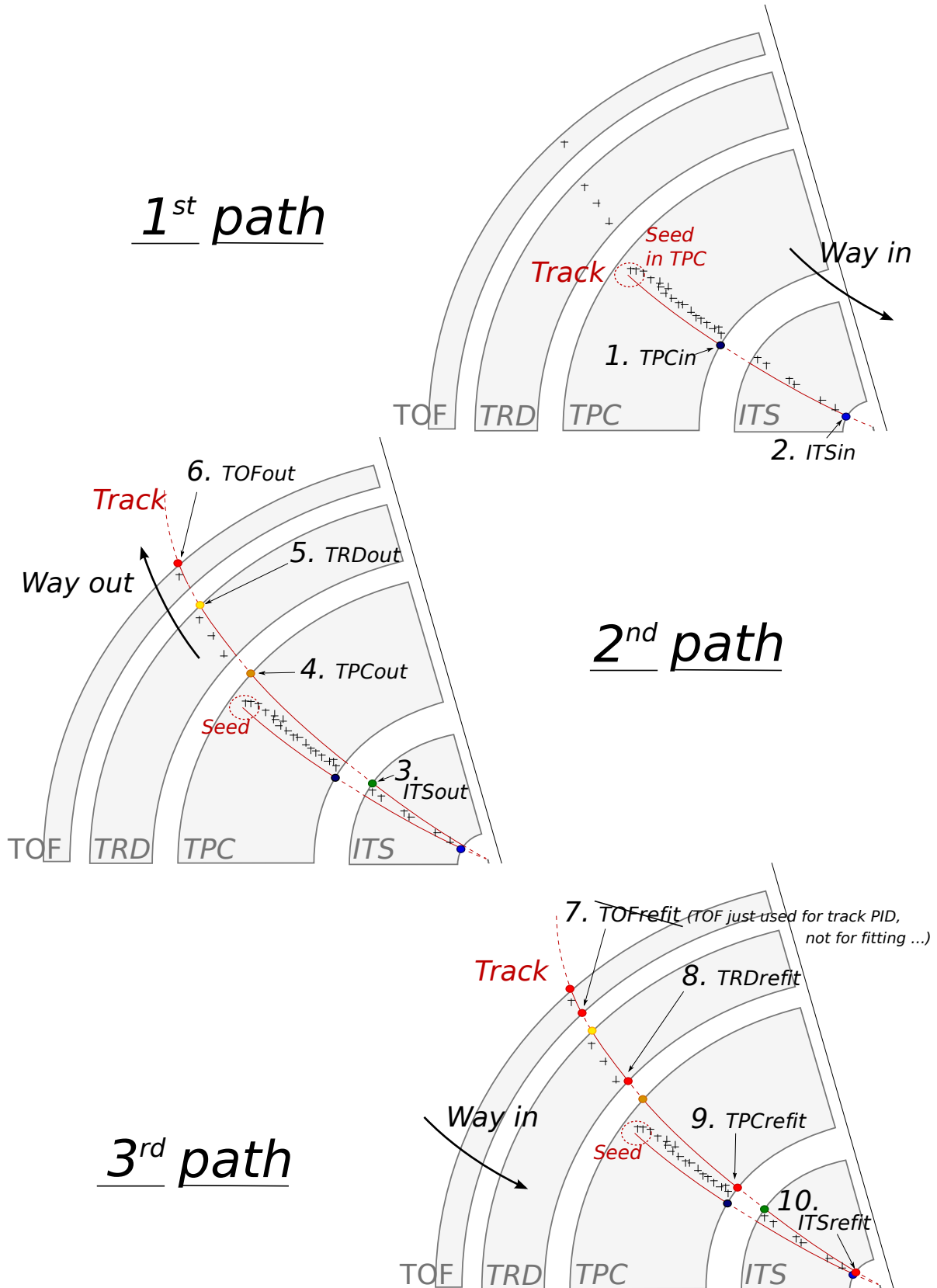


Fig. 3.13: Overview, at each pass of the Kalman filter, of the different elements related to the track reconstruction in ALICE. Figure taken from [123].

procedure comes into play and uses the remaining clusters to recover unfound tracks in the TPC because of i) their very low momentum or ii) the deadzones between sectors, or iii) decays before reaching the TPC. Formed out of two clusters from the three innermost layers and the preliminary vertex point, the seeds are propagated to the other layers, and updated with clusters passing a proximity cut. Only the track hypothesis with the smallest reduced χ^2 is kept, and its assigned clusters are removed from further track finding. The procedure repeats until there are no more track to search.

Upon completion of the track reconstruction in the ITS, the first stage of the tracking ends with the extrapolation of all tracks to their point of closest approach to the preliminary primary vertex. As in the TPC, energy loss corrections are applied at each propagation step in the ITS, considering the same mass hypothesis as one used previously and assuming that all the materials in the ITS volume (including the beam pipe) are made of Si²⁶.

The second stage starts with the outward refitting of the track parameters by the Kalman filter using the previously associated clusters. It is also during this second pass that the track length integral, as well as the expected time of flight for the eight particle mass hypothesis, are calculated; both quantities are updated at each step. The propagation procedure goes first from the primary interaction point to the outermost layers of the ITS, and then towards the TPC outer wall (second path on Fig. 3.13). When reaching the outer edge of the TPC, the Kalman filter stops updating the track parameters but the propagation continues in an attempt to match the track with a hit in a further detector (TRD, TOF, EMCal, PHOS, HMPID). The track length integration and time-of-flight calculation finish upon arriving at the TOF detector.

At the final stage (third path on Fig. 3.13), starting from the TPC outer wall, all tracks are propagated inwards to their distance of closest approach (DCA) to the preliminary primary vertex. Along the way, their parameters are improved one last time with the previously associated clusters in the ITS and TPC.

The reconstruction efficiency of TPC standalone tracks saturates around 80–85% for transverse momentum above 0.5 GeV/c, due to the loss of clusters in dead-zones between sectors. At lower p_T , it drops rapidly due to the preeminence of multiple scattering and energy loss in the detector material. Whatever the detector occupancy, the contamination of wrongly associated clusters in the TPC remains low; it does not exceed 3% for tracks with more than 10% of fake clusters, even in the most violent heavy-ion collisions.

The TPC track prolongation efficiency to the ITS depends mildly on transverse momentum. It reaches $\sim 95\%$ for tracks with at least two associated hits in the ITS, and decreases to about 80% in pp collisions at $\sqrt{s} = 7$ TeV (75% in Pb-Pb collisions at $\sqrt{s_{NN}} = 2.76$ TeV) when they have a minimum of one hit over two SPD layers, the furthest detectors relative to the TPC. The contamination of wrongly

²⁶This relies on the same arguments as those mentioned in the case of the TPC. The chap. 5 addresses the limits of this approximation.

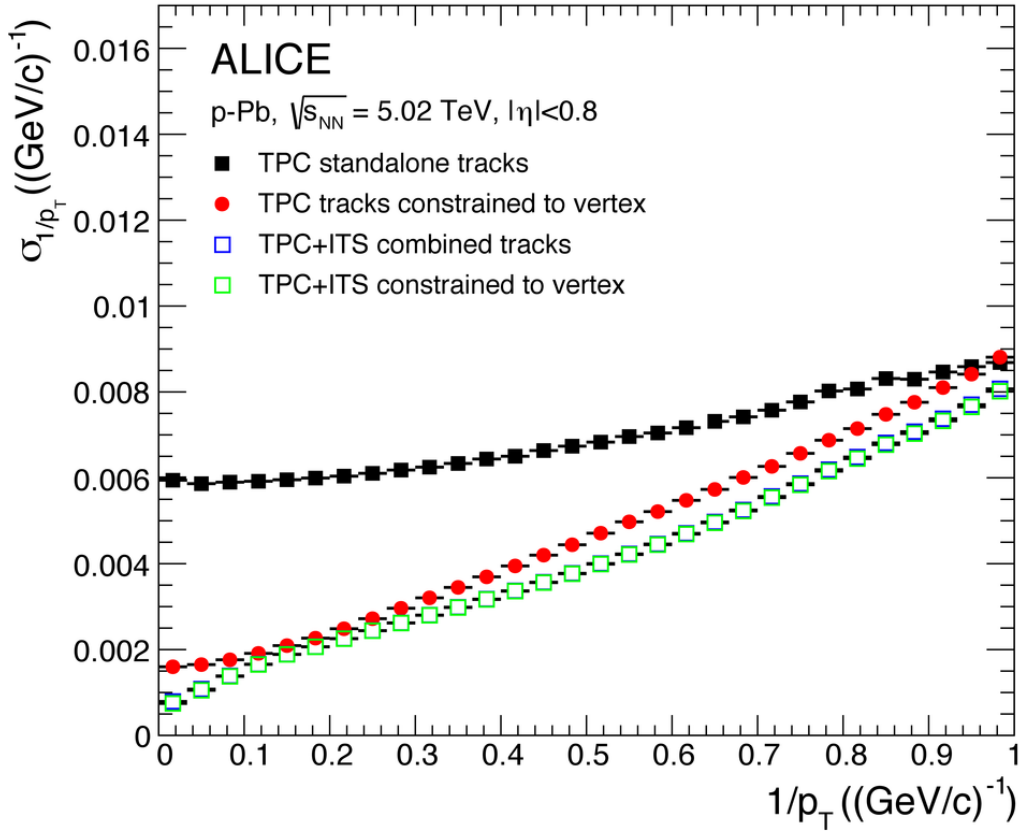


Fig. 3.14: Transverse momentum resolution for TPC standalone and ITS-TPC combined tracks, with and without vertex constraint, as a function of $1/p_T$ in p-Pb collisions at $\sqrt{s_{NN}} = 5.02 \text{ TeV}$. The blue squares can not be seen as they overlap with the green ones. Figure taken from [108].

associated ITS clusters, though, can be quite high: $\sim 30\%$ of tracks with at least one fake cluster below $p_T < 0.2 \text{ GeV}/c$, $\sim 7\%$ at $1 \text{ GeV}/c$, and below 2% at $10 \text{ GeV}/c$ in the most central Pb-Pb collisions.

The Fig. 3.14 shows the resolution on the inverse transverse momentum for TPC standalone and ITS-TPC combined tracks, extracted from their covariance matrix. This quantity is related to the relative transverse momentum resolution, σ_{p_T}/p_T , via

$$\sigma_{1/p_T} = \frac{\sigma_{p_T}}{p_T} \frac{1}{p_T} \quad \Rightarrow \quad \frac{\sigma_{1/p_T}}{1/p_T} = \frac{\sigma_{p_T}}{p_T}. \quad (3.7)$$

The transverse momentum resolution varies as a function of the transverse momentum; typically, it is at least as good as 0.9% at $p_T = 1 \text{ GeV}/c$ and 6% at $p_T = 10 \text{ GeV}/c$. Note that the global ITS-TPC tracks always yield to a better relative p_T resolution than those reconstructed only with the TPC. In the latter case, the vertex constraint on the seeding strongly improves the resolution but the effect is negligible with a matching to the ITS detectors.

II-D.iii Final determination of the primary vertex

The end of tracking stage opens the way towards a new determination of the primary vertex, based on the ITS-TPC combined tracks. Unlike the tracklets, their curvature is known, which allows to find the interaction point with a much higher precision.

All the global tracks are extrapolated as close as possible to the nominal beam position (or luminous region²⁷). After rejection of far outliers, the approximate point of closest approach of all selected tracks provides a first estimation of the interaction vertex. From here, in the near vicinity of its true position, a highly precise vertex fit can be performed [124]. It basically consists in finding the space point that minimises the weighted²⁸ distance of closest of approach to this same point over all the tracks, as in Eq. 3.6.

The precision on the vertex position increases with the number of tracks employed in the fitting algorithm. Therefore, in low-multiplicity events, the fit also includes the nominal beam position as an additional constraint/contribution with an uncertainty corresponding to the transverse size of the luminous region [124]. Although high-multiplicity events have plenty of tracks available, the high pile-up rate requires a different approach. In order to reduce the contamination from collisions, only tracks coming from the same bunch crossings (identified thanks to the timing information from the TOF detectors) can contribute to the same vertex. To further suppress the contribution of outliers, the vertex fitting relies on a more robust technique based on Tukey bisquare weights [108].

The Fig. 3.15 shows the transverse resolution on the primary vertex position as a function of the particle multiplicity per unit pseudo-rapidity in pp at $\sqrt{s} = 7$ TeV. As mentioned above, the accuracy on the interaction point position sharply improves with the track multiplicity in the event, reaching $\sim 50 \mu\text{m}$ for $dN/d\eta > 15$. With respect to the preliminary vertices found with the SPD tracklets, the final ones determined with global tracks are better by at least a factor of two. Note that both resolutions scale as the square root of the number of contributing tracks/tracklets [121].

II-E The ALICE offline framework

II-E.i The computing model

Over the whole LHC Run-2, more than 160 PB of raw data have been collected by the ALICE experiment. Their treatment requires a robust framework, capable of processing them in a reliable and timely fashion.

²⁷When two beams collide, it gives rise to one or multiple collisions. Their interaction point *a priori* lies anywhere within the region defined by the convolution of the particle distribution – in other words, the beam size – of the two incoming beams. Also called *interaction region*, its transverse size is given by $\sigma_D = \sigma^{\text{beam}}/\sqrt{2}$, with σ^{beam} the bunch size spread. [106].

²⁸The track weighting has the effect of suppressing the contribution of any remaining outliers.

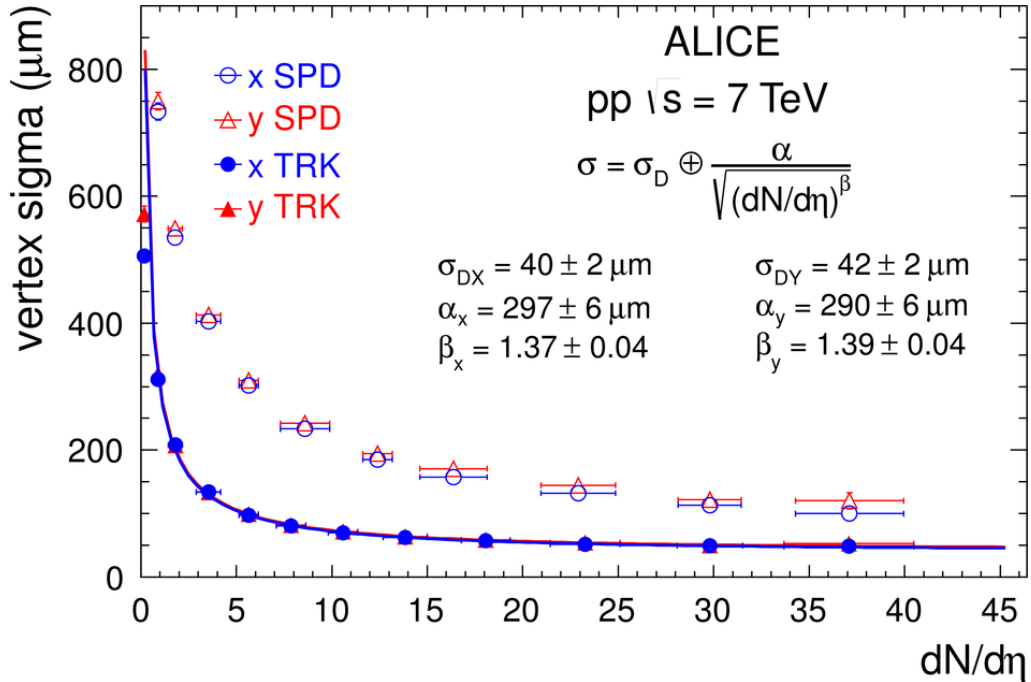


Fig. 3.15: Transverse width of the final vertex distribution, in solid markers, in pp collisions at $\sqrt{s} = 7 \text{ TeV}$. Two contributions are separated: the transverse size of the nominal beam position σ_D , and the transverse resolution on the vertex $\alpha/\sqrt{(dN/d\eta)^\beta}$. For comparison, the open markers show the same quantity determined making use of SPD tracklets. Figure taken from [108].

To be processed, this volume of data requires an amount of computing resources that can not be concentrated in one place²⁹. Instead, it is spread over different computing centres around the world. In particular, ALICE uses the Worldwide LHC Computing Grid (WLCG), a worldwide computer network infrastructure coordinated by the CERN and shared among all LHC experiments, that includes over 170 computing centres in 42 countries. The WLCG stands as the world's largest computing grid, that provides near real-time access to the LHC data regardless of their physical location [125].

The WLCG computing sites follows a hierarchical structure in layers or *Tiers* as shown in Fig. 3.16, that provides different levels of data storage and processing. The Tier-0 corresponds to the CERN Data Centre located in Geneva, that directly receives all the raw data from the LHC experiments, keeps one replica (on magnetic tapes) and performs the first reconstruction pass. It also distributes the raw data and the reconstruction output to the thirteen Tier-1 computer centres around the world via high-speed connections between 10 and 100 GB/s. They share the same roles with CERN, namely safe-keeping the data, finishing their reconstruction and distributing them to the next layer. The Tier-2 regroups about 160 sites, corresponding typically to universities and scientific institutes, that store the data produced by the closest Tier-1 site. Beyond their mass-storage capabilities, they

²⁹There are various reasons. Although the funding agencies invest in the computing equipment of their scientific projects, they focus their investments in their own countries. Even if all computing resources could be put in one place – let us say, at CERN –, the manpower would be insufficient to ensure the upkeep of such a system.

are used to run the physics analysis tasks, produce Monte Carlo simulations, and reprocess the data. A copy of the simulated data is stored in the Tier-1 centres.

Each site relies on four components: networking, hardware, middleware and physics analysis software. The networking – the backbone of any distributed computing infrastructure – allows to link together the hundreds of WLCG centres and exchange data with an excellent connectivity thanks to the CERN Internet Exchange Point, the high-bandwidth LHC optical-fibres and the Grid File Transfer Service. Each site can be seen as a computer farm that needs tending to; the hardware component refers to this aspect. It includes maintaining disk and tape servers, providing tools to access the data whatever the storage medium — via the CERN Advanced STORage system (CASTOR) or CERN EOS — as well as upgrading regularly the necessary software to operate the Grid system — from the operating system to the physics analysis software libraries. The middleware corresponds to the software architecture that comes between the operating systems and the physics analysis software; it provides numerous services (interfacing, workload management, monitoring, job submission and execution, etc) in order to access at the titanic CPU power and storage resources of the Grid. In ALICE, the AliEn system fills in this task. Last but not least, the physics analysis software provides the tools to analyse the data.

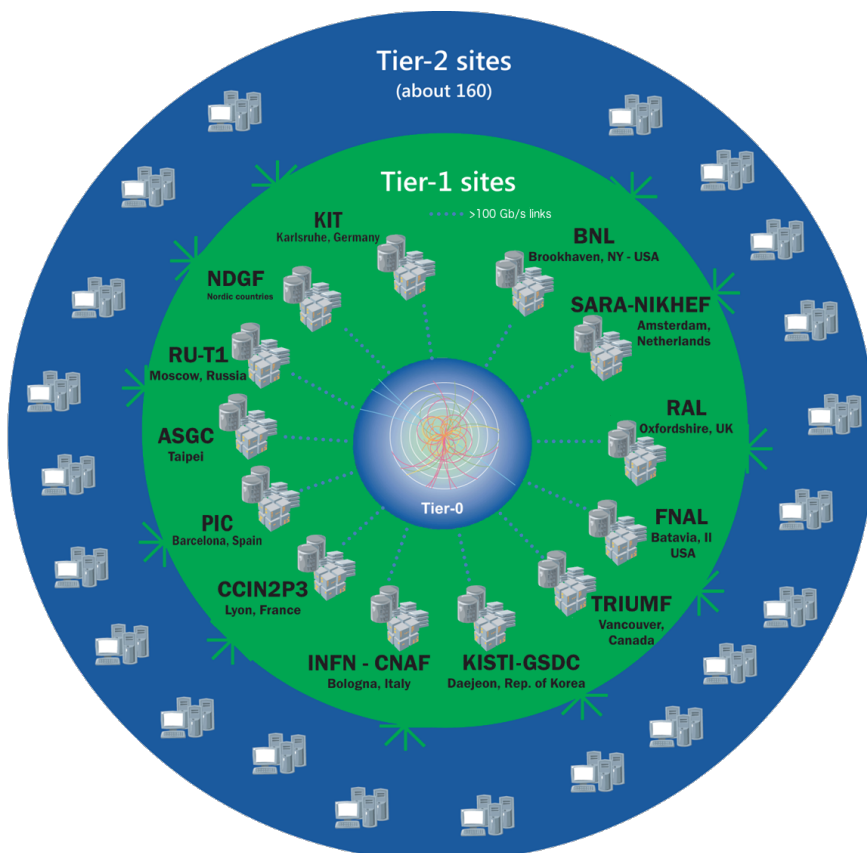


Fig. 3.16: The three Tiers of the Worldwide LHC Computing Grid as of 2023, with the list of the thirteen Tier-1 computing centres, with their geographic location. Figure taken from [125].

II-E.ii The analysis framework, AliRoot

As most of the current high-energy experiments – if not all –, the ALICE offline analysis framework is built upon ROOT, an high-performance object-oriented software developed by the CERN and implemented almost entirely in the C++ programming language. Created in 1994 by René Brun and Fons Rademakers, it provides the mathematical and statistical tools to manipulate large amounts of data and analyse them [126]. ROOT sets the foundations for the ALICE offline framework, that divides into two parts during the LHC Run-1 and Run-2:

AliRoot [127] contains the codes that are common to the whole collaboration. In particular, it includes:

- an interface for running Monte Carlo simulations (from the event generation to the detector response), event visualisation, etc,
- a description of the detector geometry as well as the material budget,
- the alignment and calibration of the detectors,
- the real and simulated data reconstruction,
- and the management of the data formats;

AliPhysics [128] regroups all the physics analysis tasks to process the collected and simulated events. Each PWG in Tab. 3.4 has a dedicated repository.

II-E.iii Data formats

Depending on the processing stage, the ALICE data come in three distinct formats with different levels of abstraction. At the output of the detectors (Sec. II-B), they take the form of *Raw Data*, that regroups all the cluster informations recorded during a collision. They are collected by the DAQ system before being transmitted at a rate of 200 MB/s to the Tier-0 site for storage and distribution to Tier-1 data centres.

In parallel, the raw data undergo their first reconstruction pass at CERN. For pp collisions, it typically takes two minutes per event in pp collisions, mainly in input/output streaming. This first pass yields to an Event Summary Data (ESD) format, that contains most of the informations related to the reconstruction such as the reconstructed tracks with their associated hits. While a pp event from raw data occupies about 1 MB of disk space, it reduces to ~ 100 kB in ESD format.

At the analysis level, the ESD file presents the advantage of having the full knowledge of the tracking and event building, with the possibility of replaying some part of the reconstruction like the V0 and cascade *vertexings* (see next chapter, Chap. 4). However, they are still considered as too heavy and too expensive in terms of CPU time. For that reason, the first pass also produces a file in Analysis Object Data (AOD) format, a lighter version than the ESD counterpart, keeping only the relevant information to extract the physics content from the data. It covers 5 to 10 times less disk space than an ESD file, thereby reducing significantly the processing time by the analysis tasks.

Note that the first reconstruction pass only serves to calibrate the TPC, SDD, TOF, T0, luminous region and centrality. The second pass applies the derived calibration, and is then used to improve the calibrations and perform a first data quality assurance. These two reconstruction passes, using only a fraction of the data from each run, provides the input for a more complete and fine-tuned calibration, that is stored in the Offline Conditions DataBase³⁰ (OCDB) and is applied in the third pass. At each stage of the processing, a set of ESD and AOD files is produced.

II-E.iv Monte Carlo data

As mentionned in Sec. II-E.ii, the AliRoot framework has the capability to run Monte Carlo (MC) simulations, that try to reproduce as accurately as possible the stochastic processes observed in the detector by sampling a given set of probability density distributions. Such a simulation consists in two consecutive steps.

It starts with the generation of the event, that simulates a collision as well as the associated physics processes ultimately leading to the creation of primary particles. This first step relies on different models called *event generators*, each having its own paradigm, its own production mechanisms, tuned to mimic the topology the collision (multiplicity, momentum distribution, etc). Among the most commonly used, there are PYTHIA [130] and HERWIG++ [131] for pp collisions, EPOS [132] for both pp and heavy-ion collisions, HIJING [133] exclusively for heavy-ion collisions.

After the generation of the event comes the propagation of the primary particles through the ALICE detector. This requires a modelisation of the apparatus in its entirety, from the various elements composing the sub-detectors to their geometric shape and their positioning. It also has to account for noisy or dead channels, detector defects, intensity of the magnetic field, etc. These informations available run by run on OCDB are used to *anchor* the simulation on the actual data taking conditions. The transport and interaction with the detector material typically rely on dedicated softwares, such as GEANT3 [134], GEANT4 [135] and FLUKA [136].

Taking into account the detector response, the energy deposited by the passage of charged particles are converted into digits and then stored in raw data format. From this point, the reconstruction of the event can start. It follows the same procedure as the one applied for real data (Sec. II-D), yielding to files in ESD and AOD formats.

In order to minimise the disk space usage and the computing time, only a fraction of the total number of events in real data is simulated. The proportion of triggers remains unchanged between real and simulated data, though. For instance, if a run in its entirety has 10% of high-multiplicity events, its simulated twin will comprise the same fraction of such events.

The key point of MC data resides in the presence of the full information about the event. This is often referred as *MC truth*. Each element of the simulation is perfectly known: the number of generated particles, their type, charge, momenta,

³⁰In fact, OCDB stores the ideal geometry of the detector, the alignment objects (*i.e.* corrections on the ideal geometry derived using Millepede algorithm [129]) and the calibration parameters for each data taking period.

whether they are primary or secondary, where they deposit energy in the detector giving rise to hits – the so-called track references –, etc. This copious amount of additional informations opens the way towards specific kinds of investigations.

When designing a new experiment, it allows to anticipate the results and, if needed, to correct or optimise the current design. It gives also the opportunity to estimate the performances of a detector (typically, the efficiency) and to study its systematic features. Finally, the comparison between the measurements (real data) and the predictions from a given MC model (simulated data) helps to improve our understanding of the underlying physics.

It should be mentionned that there exists two classes of MC simulations in high-energy physics. Reproducing as accurately as possible a collision requires tuning the parameters of the simulation such that they correspond to the ones observed in real data, including the decay channels, the branching ratios, etc. This is the standard type of simulations, the *general-purpose* MC production. A limitation arises when dealing with rare signals: for them to be observed, an unrealistic amount of events would need to be generated.

Instead, one could resort to an *enriched* MC simulations, in which the abundance of rare signals is increased. This can be achieved by artificially injecting the particles of interest in the simulation, according to a flat distribution in p_T or rapidity, etc. Another option consists in embedding a pure sample of rare signals into a background event, coming from either a simulation or real data. This is particularly used in p-Pb or Pb-Pb simulations, where PYTHIA – a generator dedicated to pp collisions – produces an event with an enhanced abundance in rare signals. However, the topology of the simulated event does not coincide with the one in p-Pb or Pb-Pb collisions. Therefore, the injected event is incorporated into a HIJING event, that plays the role of a background event³¹.

³¹Note that the background event can *a priori* be re-used several times.

Chapter

4 | Identification of V0 particles and cascades

The Chap. 2 and 3 have set the scene, it is time for the main actors to come onto stage, that are the (multi-)strange baryons or more precisely, the *hyperons*. These consist of any baryon containing at least one strange quark, but no heavier quarks such as charm, bottom or top. By describing their identification and the physics interests surrounding their reconstruction, this short chapter lays the foundations for the analysis performed throughout this thesis.

The first section, Sec. I, underlines the appealing features of strangeness and, particularly, (multi-)strange particles. The hyperons of interest in the present analyses are specified in the following section, Sec. II, as well as the motivations for this choice. This part also presents the principles for multi-strange baryon identification via topological reconstruction. Finally, in connection with Chap. 3, this short chapter closes on what makes ALICE an unique experiment for studying strange hadrons.

I The appealing features of strangeness

I-A The strange quark with respect to the other flavours

Similarly as for the charm, bottom and top quarks, there is no strangeness among the valence quarks of the nucleons from the collision beams. These only consist in up and down quarks; other flavours can still be found inside the sea of quarks and gluons, but in a moderate amount with respect to those produced during a collision at the LHC energies. From this, there arises an interesting and straightforward aspect of strangeness: all the strange quarks observed in the final state hadrons must have been produced in the processes that have occurred during

the collision.

Another property regards the mass of the strange quark. One way of classifying quarks is based on whether they preserve (at least, approximatively) or break the chiral symmetry (Sec. I-C.ii): the up and down quarks belongs to the first kind and makes part of the light flavour sector. Those breaking the chiral symmetry – the charm, bottom and top quarks – constitute the heavy flavour sector. For comparison, the bare mass of the up quark sits at $2.16^{+0.49}_{-0.26}$ MeV/c², the down quark at $4.67^{+0.48}_{-0.17}$ MeV/c². In contrast, the one of the charm, bottom and top quarks lie around 1.27 ± 0.02 GeV/c², $4.18^{+0.03}_{-0.02}$ GeV/c² and 172.69 ± 0.30 GeV/c² respectively [42]. From this perspective, the strange quark with its bare mass of $93.4^{+8.6}_{-3.4}$ MeV holds an unique position: its lightweight makes it relatively inexpensive (in terms of energy) to produce; being still much heavier than the up and down quarks (by one order of magnitude), this also qualifies it as non-ordinary matter. Thus viewed as both light and heavy, the strange quark gives access to an abundant source of non-ordinary matter.

I-B The specificity of strange hadrons

Most of strange hadrons decays into charged particles in their dominant channel. In addition, they also have a relatively long lifetime, allowing them to fly over several centimeters before the decay. From these two elements stem the distinctive decay topology of strange particles known as V0 or cascade (Sec. II-A), that can be used in their reconstruction by associating the different daughter tracks to reform the decay vertex (topological reconstruction, detailed later in Sec. II-B) [137]. This characteristic turns to be particularly interesting as the latter provides a robust identification of strange hadrons over a wide momentum range, from low to high p_{T} .

Consequently, this offers the possibility for a continuous study of strange hadrons over different production regimes, involving soft, intermediary and hard processes such as multi-parton interactions, quark coalescence and jet fragmentation respectively. For that reason, strange particles represents prime choice probes to investigate and thus improve our understanding on the evolution of the hadronisation mechanisms¹ with momentum.

II The multi-strange baryon identification

Among all the strange hadrons, this work focuses on the strangest baryons, containing two or three strange quarks, the so-called multi-strange baryons. Excluding the associated resonances, this leaves five particles: three containing two strange quarks – the $\Xi^0(uss)$, $\Xi^-(dss)$ and $\bar{\Xi}^+(\bar{d}\bar{s}\bar{s})$ –, and two triple-strange hadrons namely the $\Omega^-(sss)$ and $\bar{\Omega}^+(\bar{s}\bar{s}\bar{s})$.

¹To be exact, it is not the hadronisation mechanisms that evolves with the transverse momentum but rather their relative weight. For instance, soft processes dominates at low p_{T} , and hard ones at high p_{T} . However, *a priori*, there are also soft processes at high momentum – conversely hard processes at low momentum –, although they represent only a small fraction.

Particle	Strangeness	Mass (MeV/c ²)	Lifetime (cm)	Decay channel	B.R.
Λ [uds]	+1	1115.683	7.89	p [uud] $\pi^-[\bar{u}\bar{d}]$	63.9 %
$\bar{\Lambda}$ [$\bar{u}\bar{d}\bar{s}$]	-1	1115.683	7.89	$\bar{p}[\bar{u}\bar{u}\bar{d}]$ $\pi^+[\bar{u}\bar{d}]$	63.9 %
Ξ^0 [uss]	+2	1314.86	8.71	Λ [uds] $\pi^0[u\bar{u}]$	99.6 %
Ξ^- [dss]	+2	1321.71	4.91	Λ [uds] $\pi^-[\bar{u}\bar{d}]$	99.9 %
$\bar{\Xi}^+$ [$\bar{d}\bar{s}\bar{s}$]	-2	1321.71	4.91	$\bar{\Lambda}$ [$\bar{u}\bar{d}\bar{s}$] $\pi^+[\bar{u}\bar{d}]$	99.9 %
Ω^- [sss]	+3	1672.45	2.461	Λ [uds] $K^-[\bar{d}\bar{s}]$	67.8 %
$\bar{\Omega}^+$ [$\bar{s}\bar{s}\bar{s}$]	-3	1672.45	2.461	$\bar{\Lambda}$ [$\bar{u}\bar{d}\bar{s}$] $K^+[u\bar{s}]$	67.8 %

Table 4.1: Main characteristics of the Λ and the charged multi-strange baryons: quark content, strangeness, tabulated mass and lifetime ($c.\tau$), dominant decay channel with the associated branching ratio (B.R.) [42].

The Tab. 4.1 shows some characteristics of these five baryons, including their dominant decay channel, as well as the mono-strange baryon Λ since it appears in all decay channels. Unlike the Ξ^0 , the four charged multi-strange baryons share a common feature and a particularly appealing one: in their dominant decay channel, they follow a cascade decay topology as detailed in the next section, Sec. II-A. For that reason, the present work concentrates on the study of charged multi-strange baryons.

From now on, the following notation will be used. The Ξ^\pm (or $\bar{\Xi}^\pm$) refers to Ξ^- or Ξ^+ (or Ω^- or $\bar{\Omega}^+$). Conversely, Ξ (or Ω) means Ξ^- and Ξ^+ (or Ω^- and $\bar{\Omega}^+$). The same goes for other particles. Moreover, unless indicated otherwise, the term multi-strange baryon now designates only the Ξ^- , Ξ^+ , Ω^- or $\bar{\Omega}^+$.

II-A The V0 and cascade decays

The Fig. 4.1 depicts the full cascade decay chain of Ξ and Ω . After flying over a few centimeters, the multi-strange baryon decays weakly into a charged pion (or kaon for the Ω) and a Λ . The latter being electrically neutral, only the charged meson deposits energy in the different sensitive layers and thus can be detected at this stage; the meson plays the role of a *bachelor* particle.

The two decay products continue to travel through the detector, until the baryon daughter decays² at 63.9% via weak interaction into two oppositely charged particles: a proton and a pion. Depending on their electric charge, one is called the *positive* particle and the other the *negative* particle. This decay topology is known as V0³. Furthermore, the term “cascade” refers to the two-steps decay process un-

²The bachelor daughter being either a π^\pm or K^\pm , in most cases it does not decay in the detector due to their long lifetime ($c.\tau_\pi = 7.8045$ m and $c.\tau_K = 3.711$ m). For those that actually decays in the detector, they are characterised by *kink* topology due to their decay into a charged particle and a neutral particle.

³The term “V0” comes from the V-shape decay topology formed by the two oppositely charged

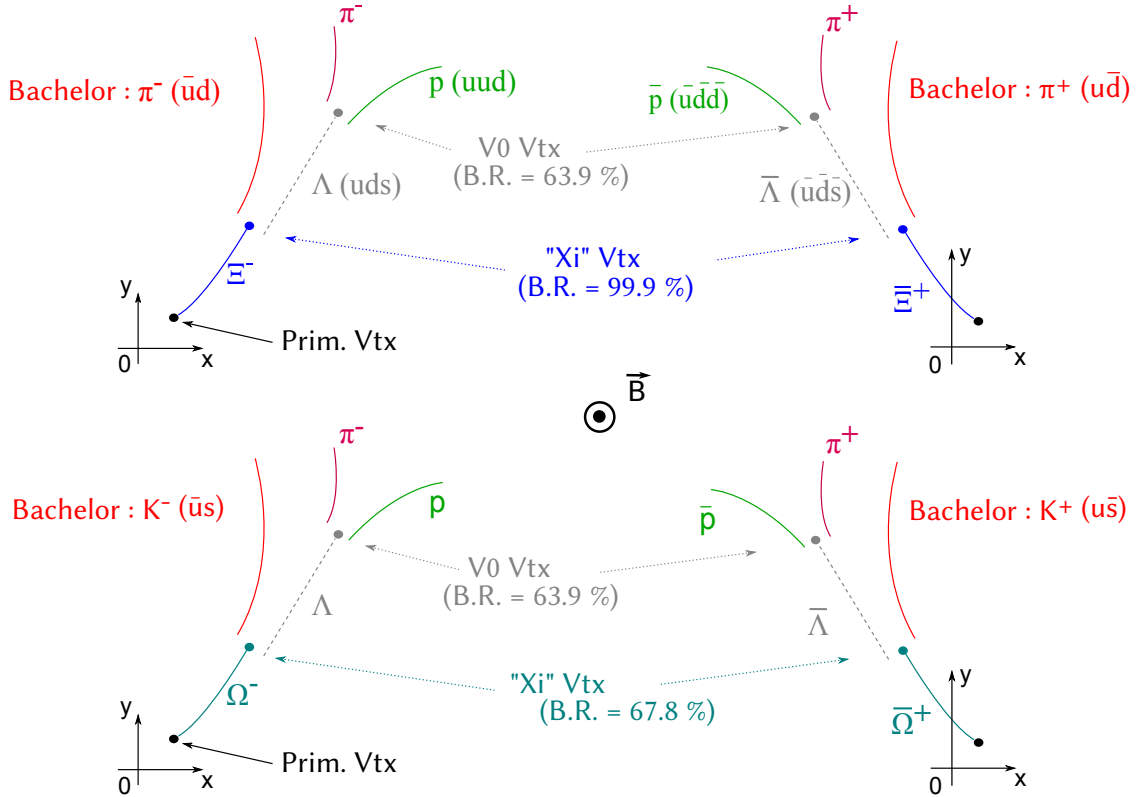


Fig. 4.1: Depiction of the full cascade decay chain of the Ξ^- (top left), Ξ^+ (top right), Ω^- (bottom left) and Ω^+ (bottom right). Figure taken from [138].

dergone by the multi-strange baryons. Hence, in the following, the usage of the term *cascade* may be used to mention either the Ξ or Ω , and similarly the term *V0* for the Λ .

Note that the four cascades on Fig. 4.1 differ only in the nature of the particles involved. On one hand, from the left to right side, the particles are swapped to anti-particles. On the other hand, the larger strangeness content of the Ω imposes the presence of a bachelor particle containing a strange quark (kaon) while, in the Ξ case, it consists in an light unflavoured meson (pion).

It should also be mentioned that although the Ξ^\pm decays into this channel quasi-systematically (99.9%), this is only the case for 67.8% of the Ω^\pm .

The Fig. 4.2 shows the cascade decay of a Ξ^- within the ALICE detector. To make it more apparent, the surrounding tracks have been removed in the bottom left part. The Ξ^\pm or Ω^\pm being electrically charged, they may loose energy in the detectors and can *a priori* be detected as any other charged particle. Although they can fly over relatively long distance compared to the vast majority of unstable particles, their $c\tau$ remain too short to *systematically* reach the innermost detectors at about 3.9 cm and 7.6 cm (to be compared to $c\tau_\Xi = 4.91$ cm and $c\tau_\Omega = 2.461$ cm)⁴. Moreover, the Λ is a neutral particle, hence it can not deposit energy in the

decay daughters.

⁴Note that the detection and tracking of these two multi-strange baryons become possible with the upgraded version of the ITS in the LHC Run-3; the innermost silicon pixel detectors being positioned at a radius of 2.2 cm and 3.9 cm in the LHC, the Ξ and Ω have significantly more

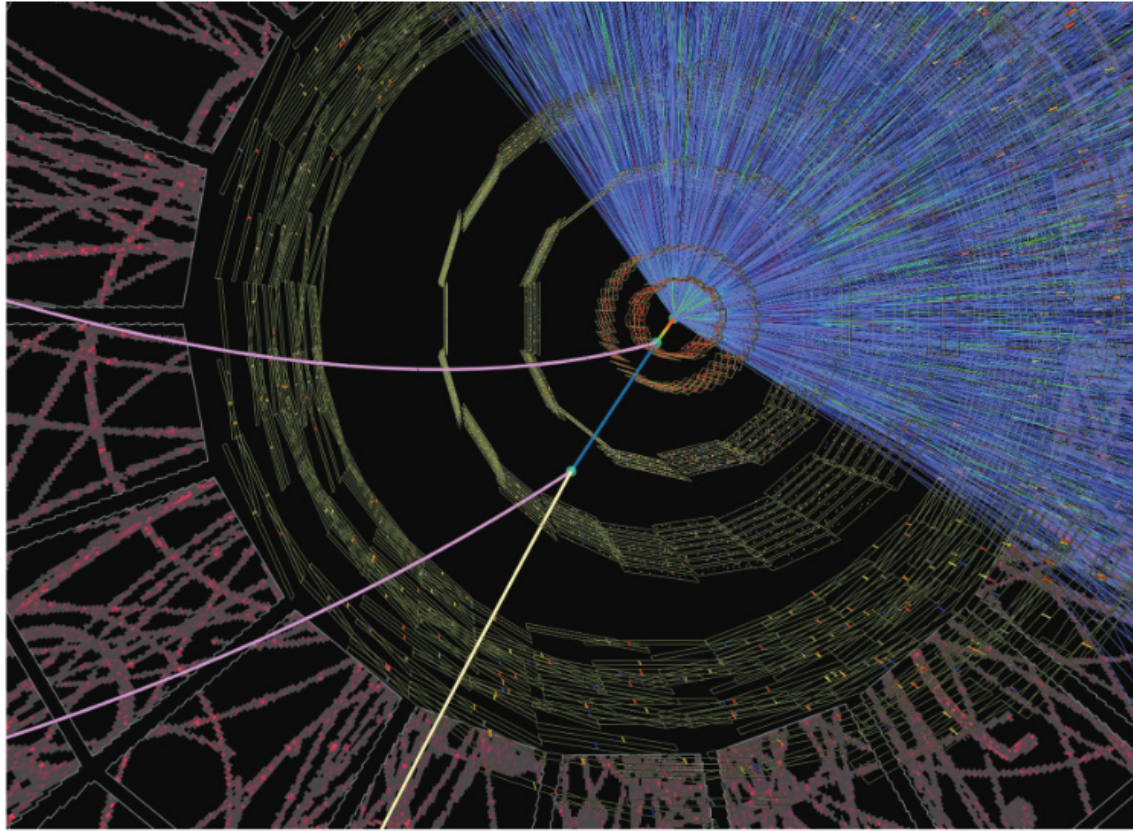


Fig. 4.2: Event display of a simulated Pb-Pb collision in the ALICE detector, with a close up on the ITS. The top part illustrates the typical density of tracks in such environment. The bottom part highlights the cascade decay of a Ξ^- . Figure taken from [107].

sensitive layers. In summary, only the bachelor, the positive and negative particles can be detected⁵. Therefore, it follows that the V0 and cascade have to be identified indirectly via their decay topology.

The top right part of Fig. 4.2 puts into perspective the difficulty of the reconstructing such a cascade topology. While the bottom part of the figure shows clearly the Ξ^- decay chain, it actually is immersed in a dense environment. In order to identify the multi-strange baryons in the event, the strategy followed in the present work consists in using topological reconstruction.

II-B The principles of the topological reconstruction

The cascade reconstruction is achieved by combining three tracks in the event. The association of two tracks allows to build a Λ (or $\bar{\Lambda}$) candidate, that may in turn be associated to another track (the bachelor) to form a cascade candidate. In a pp collision, the charged particle density⁶ can vary from a few particles up to fifty, and more than a thousands in the most central heavy-ion collisions. The

chances to leave hits in this detection layers, and therefore to be detected [139].

⁵Due to their long lifetime, the detection of the π^\pm , K^\pm , p and \bar{p} relies on the reconstruction and identification of their associated tracks in the ITS and TPC.

⁶per unit of pseudo-rapidity

mere association of three tracks leads inexorably to the formation of erroneous candidates, thus constituting a source of *combinatorial* background. In order to suppress the latter, geometric selections – aimed at singling out the candidates spatially compatible with the expected decay topology – are introduced; this is the general principle behind topological reconstruction.

II-B.i Formation of the V0 candidates

The reconstruction starts with the formation a V0 candidate. The first step consists in identifying *secondary* tracks, that do not originate from the interaction point. They are tagged as such, if the distance of closest approach (DCA) between the considered track and the primary vertex exceeds a critical value⁷ (Fig. 4.3, V0.a).

The second step aims at forming pairs of secondary tracks of opposite charge – characterised by different curvatures –; by imposing that the DCA between the two tracks is small, only the pairs originating potentially from the same decay point are retained. The secondary vertex is then positioned on the segment defined by the previous DCA, weighted by the quality of the tracks (Fig. 4.3, V0.b).

The two daughter tracks are then propagated from their initial position (the point of closest approach to the primary vertex, Sec. II-D.ii) to the secondary decay point⁸. This allows to calculate all the kinematic quantities of the V0, among which its momentum; the latter being equal to the momentum sum of the positive and negative particles at the secondary vertex, due to momentum conservation.

II-B.ii The reconstruction of cascade candidates

From the sample of V0 candidates (Sec. II-B.i), only those compatible with a Ξ^\pm or Ω^\pm decay are considered. In other words, the reconstruction of a cascade candidate must necessarily go through a secondary V0 that corresponds to either a Λ or $\bar{\Lambda}$.

Primary and secondary V0s are separated resorting to the pointing direction in the lab frame, given by the momentum at the decay vertex. This direction coincides with the straight-line trajectory of the candidate⁹ and allows to estimate its DCA to the interaction point (Fig. 4.3, V0.c). The latter being close to zero for primary V0s, a lower cut on this variable enables their rejection to retain only those tagged as secondary.

The identification of the V0 goes through the calculation of the invariant mass under the Λ or $\bar{\Lambda}$ hypothesis. This boils down to making an assumption on the mass of each decay daughter. In the case of a Λ , the positive track corresponds to

⁷While one expects for a primary track to have a DCA to the primary vertex equal (or close) to zero, this is the opposite for a secondary track: since it does not originate from the collision point, its DCA to the interaction vertex must necessarily be different from zero.

⁸Most importantly, here the propagation is performed without taking the energy losses into account. This point will be addressed in chap. 5

⁹If the candidate corresponds to an actual Λ or $\bar{\Lambda}$ (electrically neutral), its trajectory, not being curved under the influence of the magnetic field, must necessarily follow a straight line.

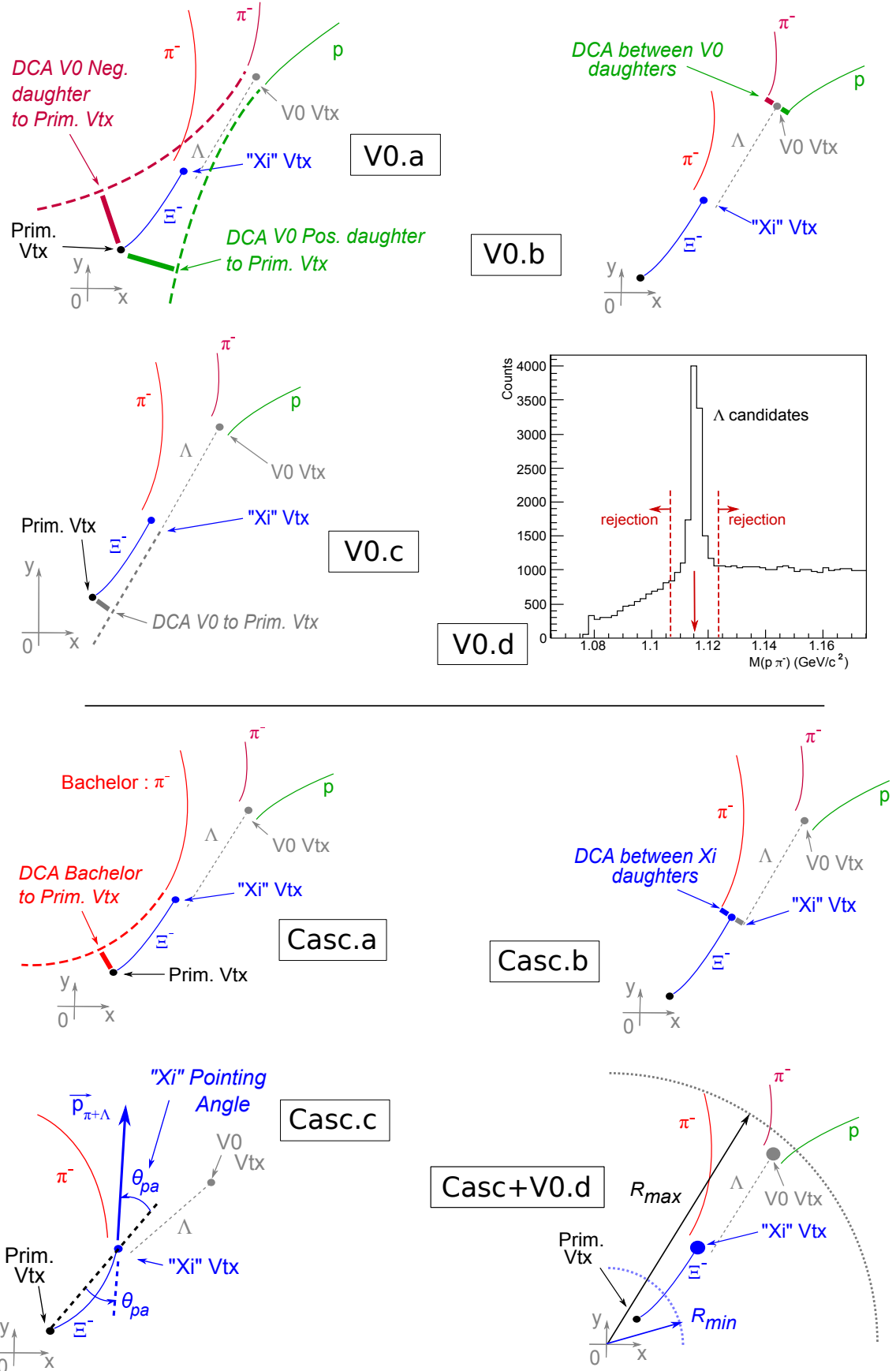


Fig. 4.3: Schematic representation of the different topological selections applied in order to first reconstruct V0s (top part), and then cascades (bottom part). Figure taken from [140].

a proton, the negative to a π^- (Eq. 4.3); conversely, for a $\bar{\Lambda}$, they are considered as a π^+ and an anti-proton respectively. If it turns out that the candidate is, in fact, a true Λ or $\bar{\Lambda}$, the reconstructed mass should lie within a window of typically a few MeV/c^2 ¹⁰ (Fig. 4.3, V0.d), centred around the nominal mass of the Λ ($m_\Lambda = 1.115683 \text{ GeV}/c^2$). In most cases, only one of the two mass hypothesis passes the cut¹¹, making it possible to differentiate between a Λ and a $\bar{\Lambda}$.

$$M_{\text{candidate}}^2(\Lambda) = (E_{\text{pos.}} + E_{\text{neg.}})^2 - (\vec{p}_{\text{pos.}} + \vec{p}_{\text{neg.}})^2 \quad (4.1)$$

$$= \left(\sqrt{\vec{p}_{\text{pos.}}^2 + m_{\text{pos.}}^2} + \sqrt{\vec{p}_{\text{neg.}}^2 + m_{\text{neg.}}^2} \right)^2 - (\vec{p}_{\text{pos.}} + \vec{p}_{\text{neg.}})^2 \quad (4.2)$$

$$= \left(\sqrt{\vec{p}_{\text{pos.}}^2 + m_{p^+}^2} + \sqrt{\vec{p}_{\text{neg.}}^2 + m_{\pi^-}^2} \right)^2 - (\vec{p}_{\text{pos.}} + \vec{p}_{\text{neg.}})^2 \quad (4.3)$$

A last step consists in forming a cascade candidate via the association of a candidate Λ (or $\bar{\Lambda}$) with any track labelled as secondary¹² (Fig. 4.3, Casc.a), playing the role of the bachelor particle. The procedure is analogous to what was done to build a V0 candidate: only pairs with a sufficiently small DCA between the reconstructed Λ (or $\bar{\Lambda}$) and the bachelor are considered (Fig. 4.3, Casc.b); primary cascades are set apart from secondary ones by introducing the *pointing angle*. The latter corresponds to the angle defined by the direction of propagation (or pointing direction) of the candidate, and the line joining the primary and secondary vertices. This angle should be small for a primary candidate and, even though the magnetic field is bending their trajectory, the change in direction remains moderate. This selection usually goes through the cosine of the pointing angle, that is constrained to be close to unity in order to validate the cascade as primary (Fig. 4.3, Casc.c).

The V0 candidate is subject to the same cut. Due to its large mass compared to the one of the bachelor, the reconstructed Λ (or $\bar{\Lambda}$) takes up most of the cascade momentum, and so most of the pointing direction. As a consequence, in order to ensure that the V0 actually originates from a Ξ^\pm or Ω^\pm decay, the cosine of its pointing angle has to be close to unity.

As a final topological selection, the cascade and V0 decay vertices must lie within a certain confidence area, in the transverse plane (Fig. 4.3, Casc.d). Close to the interaction point, at small radii, the combinatorial background is overwhelming due to the high density of tracks. Conversely, at large distance, the probability of finding a Ξ^\pm or Ω^\pm becomes extremely low. For comparison, the inner wall of the TPC ($\sim 85 \text{ cm}$) lie at $\sim 18 c.\tau_\Xi$ and $\sim 35 c.\tau_\Omega$. At such distance, the Ξ^\pm and Ω^\pm survival probabilities are about 2% and 0.001%¹³ respectively. Therefore, the decay vertices of both cascade and V0 must be located beyond a radius deemed critical; those decaying too far away with respect to their lifetime are rejected¹⁴.

¹⁰The width of the mass window depends directly on the ALICE performances in terms of transverse momentum resolution on the reconstructed tracks.

¹¹The misidentification of the daughter particles usually results in a quite different invariant mass.

¹²With the exception of the V0 daughters tracks.

¹³Considering a high-momentum cascade of $5 \text{ GeV}/c$.

¹⁴Notice that one consists in a selection on the radial position of the decay vertices, the other a cut on their 3D location.

II-B.iii Invariant mass of the cascade candidates

At this stage, the topological reconstruction is over; each triplet of tracks forms a cascade candidate, that can correspond to a Ξ^\pm , a $\bar{\Omega}^\pm$ or some residual background. The distinction is made based on the invariant mass of each candidate (Eq. 4.5).

$$M_{\text{candidate}}^2(\text{casc.}) = (E_{V0} + E_{\text{bach.}})^2 - (\vec{p}_{V0} + \vec{p}_{\text{bach.}})^2 \quad (4.4)$$

$$= \left(\sqrt{\vec{p}_{V0}^2 + m_\Lambda^2} + \sqrt{\vec{p}_{\text{bach.}}^2 + m_{\text{bach.}}^2} \right)^2 - (\vec{p}_{V0} + \vec{p}_{\text{bach.}})^2 \quad (4.5)$$

$$M_{\text{candidate}}^2(\Xi^\pm) = \left(\sqrt{\vec{p}_{V0}^2 + m_\Lambda^2} + \sqrt{\vec{p}_{\text{bach.}}^2 + m_{\pi^\pm}^2} \right)^2 - (\vec{p}_{V0} + \vec{p}_{\text{bach.}})^2 \quad (4.6)$$

$$M_{\text{candidate}}^2(\bar{\Omega}^\pm) = \left(\sqrt{\vec{p}_{V0}^2 + m_{\bar{\Lambda}}^2} + \sqrt{\vec{p}_{\text{bach.}}^2 + m_{K^\pm}^2} \right)^2 - (\vec{p}_{V0} + \vec{p}_{\text{bach.}})^2 \quad (4.7)$$

For each association of three particles, two invariant masses are calculated: one under the hypothesis of a Ξ^\pm candidate (Eq. 4.6), the other for a $\bar{\Omega}^\pm$ candidate (Eq. 4.7). Notice that, contrarily to the Λ and $\bar{\Lambda}$ cases, the invariant mass is the same for the particle (Ξ^- , Ω^-) and the anti-particle (Ξ^+ , $\bar{\Omega}^+$). In addition, the masses of the daughter particles involved in Eq. 4.6 and 4.7 correspond, in fact, to the nominal values from the PDG [42]; most importantly, the reconstructed mass of the V0 is not being used here. As long as the latter has been identified as a Λ (*i.e.* its mass fits into a certain tolerance window, Sec. II-B.ii), this choice has the advantage of limiting the deterioration on the cascade invariant mass resolution.

Although the invariant mass allows to distinguish a Ξ^\pm from a $\bar{\Omega}^\pm$, there exists a region where this is not possible anymore. The Fig. 4.4 shows the invariant mass distribution of cascade candidates assuming a Ω^- as a function of the same candidate under the hypothesis of a Ξ^- . There are two discernible and perpendicular mass bands, each one corresponding to true population of one of two considered species. At their intersection, the two species become indistinguishables, which results in an increased background in this region: a candidate identified as Ξ^- may, in fact, reveal to be a Ω^- , and vice-versa.

This additional background impacts each kind of cascade in different proportions, though. Since the population of true Ξ^- is much larger than the one of Ω^- ¹⁵, the latter constitutes a marginal source of background with respect to the Ξ^- . Conversely, the true Ξ^- – particularly in the low mass region – represent a considerable source of background for the Ω^- . As a consequence, in the context of the reconstruction of $\bar{\Omega}^\pm$ baryons, any candidates also identified as a Ξ^\pm – that is, with an invariant mass under the assumption of a Ξ^\pm within a window of few MeV/c² around $m_{\text{PDG}}(\Xi)$ – are rejected.

¹⁵That is because the Ξ are typically ten times more produced than the Ω [141].

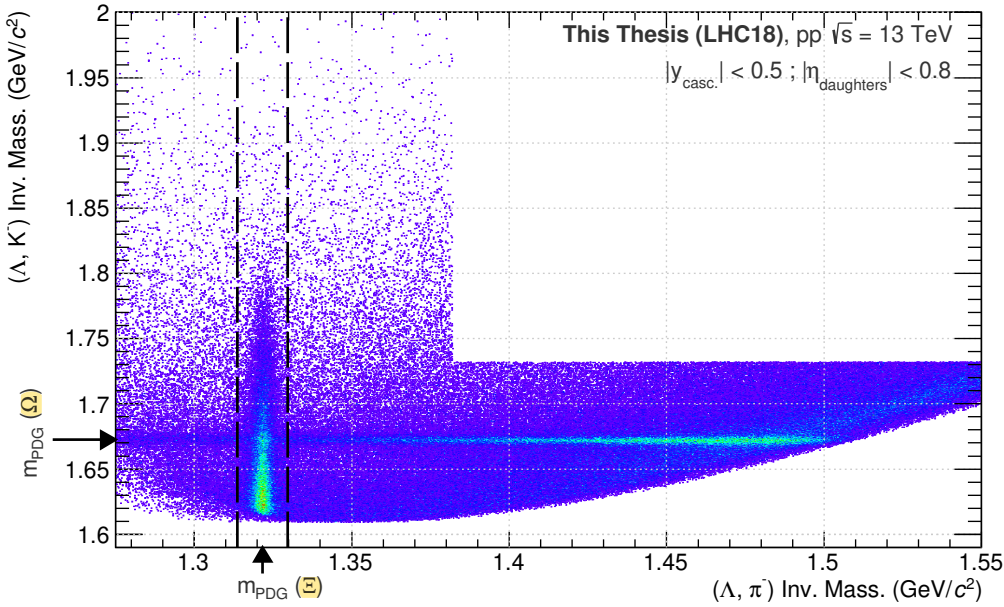


Fig. 4.4: Invariant mass distribution under the Ω^- and Ξ^- mass hypotheses, each cascade candidate can be seen under one hypothesis or the other (Eq. 4.6 and 4.7). The dashed lines show the mass rejection $m_{\text{PDG}}(\Xi) \pm 0.008 \text{ GeV}/c^2$, applied in the reconstruction of a $\bar{\Omega}^\pm$ candidate.

II-C The context of hyperon reconstruction in ALICE

In view of the characteristics of multi-strange baryons, it appears plainly that their reconstruction require excellent detection capabilities. In that regard, few experiments can compete with the performances of the ALICE detector at mid-rapidity.

As already outlined in Sec. II-B, the high granularity of its inner tracker allows to reconstruct the primary vertex, as well as the secondary vertices from V0 and cascade decays, with a precision better than $100 \mu\text{m}$ ¹⁶. Thanks to its large lever arm and almost continuous sampling of the particle trajectory, the TPC provides an excellent momentum measurement with a resolution of 0.7% ¹⁷ [107], as well as a robust particle identification. Hence, the TPC ensures an efficient reconstruction and identification of the hyperon's decay daughters, and thus of the hyperon itself. Coupled with its extremely low material budget ($13\% X_0$) and moderate magnetic field of 0.5 T , the strange hadron reconstruction can be performed over a wide momentum range and particularly, at low p_T , where the most important part of the production is.

Furthermore, the experiment benefits from the high-energy collisions delivered by the LHC. At such energies, matter and anti-matter are produced in almost equal proportions, offering the opportunity to study simultaneously hyperons and anti-hyperons. For all these reasons, ALICE stands as a perfectly suited experiment to analyse multi-strange baryons.

¹⁶Not to mention the resolution on the DCA of the daughter tracks to the primary vertex of about $30 \mu\text{m}$ [108].

¹⁷This obviously depends on the track momentum; here this is for $p_T = 1 \text{ GeV}/c$.

It should be emphasised that the cascade reconstruction varies with the track density, that goes from a few charged particles in pp collisions up to 2000 in the most central Pb-Pb collisions at $\sqrt{s_{\text{NN}}} = 5.02 \text{ TeV}$ [105]. In heavy-ion collisions, the enormous amount of tracks means a larger background, but also a larger number of contributor for the primary vertex determination and hence a better resolution on its position. This is in contrast with the pp environment, where the events are less dense but with a poorer quality on the interaction point location. Therefore, the topological selections shall be adapted for each environment, as these differences may lead to various biases on the DCA to the primary vertex, pointing angles, etc.

Also, a compromise has to be made between purity and reconstruction efficiency. In both cases, the key point revolves around the treatment of the background, which depends on the physics analysis. For example, if the background – or more precisely, its shape – is known in advance, the latter becomes tolerable as it can be subtracted later; thus, one may favour a high efficiency (*i.e.* relatively loose selections). In the reverse situation where the background is unknown, it seems preferable to apply tighter cuts in order to keep a signal with a low level of contamination, thus ensuring a high signal purity.

Chapter

5 | Mass measurements of multi-strange baryons in pp collisions at $\sqrt{s} = 13$ TeV

Chapter

6 | Analysis of the correlated production of strange hadrons

Chapter

7 | Discussion and conclusion

7 | Bibliography

- [1] P. A. Carruthers, *Quarkium: A Bizarre Fermi Liquid.* 1974.
- [2] B. J. Harrington and A. Yildiz, *High-Density Phase Transitions in Gauge Theories*, *Phys. Rev. Lett.* **33** (July, 1974) 324–327. [DOI Link](#).
- [3] J. C. Collins and M. J. Perry, *Superdense Matter: Neutrons or Asymptotically Free Quarks?*, *Phys. Rev. Lett.* **34** (May, 1975) 1353–1356. [DOI Link](#).
- [4] *New State of Matter created at CERN*,
<https://home.web.cern.ch/news/press-release/cern/new-state-matter-created-cern>, Jan. 2023.
- [5] T. Ludlam and S. Aronson, *HUNTING THE QUARK GLUON PLASMA.*,
<https://digital.library.unt.edu/ark:/67531/metadc1411284/>, Apr. 2005.
- [6] I. Arsene, *Quark Gluon Plasma an Color Glass Condensate at RHIC? The perspective from the BRAHMS experiment*, *Nuclear Physics A* **757** (Aug., 2005) 1–27, [[nucl-ex/0410020](#)].
[DOI Link](#).
- [7] B. B. B. et al, *The PHOBOS Perspective on Discoveries at RHIC*, *Nuclear Physics A* **757** (Aug., 2005) 28–101, [[nucl-ex/0410022](#)]. [DOI Link](#).
- [8] P. Collaboration and K. Adcox, *Formation of dense partonic matter in relativistic nucleus-nucleus collisions at RHIC: Experimental evaluation by the PHENIX collaboration*, *Nuclear Physics A* **757** (Aug., 2005) 184–283, [[nucl-ex/0410003](#)]. [DOI Link](#).
- [9] S. Collaboration and J. Adams, *Experimental and Theoretical Challenges in the Search for the Quark Gluon Plasma: The STAR Collaboration’s Critical Assessment of the Evidence from RHIC Collisions*, *Nuclear Physics A* **757** (Aug., 2005) 102–183, [[nucl-ex/0501009](#)].
[DOI Link](#).
- [10] *The third run of the Large Hadron Collider has successfully started*,
<https://home.cern/news/news/cern/third-run-large-hadron-collider-has-successfully-started>, Jan. 2023.
- [11] T. A. ALICE Collaboration, *Upgrade of the ALICE Experiment: Letter Of Intent*, *J. Phys. G: Nucl. Part. Phys.* **41** (July, 2014) 087001. [DOI Link](#).
- [12] A. Collaboration, *Characterizing the initial conditions of heavy-ion collisions at the LHC with mean transverse momentum and anisotropic flow correlations*, *Physics Letters B* **834** (Nov., 2022) 137393, [[arXiv:2111.06106](#)]. [DOI Link](#).
- [13] R. Schotter, *A multi-differential investigation of strangeness production in pp collisions with ALICE*, Feb. 2023. [arXiv:2302.00454](#).

- [14] Schotter, *QCD@LHC2022*, <https://indico.cern.ch/event/1150707/contributions/5112603/>.
- [15] B. Pullman, *The Atom in the History of Human Thought*. New York : Oxford University Press, 1998.
- [16] J. J. Thomson, *XL. Cathode Rays, The London, Edinburgh, and Dublin Philosophical Magazine and Journal of Science* **44** (Oct., 1897) 293–316. [DOI Link](#).
- [17] C. M. G. Lattes, H. Muirhead, G. P. S. Occhialini, and C. F. Powell, *Processes Involving Charged Mesons*, *Nature* **159** (May, 1947) 694–697. [DOI Link](#).
- [18] G. D. ROCHESTERDr. and C. C. BUTLERDr., *Evidence for the Existence of New Unstable Elementary Particles*, *Nature* **160** (Dec., 1947) 855–857. [DOI Link](#).
- [19] V. D. Hopper and S. Biswas, *Evidence Concerning the Existence of the New Unstable Elementary Neutral Particle*, *Phys. Rev.* **80** (Dec., 1950) 1099–1100. [DOI Link](#).
- [20] O. Chamberlain, E. Segrè, C. Wiegand, and T. Ypsilantis, *Observation of Antiprotons*, *Phys. Rev.* **100** (Nov., 1955) 947–950. [DOI Link](#).
- [21] F. Reines and C. L. COWANjun., *The Neutrino*, *Nature* **178** (Sept., 1956) 446–449. [DOI Link](#).
- [22] G. Danby, J.-M. Gaillard, K. Goulian, et al., *Observation of High-Energy Neutrino Reactions and the Existence of Two Kinds of Neutrinos*, *Phys. Rev. Lett.* **9** (July, 1962) 36–44. [DOI Link](#).
- [23] V. E. Barnes, P. L. Connolly, D. J. Crennell, et al., *Observation of a Hyperon with Strangeness Minus Three*, *Phys. Rev. Lett.* **12** (Feb., 1964) 204–206. [DOI Link](#).
- [24] R. Serway, C. Moses, and C. Moyer, *Modern Physics*. Cengage Learning, 2004.
- [25] V. Koch, *Aspects of Chiral Symmetry*, *Int. J. Mod. Phys. E* **06** (June, 1997) 203–249, [[nucl-th/9706075](#)]. [DOI Link](#).
- [26] M. E. Peskin, *An Introduction To Quantum Field Theory*. CRC Press, Boca Raton, Jan. 2018.
- [27] S. Braibant, G. Giacomelli, and M. Spurio, *Particles and Fundamental Interactions*. Undergraduate Lecture Notes in Physics. Springer Netherlands, Dordrecht, 2012.
- [28] E. Noether and M. A. Tavel, *Invariant Variation Problems, Transport Theory and Statistical Physics* **1** (Jan., 1971) 186–207, [[physics/0503066](#)]. [DOI Link](#).
- [29] *Definition of GAUGE*, <https://www.merriam-webster.com/dictionary/gauge>, Feb. 2023.
- [30] M. S. Sozzi, *Tests of discrete symmetries*, *J. Phys. G: Nucl. Part. Phys.* **47** (Nov., 2019) 013001. [DOI Link](#).
- [31] R. Lehnert, *CPT Symmetry and Its Violation*, *Symmetry* **8** (Nov., 2016) 114. [DOI Link](#).
- [32] R. G. Sachs, *The Physics of Time Reversal*. University of Chicago Press, Chicago, IL, Oct. 1987.
- [33] S. Glashow and B. Bova, *Interactions: A Journey Through the Mind of a Particle Physicist and the Matter of This World*, Sheldon Glashow with Ben Bova. 1988. Warner Books; New York, NY. 347 pages. ISBN: 0-446-51315-6. \$19.95, *Bulletin of Science, Technology & Society* **10** (Aug., 1990) 241–241. [DOI Link](#).
- [34] J. B. Kim, J. H. Kim, and H. K. Lee, *Electron-Neutrino Degeneracy and Primordial Nucleosynthesis*, Jan. 1997. [astro-ph/9701011](#).

- [35] M. Thomson, *Modern Particle Physics*, Cambridge University Press, Sept. 2013. [DOI Link](#).
- [36] *Quantum Diaries*,
<http://www.quantumdiaries.org/2011/06/19/helicity-chirality-mass-and-the-higgs/>.
- [37] C. MissMJ, *Standard model of elementary particles – wikimedia*,
https://commons.wikimedia.org/wiki/File:Standard_Model_of_Elementary_Particles.svg, Sept. 2019.
- [38] G. Jaeger, *The Elementary Particles of Quantum Fields*, Entropy **23** (Nov., 2021) 1416. [DOI Link](#).
- [39] J. Schmidhuber, *Evolution of National Nobel Prize Shares in the 20th Century*, Sept. 2010. [arXiv:1009.2634](#).
- [40] C. S. Wu, E. Ambler, R. W. Hayward, et al., *Experimental Test of Parity Conservation in Beta Decay*, Physical Review **105** (Feb., 1957) 1413–1415. [DOI Link](#).
- [41] M. Goldhaber, L. Grodzins, and A. W. Sunyar, *Helicity of Neutrinos*, Phys. Rev. **109** (Feb., 1958) 1015–1017. [DOI Link](#).
- [42] P. D. Group, *Review of Particle Physics*, PTEP **2022** (2022) 083C01. [DOI Link](#).
- [43] CERN, *New results indicate that particle discovered at CERN is a Higgs boson*,
<https://home.web.cern.ch/news/press-release/cern/new-results-indicate-particle-discovered-cern-higgs-boson>, Mar. 2023.
- [44] T. W. B. Kibble, *Englert-Brout-Higgs-Guralnik-Hagen-Kibble mechanism (history)*, Scholarpedia **4** (Jan., 2009) 8741. [DOI Link](#).
- [45] S. Sakata, *On a Composite Model for the New Particles*, Progress of Theoretical Physics **16** (Dec., 1956) 686–688. [DOI Link](#).
- [46] J. J. Sakurai, *Theory of strong interactions*, Annals of Physics **11** (Sept., 1960) 1–48. [DOI Link](#).
- [47] M. Gell-Mann, *THE EIGHTFOLD WAY: A THEORY OF STRONG INTERACTION SYMMETRY*, Tech. Rep. TID-12608; CTSL-20, California Inst. of Tech., Pasadena. Synchrotron Lab., Mar. 1961.
- [48] Y. Ne'eman, *Derivation of strong interactions from a gauge invariance*, Nuclear Physics **26** (Aug., 1961) 222–229. [DOI Link](#).
- [49] M. Gell-Mann, *Isotopic Spin and New Unstable Particles*, Phys. Rev. **92** (Nov., 1953) 833–834. [DOI Link](#).
- [50] P. Skands, *Introduction to QCD*, in *Searching for New Physics at Small and Large Scales*, pp. 341–420, Nov. 2013, [[arXiv:1207.2389](#)]. [DOI Link](#).
- [51] O. W. Greenberg, *Spin and Unitary-Spin Independence in a Paraquark Model of Baryons and Mesons*, Phys. Rev. Lett. **13** (Nov., 1964) 598–602. [DOI Link](#).
- [52] M. Y. Han and Y. Nambu, *Three-Triplet Model with Double \$|mathrm{SU}(3)\$ Symmetry*, Phys. Rev. **139** (Aug., 1965) B1006–B1010. [DOI Link](#).
- [53] J. Bjorken, *Current Algebra at Small Distances*, Tech. Rep. SLAC-PUB-0338, SLAC National Accelerator Lab., Menlo Park, CA (United States), June 2018.

- [54] R. P. Feynman, *The Behavior of Hadron Collisions at Extreme Energies*, in *Special Relativity and Quantum Theory: A Collection of Papers on the Poincaré Group* (M. E. Noz and Y. S. Kim, eds.), Fundamental Theories of Physics, pp. 289–304. Springer Netherlands, Dordrecht, 1988. [DOI Link](#).
- [55] H. Fritzsch, M. Gell-Mann, and H. Leutwyler, *Advantages of the color octet gluon picture*, *Physics Letters B* **47** (Nov., 1973) 365–368. [DOI Link](#).
- [56] J. E. Augustin, A. M. Boyarski, M. Breidenbach, et al., *Discovery of a Narrow Resonance in $\hat{e}^+ \hat{e}^- \rightarrow \text{Annihilation}$* , *Phys. Rev. Lett.* **33** (Dec., 1974) 1406–1408. [DOI Link](#).
- [57] J. J. Aubert, U. Becker, P. J. Biggs, et al., *Experimental Observation of a Heavy Particle J/ψ* , *Phys. Rev. Lett.* **33** (Dec., 1974) 1404–1406. [DOI Link](#).
- [58] H. Harari, *A new quark model for hadrons*, *Physics Letters B* **57** (July, 1975) 265–269. [DOI Link](#).
- [59] S. W. Herb, D. C. Hom, L. M. Lederman, et al., *Observation of a Dimuon Resonance at 9.5 GeV in 400-GeV Proton-Nucleus Collisions*, *Phys. Rev. Lett.* **39** (Aug., 1977) 252–255. [DOI Link](#).
- [60] CDF Collaboration, F. Abe, H. Akimoto, et al., *Observation of Top Quark Production in $\bar{p}p$ Collisions with the Collider Detector at Fermilab*, *Phys. Rev. Lett.* **74** (Apr., 1995) 2626–2631. [DOI Link](#).
- [61] D0 Collaboration, S. Abachi, B. Abbott, et al., *Observation of the Top Quark*, *Phys. Rev. Lett.* **74** (Apr., 1995) 2632–2637. [DOI Link](#).
- [62] B. R. Martin and G. Shaw, *Particle Physics*. John Wiley & Sons, Jan. 2017.
- [63] A. Maire, *Production des baryons multi-étranges au LHC dans les collisions proton-proton avec l'expérience ALICE*. PhD thesis, 2011.
- [64] D. J. Gross and F. Wilczek, *Ultraviolet Behavior of Non-Abelian Gauge Theories*, *Phys. Rev. Lett.* **30** (June, 1973) 1343–1346. [DOI Link](#).
- [65] H. David Politzer, *Asymptotic freedom: An approach to strong interactions*, *Physics Reports* **14** (Nov., 1974) 129–180. [DOI Link](#).
- [66] FT2, *English: Explanatory diagram showing how symmetry breaking works. At a high enough energy level, a ball settled in the center (lowest point), and the result has symmetry. At lower energy levels, the center becomes unstable, the ball rolls to a lower point - but in doing so, it settles on an (arbitrary) position and the result is that symmetry is broken - the resulting position is not symmetrical.*, 15 December 2012, 16:53:46.
- [67] Y. Nambu and G. Jona-Lasinio, *Dynamical Model of Elementary Particles Based on an Analogy with Superconductivity. I*, *Phys. Rev.* **122** (Apr., 1961) 345–358. [DOI Link](#).
- [68] S. Muroya, A. Nakamura, C. Nonaka, and T. Takaishi, *Lattice QCD at Finite Density – An introductory review*, *Progress of Theoretical Physics* **110** (Oct., 2003) 615–668, [[hep-lat/0306031](#)]. [DOI Link](#).
- [69] W. Weise, *Chiral symmetry in strongly interacting matter*, *Progress of Theoretical Physics Supplement* **186** (Oct., 2010) 390–403, [[arXiv:1009.6201](#)]. [DOI Link](#).
- [70] A. Bazavov, T. Bhattacharya, C. DeTar, et al., *The equation of state in (2+1)-flavor QCD*, *Phys. Rev. D* **90** (Nov., 2014) 094503, [[arXiv:1407.6387](#)]. [DOI Link](#).

- [71] E. Annala, T. Gorda, A. Kurkela, et al., *Evidence for quark-matter cores in massive neutron stars*, <https://arxiv.org/abs/1903.09121v2>, Mar. 2019.
- [72] M. Alford, K. Rajagopal, and F. Wilczek, *QCD at Finite Baryon Density: Nucleon Droplets and Color Superconductivity*, *Physics Letters B* **422** (Mar., 1998) 247–256, [[hep-ph/9711395](#)]. [DOI Link](#).
- [73] A. Maire, *Phase Diagram of QCD Matter: Quark-Gluon Plasma*. 2015.
- [74] O. Philipsen, *The QCD equation of state from the lattice*, *Progress in Particle and Nuclear Physics* **70** (May, 2013) 55–107, [[arXiv:1207.5999](#)]. [DOI Link](#).
- [75] M. A. Stephanov, *QCD phase diagram and the critical point*, *Int. J. Mod. Phys. A* **20** (July, 2005) 4387–4392, [[hep-ph/0402115](#)]. [DOI Link](#).
- [76] Rafelski, *Melting Hadrons, Boiling Quarks - From Hagedorn Temperature to Ultra-Relativistic Heavy-Ion Collisions at CERN*. Springer Cham, Apr. 2015.
- [77] J. Rafelski, *Melting Hadrons, Boiling Quarks*, *Eur. Phys. J. A* **51** (Sept., 2015) 114, [[arXiv:1508.03260](#)]. [DOI Link](#).
- [78] G. F. Chapline and A. K. Kerman, *On the Possibility of Making Quark Matter in Nuclear Collisions*, .
- [79] S. A. Chin, *Transition to hot quark matter in relativistic heavy-ion collision*, *Physics Letters B* **78** (Oct., 1978) 552–555. [DOI Link](#).
- [80] J. D. Bjorken, *Highly relativistic nucleus-nucleus collisions: The central rapidity region*, *Phys. Rev. D* **27** (Jan., 1983) 140–151. [DOI Link](#).
- [81] H. Satz, *The SPS heavy ion programme*, *Physics Reports* **403–404** (Dec., 2004) 33–50. [DOI Link](#).
- [82] J. E. Bernhard, *Bayesian parameter estimation for relativistic heavy-ion collisions*, <https://arxiv.org/abs/1804.06469v1>, Apr. 2018.
- [83] A. Maire, *Two Views on the Bjorken Scenario for Ultra-Relativistic Heavy-Ion Collisions*. 2011.
- [84] A. Collaboration, *The ALICE experiment – A journey through QCD*, Nov. 2022. [arXiv:2211.04384](#).
- [85] A. Collaboration, *Suppression of charged particle production at large transverse momentum in central Pb-Pb collisions at $\sqrt{s_{\text{NN}}} = 2.76 \text{ TeV}$* , *Physics Letters B* **696** (Jan., 2011) 30–39, [[arXiv:1012.1004](#)]. [DOI Link](#).
- [86] J. Rafelski, *Strangeness enhancement*, *Eur. Phys. J. Spec. Top.* **155** (Mar., 2008) 139–166. [DOI Link](#).
- [87] J. Rafelski and B. Müller, *Strangeness Production in the Quark-Gluon Plasma*, *Phys. Rev. Lett.* **48** (Apr., 1982) 1066–1069. [DOI Link](#).
- [88] J. Adam, D. Adamová, M. M. Aggarwal, et al., *Centrality dependence of $\psi(2S)$ suppression in p-Pb collisions at $\sqrt{s_{\text{NN}}} = 5.02 \text{ TeV}$* , *J. High Energ. Phys.* **2016** (June, 2016) 50. [DOI Link](#).
- [89] *Puzzle: Le Grand collisionneur de hadrons / Visitez le CERN*, https://visit.cern.fr/content/lhc_puzzle.
- [90] F. de Rose, *Paris 1951: The birth of CERN*, *Nature* **455** (Sept., 2008) 174–175. [DOI Link](#).

- [91] CERN council, *Convention for the Establishment of a European Organization for Nuclear Research / CERN Council*, <https://council.web.cern.ch/en/content/convention-establishment-european-organization-nuclear-research#7>, July 1953.
- [92] CERN, *Our People*, <https://home.cern/about/who-we-are/our-people>, Feb. 2023.
- [93] *The Future Circular Collider*, <https://home.cern/science/accelerators/future-circular-collider>, Feb. 2023.
- [94] M. Benedikt, A. Blondel, O. Brunner, et al., *Future Circular Collider - European Strategy Update Documents*. 2019.
- [95] *LHC Guide*. 2017.
- [96] Lopienska, Ewa, *The CERN accelerator complex, layout in 2022*, <https://cds.cern.ch/images/CERN-Graphics-2022-001-1>, Mar. 2022.
- [97] *The accelerator complex / CERN*, <https://home.cern/science/accelerators/accelerator-complex>.
- [98] *Greybook*, <https://greybook.cern.ch/>.
- [99] G. Aad, S. Bentvelsen, G. J. Bobbink, et al., *The ATLAS Experiment at the CERN Large Hadron Collider*. 2008.
- [100] C. Collaboration, S. Chatrchyan, G. Hmayakyan, et al., *The CMS experiment at the CERN LHC*, *J. Inst.* **3** (Aug., 2008) S08004. [DOI Link](#).
- [101] A. Collaboration, K. Aamodt, A. A. Quintana, et al., *The ALICE experiment at the CERN LHC*, *J. Inst.* **3** (Aug., 2008) S08002–S08002. [DOI Link](#).
- [102] L. Collaboration, A. A. A. Jr, L. M. A. Filho, et al., *The LHCb Detector at the LHC*, *J. Inst.* **3** (Aug., 2008) S08005. [DOI Link](#).
- [103] *LHC commissioning*, <https://lhc-commissioning.web.cern.ch/>.
- [104] ALICE Collaboration, *ALICE Collaboration*, <https://alice-collaboration.web.cern.ch/general-information>.
- [105] ALICE Collaboration, J. Adam, D. Adamová, et al., *Centrality Dependence of the Charged-Particle Multiplicity Density at Midrapidity in Pb-Pb Collisions at $\sqrt{s_{NN}} = 5.02 \text{ TeV}$* , *Phys. Rev. Lett.* **116** (June, 2016) 222302. [DOI Link](#).
- [106] a. F. Carminati, P. Foka, P. Giubellino, et al., *ALICE: Physics Performance Report, Volume I*, *J. Phys. G: Nucl. Part. Phys.* **30** (Oct., 2004) 1517. [DOI Link](#).
- [107] A. Collaboration, B. Alessandro, F. Antinori, et al., *ALICE: Physics Performance Report, Volume II*, *J. Phys. G: Nucl. Part. Phys.* **32** (Sept., 2006) 1295–2040. [DOI Link](#).
- [108] A. Collaboration, *Performance of the ALICE Experiment at the CERN LHC*, *Int. J. Mod. Phys. A* **29** (Sept., 2014) 1430044, [[arXiv:1402.4476](https://arxiv.org/abs/1402.4476)]. [DOI Link](#).
- [109] A. Collaboration, *Alignment of the ALICE Inner Tracking System with cosmic-ray tracks*, [arXiv:1001.0502 \[hep-ex, physics:physics\]](https://arxiv.org/abs/1001.0502) (Sept., 2017) [[arXiv:1001.0502](https://arxiv.org/abs/1001.0502)]. [DOI Link](#).
- [110] A. Maire and D. Dobrigkeit Chinellato, *ALICE Sub-Detectors Highlighted (LHC Runs 1+2 // Runs 3+4)*. 2017.

- [111] J. Alme, Y. Andres, H. Appelshäuser, et al., *The ALICE TPC, a large 3-dimensional tracking device with fast readout for ultra-high multiplicity events*, Nuclear Instruments and Methods in Physics Research Section A: Accelerators, Spectrometers, Detectors and Associated Equipment **622** (Oct., 2010) 316–367. [DOI Link](#).
- [112] A. Maire, *ALICE TPC Sectors and Pad Rows*. 2011.
- [113] A. Collaboration, *Performance of the ALICE VZERO system*, *J. Inst.* **8** (Oct., 2013) P10016–P10016, [[arXiv:1306.3130](#)]. [DOI Link](#).
- [114] A. Akindinov, F. Anselmo, M. Basile, et al., *The multigap resistive plate chamber as a time-of-flight detector*, Nuclear Instruments and Methods in Physics Research Section A: Accelerators, Spectrometers, Detectors and Associated Equipment **456** (Dec., 2000) 16–22. [DOI Link](#).
- [115] A. V. Akindinov, A. Alici, F. Anselmo, et al., *Study of gas mixtures and ageing of the multigap resistive plate chamber used for the Alice TOF*, Nuclear Instruments and Methods in Physics Research Section A: Accelerators, Spectrometers, Detectors and Associated Equipment **533** (Nov., 2004) 93–97. [DOI Link](#).
- [116] A. Collaboration, *Determination of the event collision time with the ALICE detector at the LHC*, *Eur. Phys. J. Plus* **132** (Feb., 2017) 99, [[arXiv:1610.03055](#)]. [DOI Link](#).
- [117] I. J. Bloodworth, G. Di Marzo-Serugendo, D. Evans, et al., *The ALICE Central Trigger Processor*. CERN, 2000.
- [118] ALICE Collaboration, *Trigger, Data Acquisition, High Level Trigger, Control System Technical Design Report*, <https://edms.cern.ch/ui/#!master/navigator/document?D:1811711722:1811711722:subDocs>.
- [119] A. Collaboration, *Charged-particle multiplicity measurement in proton-proton collisions at $\sqrt{s} = 0.9$ and 2.36 TeV with ALICE at LHC*, *Eur. Phys. J. C* **68** (July, 2010) 89–108, [[arXiv:1004.3034](#)]. [DOI Link](#).
- [120] ALICE Collaboration, *ALICE Trigger Coordination Twiki page*, <https://twiki.cern.ch/twiki/bin/viewauth/ALICE/TriggerCoordination>, Oct. 2020.
- [121] Caffarri, Davide, *Charm suppression in Pb-Pb collisions at the LHC measured using D0 K- π + reconstruction with the ALICE experiment*, <https://www.research.unipd.it/handle/11577/3422170?mode=complete>, Jan. 2012.
- [122] R. Mankel, *Pattern recognition and event reconstruction in particle physics experiments*, *Rep. Prog. Phys.* **67** (Mar., 2004) 553. [DOI Link](#).
- [123] A. Maire, *Track Reconstruction Principle in ALICE for LHC Run I and Run II*. 2011.
- [124] V. Karimäki, *Effective Vertex Fitting*. 1997.
- [125] Worldwide LHC Computing Grid, *Worldwide LHC Computing Grid's welcome page*, <https://wlcg-public.web.cern.ch/>.
- [126] Rene Brun and Fons Rademakers, *ROOT - An Object Oriented Data Analysis Framework*, <https://root.cern/>.
- [127] ALICE Collaboration, *AliRoot*, <https://github.com/alisw/AliRoot>.
- [128] ALICE Collaboration, *AliPhysics*, alisw, Feb. 2023.
- [129] V. Blobel and C. Kleinwort, *A New Method for the High-Precision Alignment of Track Detectors*, <https://arxiv.org/abs/hep-ex/0208021v1>, Aug. 2002.

- [130] C. Bierlich, S. Chakraborty, N. Desai, et al., *A comprehensive guide to the physics and usage of PYTHIA 8.3*, Mar. 2022. [arXiv:2203.11601](https://arxiv.org/abs/2203.11601).
- [131] M. Bähr, S. Gieseke, M. A. Gigg, et al., *Herwig++ physics and manual*, *Eur. Phys. J. C* **58** (Dec., 2008) 639–707. [DOI Link](#).
- [132] T. Pierog, Iu. Karpenko, J. M. Katzy, et al., *EPOS LHC: Test of collective hadronization with data measured at the CERN Large Hadron Collider*, *Phys. Rev. C* **92** (Sept., 2015) 034906. [DOI Link](#).
- [133] X.-N. Wang and M. Gyulassy, *HJING 1.0: A Monte Carlo Program for Parton and Particle Production in High Energy Hadronic and Nuclear Collisions*, *Computer Physics Communications* **83** (Dec., 1994) 307–331, [[nucl-th/9502021](https://arxiv.org/abs/nucl-th/9502021)]. [DOI Link](#).
- [134] R. Brun, F. Bruyant, M. Maire, et al., *GEANT 3: User's guide Geant 3.10, Geant 3.11; rev. version*, tech. rep., CERN, Geneva, 1987.
- [135] Geant4, *Geant4 home page*, <https://geant4-userdoc.web.cern.ch/UsersGuides/ForApplicationDeveloper/html/Introduction/introduction.html>.
- [136] G. Battistoni, T. Boehlen, F. Cerutti, et al., *Overview of the FLUKA code*, *Annals of Nuclear Energy* **82** (Aug., 2015) 10–18. [DOI Link](#).
- [137] J. Speltz, *Caractérisation d'un état dense de quarks et de gluons grâce aux fonctions d'excitation des hyperons multi-étranges mesurées avec l'expérience STAR au RHIC*. PhD thesis, Université Louis Pasteur - Strasbourg I, Oct. 2006.
- [138] A. Maire, *Four types of cascade decays for multi-strange baryons (charged Xi and Omega)*, 2011.
- [139] D. D. Chinellato, *Charm and multi-charm baryon measurements via strangeness tracking with the upgraded ALICE detector*, *EPJ Web Conf.* **259** (2022) 09004, [[arXiv:2110.00955](https://arxiv.org/abs/2110.00955)]. [DOI Link](#).
- [140] A. Maire, *Topological Selections for V0 (K0s, Lambda) and Cascade (Xi, Omega) Reconstruction in ALICE*. 2011.
- [141] A. Collaboration, *Production of light-flavor hadrons in pp collisions at $\sqrt{s} = 7$ and $\sqrt{s} = 13$ TeV*, arXiv:2005.11120 [hep-ex, physics:nucl-ex] (May, 2020) [[arXiv:2005.11120](https://arxiv.org/abs/2005.11120)].